

REPORT DOCUMENTATION PAGE

Form Approved
OMB No. 0704-0188

Public reporting burden for this collection of information is estimated to average 1 hour per response, including the time for reviewing instructions, searching existing data sources, gathering and maintaining the data needed, and completing and reviewing the collection of information. Send comments regarding this burden estimate or any other aspect of this collection of information, including suggestions for reducing this burden, to Washington Headquarters Services, Directorate for Information Operations and Reports, 1215 Jefferson Davis Highway, Suite 1204, Arlington, VA 22202-4302, and to the Office of Management and Budget, Paperwork Reduction Project (0704-0188), Washington, DC 20503.

1. AGENCY USE ONLY (Leave blank) 2. REPORT DATE 3. REPORT TYPE AND DATES COVERED
FINAL REPORT 15 Oct 93 - 31 Oct 94

4. TITLE AND SUBTITLE
Grating Light Valves for High Resolution Displays 5. FUNDING NUMBERS
61101E
A564/16

6. AUTHOR(S)
Professor Bloom

7. PERFORMING ORGANIZATION NAME(S) AND ADDRESS(ES)
Stanford University
Stanford, CA 94305-4125 AFOSR-TR-95
0793

9. SPONSORING/MONITORING AGENCY NAME(S) AND ADDRESS(ES)
AFOSR/NE
110 Duncan Avenue Suite B115
Bolling AFB DC 20332-0001

10. SPONSORING/MONITORING AGENCY REPORT NUMBER
F49620-93-1-0609

11. SUPPLEMENTARY NOTES

12a. DISTRIBUTION/AVAILABILITY STATEMENT
APPROVED FOR PUBLIC RELEASE: DISTRIBUTION UNLIMITED

12b. DISTRIBUTION STATEMENT
DTIC
SELECTED
JAN 03 1996
F

13. ABSTRACT (Maximum 200 words)

The Grating Light Valve (GLV) is a micromechanical phase grating that can be used for color display applications. Operation is based on electrically controlling the mechanical positions of grating elements to modulate diffraction efficiency. By choosing dimensions of the grating structures carefully, it is possible to produce a digital optical device.

DTIC QUALITY INSPECTED 2

19960102 006

15. NUMBER OF PAGES

16. PRICE CODE

17. SECURITY CLASSIFICATION OF REPORT
UNCLASSIFIED 18. SECURITY CLASSIFICATION OF THIS PAGE
UNCLASSIFIED 19. SECURITY CLASSIFICATION OF ABSTRACT
UNCLASSIFIED 20. LIMITATION OF ABSTRACT

FINAL REPORT
F49620-93-1-0609

GRATING LIGHT VALVES FOR HIGH RESOLUTION DISPLAYS

RAJ B. APTE
Report No. 5192

A DISSERTATION
SUBMITTED TO THE DEPARTMENT OF
ELECTRICAL ENGINEERING
AND THE COMMITTEE ON GRADUATE STUDIES
OF STANFORD UNIVERSITY
IN PARTIAL FULFILLMENT OF THE REQUIREMENTS FOR THE DEGREE
OF

DOCTOR OF PHILOSOPHY

Accession For		
NTIS	CRA&I	<input checked="" type="checkbox"/>
DTIC	TAB	<input type="checkbox"/>
Unannounced		<input type="checkbox"/>
Justification		
By		
Distribution /		
Availability Codes		
Dist	Avail and/or Special	
A-1		

June 1994

© COPYRIGHT BY RAJ B. APTE

All Rights Reserved. No part of this publication may be reproduced, stored in a retrieval system or transmitted in any form or by any means: electronic, electrostatic, optic, magnetic, mechanical, photocopying, recording or otherwise, without permission in writing from the author.

I certify that I have read this dissertation and that in my opinion it is fully adequate,
in scope and quality, as a dissertation for the degree of Doctor of Philosophy.

David M. Bloom, Principal Advisor

I certify that I have read this dissertation and that in my opinion it is fully adequate,
in scope and quality, as a dissertation for the degree of Doctor of Philosophy.

James S. Harris

I certify that I have read this dissertation and that in my opinion it is fully adequate,
in scope and quality, as a dissertation for the degree of Doctor of Philosophy .

Thomas Kenny

Approved for the University Committee on Graduate Studies.

Abstract

The Grating Light Valve (GLV) is a micromechanical phase grating that can be used for color display applications. Operation is based on electrically controlling the mechanical positions of grating elements to modulate diffraction efficiency. By choosing dimensions of the grating structures carefully, it is possible to produce a digital optical device.

Since gratings are inherently dispersive, the GLV can be used for color displays. Full NTSC-quality colors are available. In addition, the devices are bistable and may be able to operate with a passive matrix of contacts and still achieve the performance of an active matrix light valve. Eight bits of gray scale are possible using time division multiplexing and the fast (20 ns) switching speed of the GLV. The contrast ratio of the device is sensitive to processing errors, and a ratio of 20:1 was measured. With better processing, a color contrast of 200:1 should be achieved. The operating voltage is 20 V, but there is good evidence that 5 V operation is feasible.

One problem in the development of large one-dimensional and two-dimensional arrays of devices was sticking during the final wet processing step. This is a common problem in micromachines. Our solution is to use rough (150 Å-RMS) polysilicon films to reduce the area of contact between the moving parts and the substrate. In the case of two-dimensional arrays, this film could be doped and function as the second dimension of interconnects. Although this structure suffers from some of the difficulties of a non-planar process, it was used to demonstrate two-dimensional arrays of devices.

Acknowledgments

This work was sponsored by Andy Yang and Ken Gabriel of the Advanced Research Projects Administration under Contracts DAAL03-92-G-0232 and F49620-93-I-0609.

In addition to the sponsors I would like to thank my advisor, Dave Bloom, whose tireless energy and enthusiasm never failed to rouse me from my processing-lab stupor, and my research associate, Bill Banyai, who deconstructed my experiments. I hope that someday I will be worthy of their efforts.

Contents

Abstract.....	iv
Acknowledgments.....	v
Contents	vi
List of Figures	ix
List of Tables	xii
List of Photographs	xiii
Introduction	1
1.1 Basic Device Fabrication and Operation	1
1.2 Comparison with LCDs and Other Micromechanical Valves.....	2
1.2.1 Limitations of LCDs	2
1.2.2 Other Micromechanical Displays	3
1.3 This Work	6
1.4 Outline	6
Optics of the GLV	7
2.1 Diffraction Grating Analysis	7
2.1.1 Basic Operation of the GLV.....	9
2.1.2 Scalar Diffraction Theory.....	9
2.2 Basic Optical Systems.....	12
2.3 Monochrome Contrast Ratio	15

2.3.1	Brightness and Contrast Ratio	15
2.3.2	Effect of Etch Anisotropy on Contrast.....	18
2.4	Color Operation.....	18
2.4.1	CIE Color Coordinates	20
2.4.2	Color Design.....	22
2.5	Color Contrast Ratio	25
2.6	Pixel Size Limits.....	27
Mechanics of the GLV		30
3.1	Basics of hysteresis	30
3.2	Materials Parameters	32
3.3	String Model	33
3.4	Beam Model.....	36
3.4.1	Switching Voltage.....	38
3.4.2	Peak Stress.....	39
3.4.3	Hysteresis	39
3.5	Row-addressing Method.....	40
3.6	Speed.....	42
3.7	Temperature Limits.....	42
Fabrication of the GLV		45
4.1	Basic Process	45
4.2	Isolation.....	47
4.3	Interconnect Conductivity and Reflectivity	50
4.4	Sticking	51
4.4.1	Water.....	52
4.4.2	Beam Peeling Theory	53
4.4.3	Stress	53
4.4.4	Surface Treatments.....	54
4.4.5	Striations	55
4.4.6	Van der Waals Bonding	56
4.4.7	Surface Roughness and Contrast.....	60
4.4.8	Progress in Reducing Sticking.....	61
4.5	Two-Dimensional Arrays.....	63
4.5.1	Isolation	63
4.5.2	Thermal budget.....	63

4.5.3 Basic Recipe	64
4.5.4 Nonplanar Processing	64
4.6 Reliability	66
4.7 Device Failure	67
4.8 Future Process Design	67
Conclusion	71
5.1 Device Summary	71
5.2 Future Work	72
Bibliography	74
Appendix 1	82
A1.1 Standard Process Steps	82
A1.2 Current GLV process	83
Appendix 2	85

List of Figures

Figure 1.1	
A single GLV pixel.....	2
Figure 2.1	
Diffraction efficiency for several orders of an aluminum reflection phase grating	8
Figure 2.2	
Two states of the GLV.....	9
Figure 2.3	
Diffraction efficiency (diffractivity) of the first order as a function of wavelength for a “down” pixel, $S_{down}(\lambda)$	11
Figure 2.4	
Diffraction efficiency (diffractivity) of the first order as a function of wavelength for an “up” pixel, $S_{up}(\lambda)$	11
Figure 2.5a	
Simple monochrome optical system (I).....	13
Figure 2.5b	
Simple optical system (II) for electrical characterization of devices	14
Figure 2.6	
BW responsivity of the human eye.....	16
Figure 2.7	
BW contrast ratio vs. wavelength for narrowband sources	16
Figure 2.8	
BW contrast ratio vs. film thickness error.....	17
Figure 2.9	
Effect of bad sidewalls on contrast ratio.....	19

Figure 2.10	
Contrast ratio vs. sidewall angle.....	19
Figure 2.11	
Color responsivity of the human eye.....	21
Figure 2.12	
Basic optics of Schlieren system (III).....	24
Figure 2.13	
Measured color coordinates and theoretical values of the GLV with NTSC	
phosphor standards and the visible gamut.....	26
Figure 2.14	
Color coordinates of green pixel as a function of diffraction angle.....	26
Figure 3.1	
Basic model for the GLV beam mechanics.....	30
Figure 3.2	
Origin of hysteresis	31
Figure 3.4	
Results of beam model.....	38
Figure 3.5	
Simulated hysteresis curve	40
Figure 3.6	
Measured hysteresis curve of a single pixel.....	41
Figure 3.7	
Pixel switching in 20.5 ns.....	43
Figure 4.1	
Single pixel of the one mask GLV process.....	46
Figure 4.2	
Schematic of single mask process.....	46
Figure 4.3	
Device to device isolation.....	47
Figure 4.4	
Field concentration caused by poor sidewalls.....	50
Figure 4.5	
Control of residual stress in LPCVD nitride	54
Figure 4.6	
Beam peel length as a function of residual stress and striations	58

Figure 4.7	
Surface roughness and beam sticking.....	59
Figure 4.8	
Contrast ratio versus film thickness.....	59
Figure 4.9	
Schematic of two dimensional array	65

List of Tables

Table 2.1	
Basic values of color parameters	22
Table 2.2	
Contrast ratio for unoptimized system	27
Table 2.3	
Contrast ratio for optimized system	27
Table 3.1	
Basic physical and geometric factors of the GLV	33
Table 3.2	
Three different types of nitride in use	33
Table 3.3	
Experimental second instability voltages	38
Table 3.4	
Materials parameters for thermal expansion	44
Table 4.1	
Progress in decreasing sticking	62

List of Photographs

Photograph 2.1	
SEM of color pixels	25
Photograph 2.2	
Sideview of stuck beams	29
Photograph 4.1	
Grating destroyed by shorting and fusing.....	48
Photograph 4.2	
Closeup of fused beam	49
Photograph 4.3	
Harp test structure.....	52
Photograph 4.4	
Atomic force microscope image of harp structure	56
Photograph 4.5	
Striations in one dimensional arrays	57
Photograph 4.6a	
Rough polysilicon surface.....	60
Photograph 4.6b	
Nitride deformed by rough polysilicon	61
Photograph 4.7	
Single pixel in a two-dimensional array	62
Photograph 4.8	
4x4 pixel array.....	66
Photograph 4.9	
Four corners of a two dimensional array	68
Photograph 4.10	
Four corners point of two-dimensional array, alternate view	69

Chapter 1

Introduction

1.1 Basic Device Fabrication and Operation

The Grating Light Valve (hereafter GLV) is a micromechanical light valve intended for display applications. A single pixel is shown in Figure 1.1. The body of the device is a collection of ten beams stretched across a frame. This frame is attached by a spacer to the substrate, leaving the beams suspended in air. By moving the beams electrostatically it is possible to modulate the diffraction efficiency of light incident on the structure. This device, whose fabrication uses only standard Silicon processes, is the subject of this thesis.

As a light valve for display, the GLV has a number of interesting properties. GLV fabrication is fairly simple, requiring only one mask step for basic devices and only three or four for complete array fabrication. This should translate into low production cost. The GLV is capable of either black-and-white (BW) or color operation with white light illumination. The pixels of the GLV are extremely fast, switching in under 25 ns. Furthermore, the pixels are bistable with applied voltage: it may be possible to operate the GLV and achieve active matrix performance with only a passive matrix. The combination of speed and bistability may be used for spatial light modulator applications as well as for simplifying the design of drivers (fast pixels can be addressed by a passive matrix, while slow pixels require the increased complexity of an active matrix structure).

1.2 Comparison with LCDs and Other Micromechanical Valves

From the mid-seventies micromechanical display technologies have been under investigation. Commercialization has focused on pivoting or moving mirrors to steer light into or out of collection optics [Sampsel 1992]. An alternative technology uses elastomers as the micromechanical layer in a diffractive configuration [Gerhard-Multhaupt 1990]; this technology is the most similar to the GLV. A comparison of GLV technology with the dominant new display technology, liquid crystal displays (LCDs), and other micromechanical display technologies will serve to explain the motivation for this work.

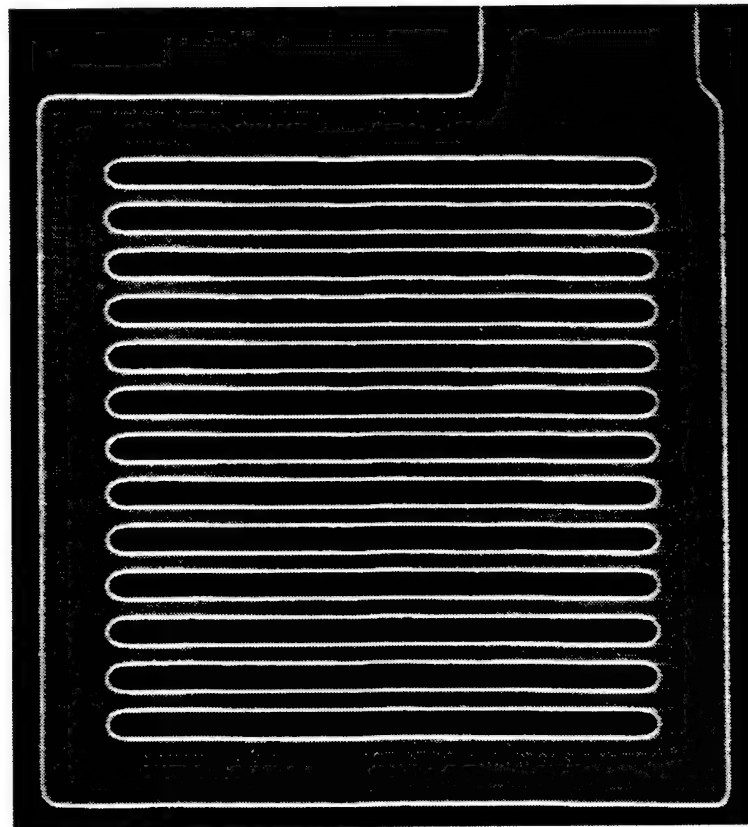


Figure 1.1: A single GLV pixel

1.2.1 Limitations of LCDs

The attraction of micromechanical displays is that they do not suffer from the limited speed and efficiency of LCDs. Nematic LCDs switch in milliseconds, and while new, faster liquid crystal technologies are under investigation, commercial LCD pixels operate

at little more than the video frame refresh rate. This complicates the design of device drivers, since simple row-by-row addressing requires devices to respond in a small fraction of the frame rate. LCD panels typically include an active matrix of perhaps a million transistors which can latch quickly. A second problem with LCDs is their limited optical efficiency. Typically around 5% of the light that enters a color LC valve makes it to the screen. This problem is especially acute for projection displays, which require maximum delivery of screen lumens. Micromechanical displays are potentially capable of a 500% improvement in optical throughput over LCDs (i.e., 25% of the incident light reaching the screen). In applications where lamp power is limited, this may be an important factor against LCDs.

If lamp technology is not a limiting factor, then the brightness of a light valve display is governed by the generation of heat in the valve. All the light that is not transmitted through a LC light valve is dissipated in the valve itself as heat, so the low optical throughput translates into device heating. The problem is compounded by the fact that LCDs are very temperature sensitive, with only a 40° C operating range. The GLV is constructed of high temperature ceramic materials and is very insensitive to temperature variations. In addition, micromechanical light valves modulate light by switching it from the collection optics into a beam dump: the energy not transmitted from dark pixels does not heat the device. Only about 8% of the incident light is absorbed by the aluminum reflector on the surface of the chip. These facts combine to make it likely that much larger lamps can be used with micromechanical displays compared to LCDs. Larger lamps and higher efficiencies mean more screen lumens.

The promise solving the problems of LCDs—speed, optical efficiency, and temperature sensitivity/device heating—makes micromechanical displays interesting to a number of companies [Sampsell 1992], including those with LCD manufacturing capability [Yoshida 1993].

1.2.2 Other Micromechanical Displays

Pioneers of micromachining first proposed micromechanical displays in the mid-seventies [Petersen 1982]. Commercial development commenced at Texas Instruments soon after and continues to the present [Hornbeck 1991a; Hornbeck 1991b; Sampsell 1990]. Their work is based on electrostatic pivoting or moving mirrors. Since mirrors have to be rigid while beams in the GLV are flexible, mirrors are nearly an order of magnitude thicker than beams. This translates into a larger moment of inertia and slower

accelerations for a given driving torque. Also, mirrors must be deflected by several microns while beams require less than one seventh of a micron deflection. For these reasons GLV is more than two orders of magnitude faster than Texas Instruments' Deformable Mirror Device (DMD).

The difference in speed is sufficient to allow row-addressing of the GLV while limiting the DMD to frame addressing. In row-addressing, each row pixels is selected, one at a time. Simultaneously pixel data is put on the column drivers. Following the write cycle, the current row is de-selected and the next row is selected. If each pixel contains memory, either by the integration of a transistor or some inherent bistability, then this method does not suffer from the limited contrast of passive-matrix addressing [Alt 1973]. Clearly the pixels must respond faster than the frame-rate times the number of rows. For digital pixels (which both DMD and GLV use), the response of the pixel must be faster still by the number of distinct gray levels. For a 1000 row display with 8 bits of grayscale (per color) addressed at 60 Hz, the pixels must be capable of responding at 15 MHz. The GLV is capable of this speed.

For the slower DMD pixels, more cumbersome frame-addressing is needed. A matrix of fast master-slave flip-flops is located beneath the pixels, one flip-flop per pixel. The master is connected to the addressing lines of that pixel, while the slave is connected to the mirror immediately above it. The master flip-flops are row addressed. After the complete frame of master flip-flops has been programmed for the next frame, the data from each master is latched to its slave and the mirror that stands above it. The master to slave latching is done for the entire frame simultaneously. Finally, row-addressing of master flip-flops continues for the next frame.

Frame-addressing achieves the same performance as row-addressing, but requires eight transistors per pixel (four for each flip-flop). Eight million transistors are needed in a megapixel display. Only two-thousand drivers are needed for the GLV, each of which must switch among three logic states. Since tri-state logic requires fewer than 10 transistors per driver, fewer than twenty thousand transistors are needed for a megapixel GLV. The reduced complexity of the GLV should make it less expensive to manufacture than the DMD.

A second advantage of the GLV over the DMD is that the GLV is capable of producing color from a white illumination source without any additional components. Although the

DMD can be used for color, the addition of a large, rotating color wheel or other color selector is needed to illuminate the DMD with red, green, and blue light sequentially. The frame rate is tripled, and the DMD images the red, green, and blue component in succession. The eye integrates the three primary images into one color image. The addition of a color selector is not needed for the GLV: it is converted from BW to color operation simply by narrowing a slit in the projection optics. The intrinsic color generation of the GLV will be very useful for manufacturing compact color displays for pager and head-mounted applications.

Other micromechanical display technologies are based on electron beam, active-matrix Silicon, or CRT/photoconductor addressing of viscoelastic and oil films [Gerhard-Multhaupt 1991]. Electron beams and CRT/photoconductor addressed displays are unlikely to have a major impact because of their high cost and therefore small penetration into the low and middle parts of the market. However, there is promise that research on active-matrix viscoelastic systems may lead to mainstream products in the future because of their simplicity of fabrication and compatibility with CMOS process integration.

Viscoelastic spatial light modulators (VSLMs) [Gerhard-Multhaupt 1990] use a thin viscoelastic layer sandwiched between a flexible layer of metal and a rigid substrate with transistors and metal lines on the other. If a voltage is applied to the lines, which are shaped like gratings, the top metal is attracted and the viscoelastic layer and top metal deform together. This forms a sinusoidal grating on the top metal. Essentially, the GLV and VSLM are based on the same principles of operation, with different implementations of the spacer layer: air vs. plastic. Since the surface deformations are similar in shape, the optical systems are very similar. One advantage of the VSLM is that it does not require any high temperature processing, so integration with driver circuits and active matrices is greatly simplified. Nevertheless, a passive matrix GLV that only requires a few thousand driver transistors may be easier to manufacture than the VSLM with an active matrix of millions of transistors.

1.3 This Work

Original contributions of this thesis are the discussions of color, device modeling and the fabrication of two-dimensional arrays of devices. Specifically:

- Generating color using the dispersive properties of gratings and Schlieren optics.
- Modeling the contrast ratio for broadband illumination.
- Modeling the mechanical properties of beams.
- Using striations to reduce sticking of the beams to the substrate.
- Using surface roughness to reduce sticking of the beams to the substrate.
- Fabricating two-dimensional arrays of devices.
- Proposing a two-dimensional addressing scheme.

Other students, Olav Solgaard and Francisco Sandejas, did the initial process design and first mask layout. In addition, Francisco developed other processes to decrease sticking and to obtain critical sidewall (and dimensional) control for higher contrast.

1.4 Outline

This chapter presented a sketch of micromechanical entries into display development and a comparison with LCDs. Chapter 2 explains the optical properties of the device, including the principle of operation, color generation, contrast ratio, and scalability. Two models for the electromechanical operation of the device are presented in Chapter 3. These models are used in Chapter 4 to analyze the problem of stiction encountered during fabrication. The process design for two-dimensional arrays is reviewed. Chapter 5 summarizes the research on this device and discusses future research topics. The two appendices give specific process recipe steps for the devices and the details of the numerical beam calculations.

Chapter 2

Optics of the GLV

2.1 Diffraction Grating Analysis

A diffraction grating is a periodic structure that affects either the amplitude or phase of incident light. Typically the period is several times the wavelength of light. A detailed analysis of diffraction gratings [Born 1980] shows that incident light is diffracted by the grating into several directions which conform to the Bragg condition. Amplitude gratings are formed by alternating stripes of absorbing and transmitting material. Phase gratings modulate the phase rather than the amplitude of light.

The GLV is a microelectromechanical phase diffraction grating. The amplitudes of the diffracted modes of a $2.00\text{ }\mu\text{m}$ period phase grating with rectangular grooves constructed from aluminum as a function of groove depth are shown in Figure 2.1. The specular mode has a peak reflectivity of 92% when no grooves are present (92% is the reflectivity of aluminum). This value decreases as the light is diffracted rather than reflected. However, when the grooves are $\lambda/2$ deep, the reflectivity is again maximum. Shadowing effects (caused by reflections from the sidewalls of the grating elements) limit this maximum reflectivity to 82%.

The light that is not reflected into the specular mode is diffracted. For small grating depths there is little diffraction. As the round-trip depth approaches $\lambda/4$ in phase, the diffraction peaks, with 41% of the light in each of the first order diffraction modes. At a grating depth of $\lambda/2$ the diffracted light is again nulled. In this case the grating functions like a perfectly flat mirror, for nearly an octave of wavelengths of light. Since each of the

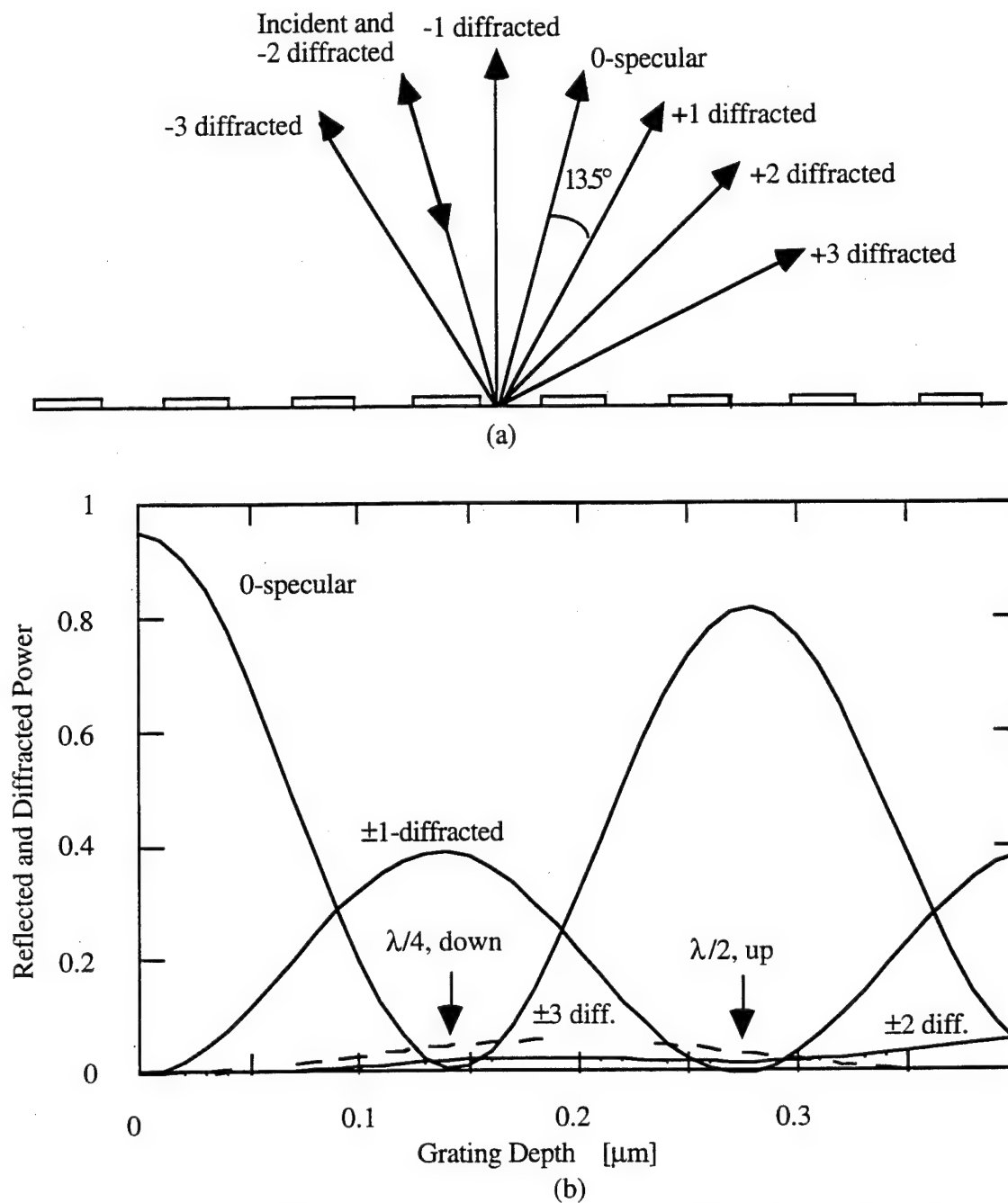


Figure 2.1: Diffraction efficiency for several orders of an aluminum reflection phase grating with a $2.00 \mu\text{m}$ period, illuminated at 13.5° incidence at 550 nm . (a) shows schematically the diffracted modes. (b) shows the diffracted intensities as a function of grating depth. Note the finite reflectivity of aluminum limits the specular reflection with no groves to 92%. [Gaither 1988; Veldkamp 1989]

diffracted modes has a different diffraction angle, the component of the wavevector normal to the grating varies with order number. This variation is what causes the higher order modes to null further out than the ± 1 order. Thus, not all the diffracted modes can be nulled at one grating depth. Fortunately, these higher orders are fairly small in magnitude, so that the total power lost if they are spatially filtered is negligible.

2.1.1 Basic Operation of the GLV

The switching of the diffraction efficiency can be used to make devices in a number of ways. The two basic methods depend on whether the reflected or diffracted light is collected by the optical system. These are demonstrated in Figure 2.2. In the undeflected, or “up” case, which corresponds to $\lambda/2$ the GLV is purely reflecting. In the deflected, or “down” case, the phase delay is $\lambda/4$ and the diffraction into the ± 1 diffraction orders is maximized. The key to device operation is that the spacer and beam thicknesses are chosen to be $\lambda/4$ deep.

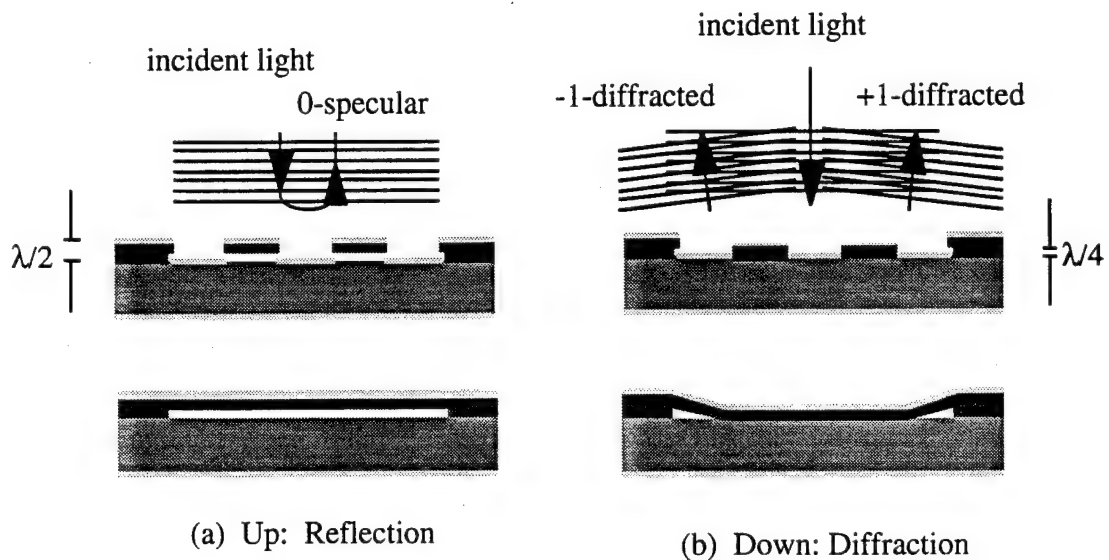


Figure 2.2: Two states of the GLV. In (a), the beams are up and the device reflects the incident light. In (b), when the beams are down, the GLV diffracts all the light. The top two illustrations show the cross section through the beams. The bottom two show a cross section that is parallel to the beams.

2.1.2 Scalar Diffraction Theory

Scalar diffraction theory for normal incidence is largely in agreement with Figure 2.1. The scalar theory gives for the ± 1 diffraction orders [Solgaard 1992]

$$I = \frac{I_0}{2} \text{sinc}^2\left(\frac{\pi}{2}\right) \left[1 - \cos\left\{ \frac{2\pi d}{\lambda} \left(1 + \frac{1}{\sqrt{1 - (\lambda/p)^2}} \right) \right\} \right]$$

where I_0 is the incident light intensity, d is the grating depth, λ is the wavelength of the incident light, and p is the periodicity of the grating. For small diffraction angles ($2 \mu\text{m}$ periodicity gives a diffraction angle of 15° at 550 nm) and a grating designed with $d = \lambda_0/4$ for a design wavelength of λ_0 , the intensity of the ± 1 diffraction orders for a “down” pixel is

$$S_{\text{down}}(\lambda) = 0.41 \frac{S_0(\lambda)}{2} \left[1 - \cos \frac{\pi \lambda_0}{\lambda} \right]$$

For an “up” pixel the corresponding expression is

$$S_{\text{up}}(\lambda) = 0.41 \frac{S_0(\lambda)}{2} \left[1 - \cos \frac{2\pi \lambda_0}{\lambda} \right]$$

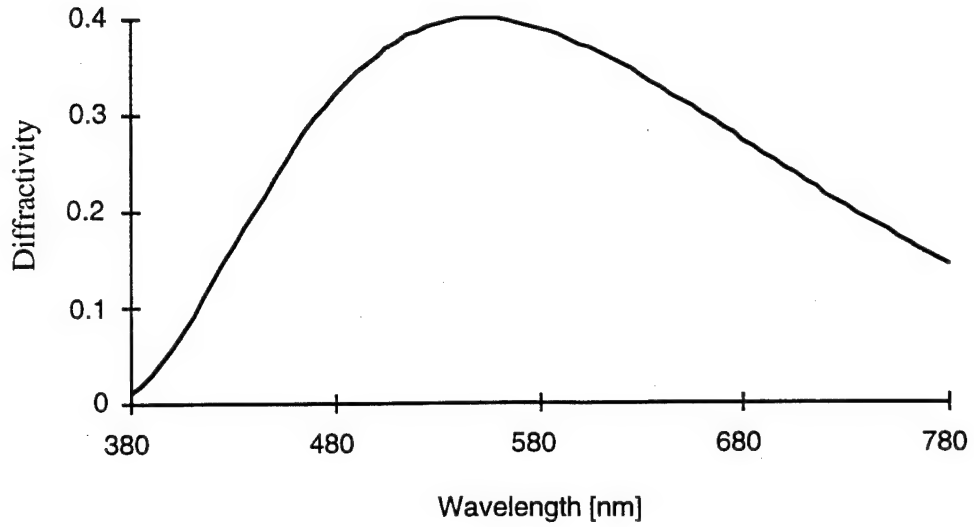


Figure 2.3: Diffraction efficiency (diffractivity) of the first order as a function of wavelength for a “down” pixel, $S_{down}(\lambda)$. This grating is designed for 550 nm.

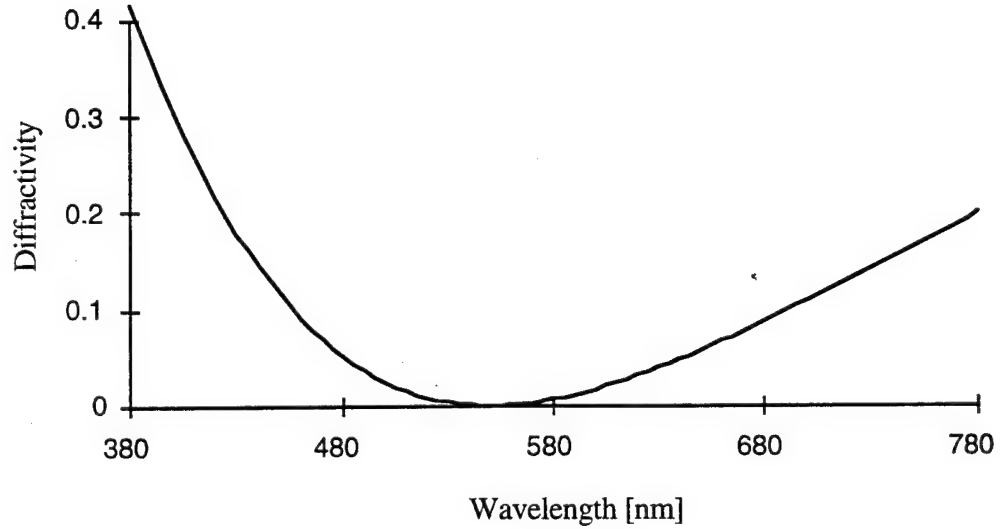


Figure 2.4: Diffraction efficiency (diffractivity) of the first order as a function of wavelength for an “up” pixel, $S_{up}(\lambda)$. This grating is designed for 550 nm.

The plots of $S_{down}(\lambda)$ and $S_{up}(\lambda)$, Figures 2.3 and 2.4, respectively, illustrate the basis of the bandwidth and the contrast ratio of the device. It is apparent that the GLV modulates

light over a 200 nm bandwidth. The contrast at any particular wavelength is simply the ratio of $S_{down}(\lambda)$ to $S_{up}(\lambda)$. Because $S_{up}(\lambda)$ is a null at only a single wavelength (550 nm in this case), the contrast ratio peaks at that point and declines to either side. In Section 2.3 these parameters will be used along with a development of human visual perception to calculate contrast ratios for these devices when used in optical systems described in Section 2.2.

2.2 Basic Optical Systems

Optical systems can be constructed to view either the reflected or diffracted light. The latter has two clear advantages. Since the non-diffraction grating portions of the device, including bond pads and other large areas, remain equally reflecting in both the “up” and “down” positions, there will be a problem generating adequate contrast without the use of masking films or spatial filters to remove the unmodulated light. The second advantage to viewing the diffracted light is that the spatial dispersion of the grating, discussed in Section 2.4 and Figure 2.12, can be used to make color pixels.

The basis of BW operation was shown in Figure 2.2. When the beams are “up,” the device is reflective, and the normally incident light is reflected back to the source. If the beams are brought into the “down” position, then the pixel diffracts 82% of the incident light into the ± 1 diffraction modes. Additional light is diffracted into higher order modes (about 10% of the incident), but the optics used had too small an aperture to collect this light.

The optical systems were used in device testing. The prototypical BW optical system (hereafter, system I), is shown in Figure 2.5. The illumination source was either a 250 W metal halide arc lamp with an integrated reflector or a 40 W tungsten-halogen lamp with dielectric reflector. The light was condensed with f/2.4 optics and imaged without magnification at an intermediate point. At the intermediate point the image was spatially filtered to insure adequate collimation. Since collimation within the plane of Figure 2.5 is essential for good contrast, the arc or filament of the lamp is shown perpendicular to this plane. The source image was then collimated and directed by a turning mirror onto the face of the device. The specular reflection was returned to the lamp, while the diffracted orders were collected by a projection lens placed just over a focal length away. The distance between the device and the projection lens was adjusted to focus the image on a distant screen. In this system the projection lens is used both for projection to the

screen as well as spatial filtering of the diffracted light. A telecentric stop was placed at a distance of one focal length from the projection lens. At this plane, all rays from the device plane with the same angle all pass through the same point, i.e., all the +1 diffraction order rays focus at one point while all the -1 rays focus at another. By placing a stop with slits in it at those two points, all non-diffracted light is blocked from the screen.

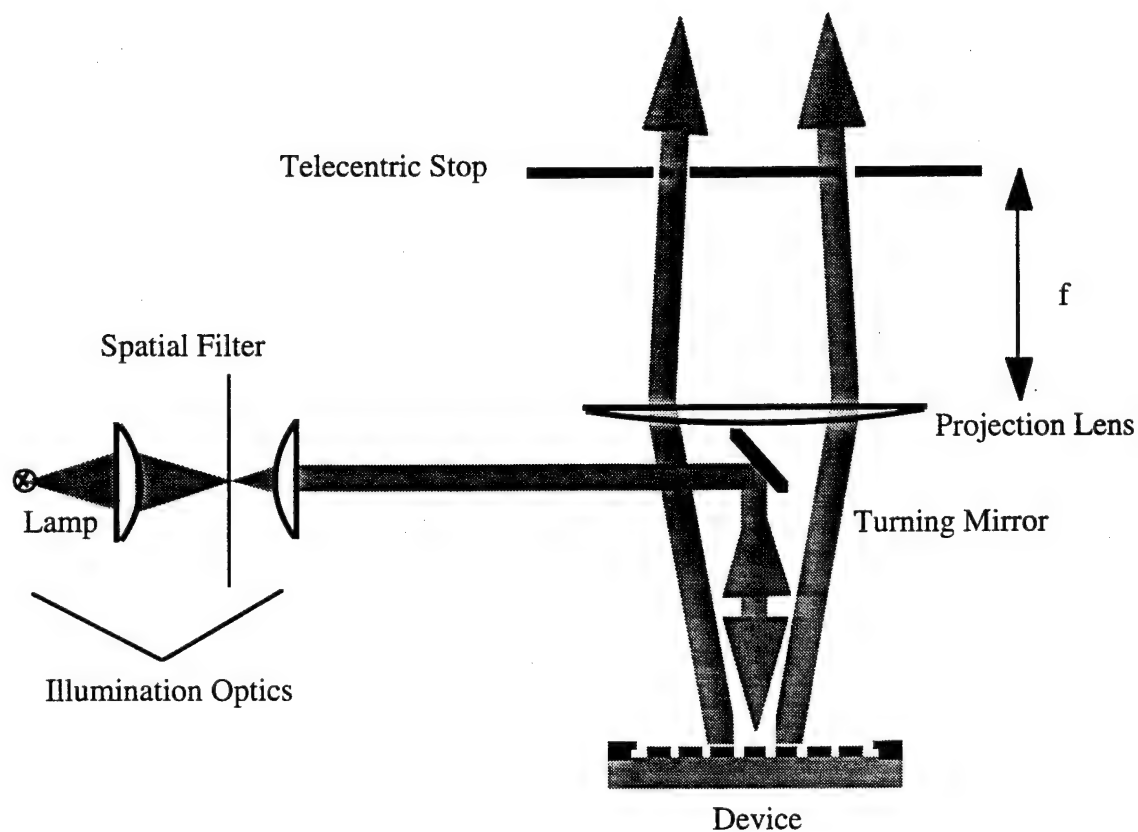


Figure 2.5a: Simple monochrome optical system (I). System I was used as a prototype for a second system, *vide infra*, to do electrical testing (system II) and a third to do optical testing (system III).

System I was used to demonstrate the utility of the GLV for projection and contained a static GLV device. The static GLV device was designed with a fixed, VGA bitmapped image on it. At each pixel of the bitmap, the values for red, green, and blue were quantized to six bits each. At the corresponding location on the static GLV, three pixels

were written, red, green, and blue, and the beam length of each was varied from 0.25 to 16 μm depending on the six bits for each color. A dark pixel was simply left blank. Except for contrast ratio, this static display gives a faithful impression of what a GLV display will look like.

A second system (system II) was constructed for device testing using a microscope/probe station to allow electrical operation of the beams. In this system, the illumination optics were reduced to a tungsten-halogen lamp with integrated collimating reflector. The turning mirror was moved to the side so that the device was illuminated from the diffraction angle. The diffraction angle of the -1 order was then normal to the device. This light was imaged through a microscope objective and eyepiece. The other diffracted modes (+1, ± 2 , ± 3) were discarded. At the telecentric point of the objective lens two strips of black tape were used to define a slit. This system was used for most of the electrical device testing (including hysteresis measurements). A third optical system (system III, see Section 2.4.3) was used to measure the color properties of the GLV.

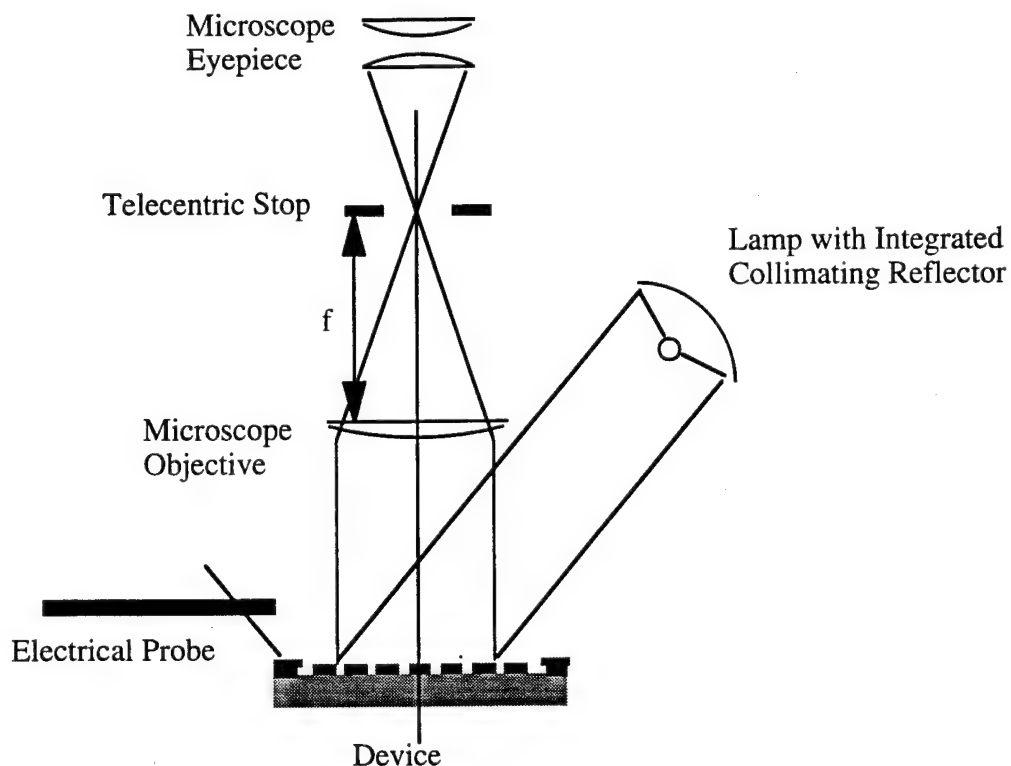


Figure 2.5b: Simple optical system (II) for electrical characterization of devices. This system is constructed on a probe station with microscope.

2.3 Monochrome Contrast Ratio

To understand the difference between dynamic range or extinction ratio, terms used in describing optical modulators, and contrast ratio, it is necessary to discuss the responsivity of the human eye [Hunt 1991] and its effect on perceived brightness. Theoretical and experimental values of the BW contrast ratio are discussed, and the difference is explained as a result of process parameters.

2.3.1 Brightness and Contrast Ratio

Based on subjective descriptions of comparative brightness for different colors, the *Commission Internationale de l'Éclairage* (hereafter CIE) established in 1931 the CIE standard photometric observer. The basis of this observer is the photopic spectral luminous efficiency function, $V(\lambda)$, plotted in Figure 2.6. This function gives the relative brightness of narrowband optical sources of constant optical power over the visible spectrum which peaks at 555 nm. Because of the linearity of the human eye, the apparent brightness, Y_x , of a source with some spectral distribution, $S_x(\lambda)$, is equal to

$$Y_x = \int_{380\text{nm}}^{780\text{nm}} V(\lambda) S_x(\lambda) d\lambda$$

Using the values of $S_x(\lambda)$ for “up” and “down” pixels in Section 2.1.2, the apparent brightness of “up” and “down” pixels can be calculated for a given illumination spectrum, $S_0(\lambda)$. The contrast ratio is defined as $Y_{\text{down}}/Y_{\text{up}}$.

To calculate the narrowband contrast ratio of the GLV, i.e. the contrast ratio for a light-emitting diode (LED) or other narrowband illumination, we take $S_0(\lambda) = \delta(\lambda - \lambda_0)$, where $\delta(\lambda - \lambda_0)$ is the delta distribution at λ_0 . This contrast ratio is plotted vs. λ_0 in Figure 2.7. The narrowband contrast ratio is extremely high at the design wavelength and is still better than 100:1 over nearly 100 nm of spectrum. In the case where the GLV is illuminated with LEDs, contrast ratios of better than 10^4 should be expected—perhaps as high as 10^8 if the device is grown with perfect dimensions and very smooth aluminum.

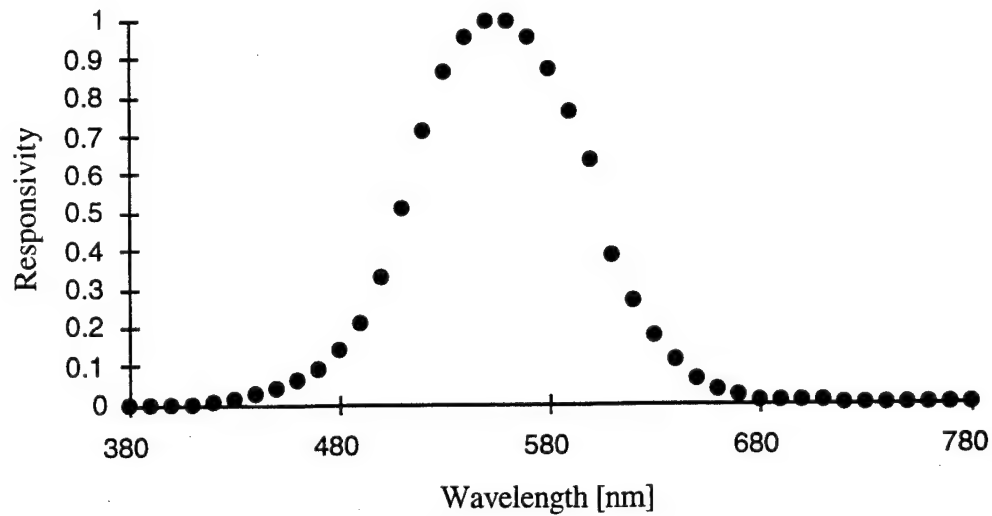


Figure 2.6: BW responsivity of the human eye.[Hunt 1991]

For white light illumination, which is flat over the entire visible spectrum, the contrast ratio is calculated to be 82:1. This value of the contrast ratio is representative of a variety of high-temperature black-body and multiline, white arc sources. It is also representative of contrast ratios seen on existing LCD projectors [Yoshida 1993].

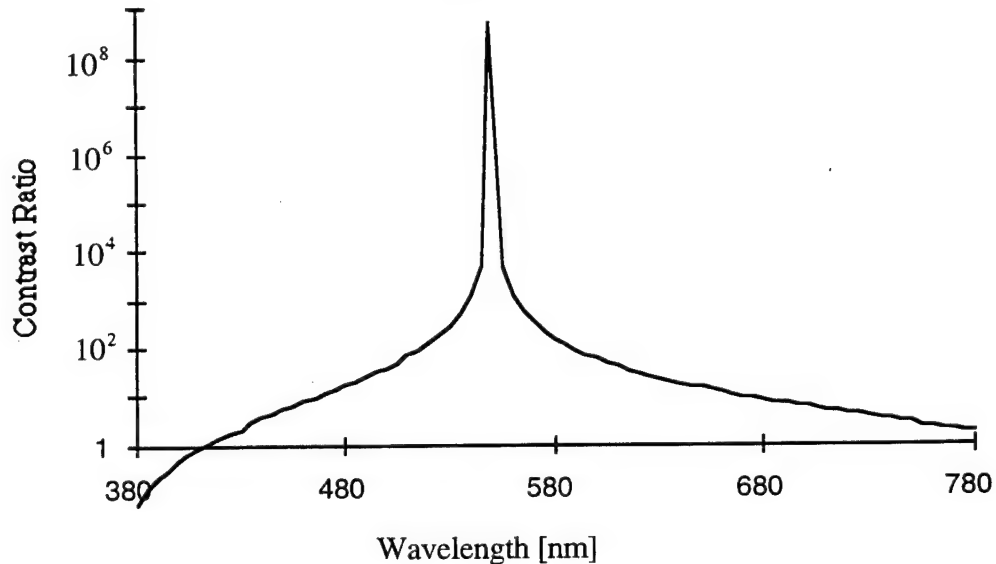


Figure 2.7: BW contrast ratio vs. wavelength for narrowband sources. For narrowband operation, the GLV is capable of operating as an extremely high contrast ratio modulator. For a device optimized for the green the contrast is better than 100:1 from 520 to 580 nm.

Because of the narrowness of the peak of the narrowband contrast ratio, it was feared that the contrast ratio would be a very sensitive function of processing variations, particularly thickness errors that cause wavelength shifts in the optical properties. This hypothesis was tested by recalculating the contrast ratio, as above, but for pixels with design thicknesses other than 555 nm. These contrast ratios are plotted in Figure 2.8 as a function of the change in oxide plus spacer thickness (i.e., a device with design wavelength of 565 nm instead of 555 nm has 10 nm of wavelength error. Since the oxide plus spacer thickness is $\lambda/2$, this corresponds to a 5 nm thickness error). This calculation shows that a few percent error in film growth will not destroy the BW contrast ratio of the device.

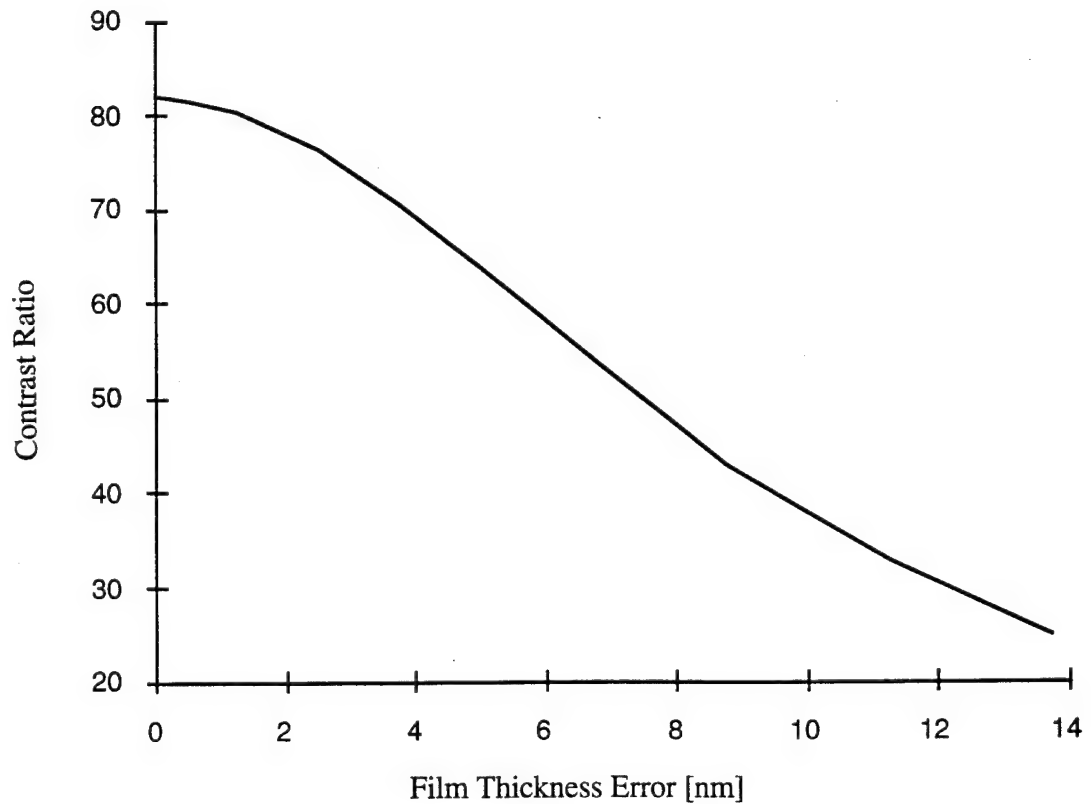


Figure 2.8: BW contrast ratio vs. film thickness error. The contrast ratio is plotted as a function of total film (spacer and beam) thickness error for a pixel with 140 nm total nominal film thickness. Thus, at least 5% control of thicknesses is needed to construct satisfactory contrast ratio devices.

2.3.2 Effect of Etch Anisotropy on Contrast

The measured value of the contrast ratio was 20:1 [Apte 1993]. From Figure 2.8, it is apparent that the fourfold discrepancy from theory cannot be explained by film thickness errors (accuracy to within 5 nm was typical). In fact, the error lies in the quality of the sidewalls of the gratings, and thus in the masking and etching process used. Since the diffraction efficiency of the lower part of the sloped sidewall in the “up,” or dark, case is comparable to that of the “down,” or light, case, the contrast is spoiled by the poor quality of the dark state.

To make the effect of poor sidewalls precise is difficult, since a vector diffraction theory will be needed to handle 500 to 1000 Å features [Gaylord 1982]. A simple estimate is possible using the expression for diffraction given in Section 2.1.2. In this expression the intensity of diffraction as a function of grating depth is given. If we average this expression over the range of heights of the beam—including the downward sloping sidewalls—this gives our estimate of the diffraction efficiency of the “up” beams. The substitution of this value for the denominator in the contrast ratio under white light illumination is plotted in Figure 2.10. A contrast ratio of only 11:1 is expected for 45° sidewalls.

The measured value for the sidewall slope for the nitride etch recipe given in Appendix 2 is 25°, which is measured from SEM photomicrographs. This slope gives a contrast ratio of 21:1. Although the method of this calculation neglects the very fine structures of the the sidewalls and their precise effect upon the diffraction, it seems likely that improved sidewall slopes will result in improved contrast ratio. Work on using metal masks instead of photoresist during the etch step are being explored for this reason.

2.4 Color Operation

By using the dispersive properties of the grating [Born 1980] the GLV can act both as a light valve and a color filter. For a diffraction grating with normally incident illumination and period, p , the relationship between diffraction angle, θ , wavelength, λ , and order number, m , is given by

$$\sin \theta = m \frac{\lambda}{p}$$

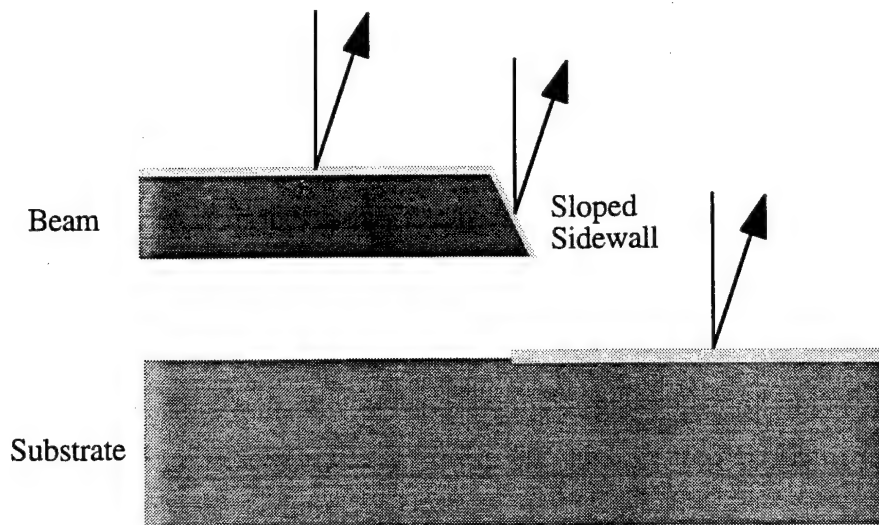


Figure 2.9: Effect of bad sidewalls on contrast ratio. If the sidewalls of the beams are sloped by insufficient anisotropy of the beam etch or unsatisfactory masking, then the lower parts of the slope are at the height for maximum diffraction. Poor contrast results.

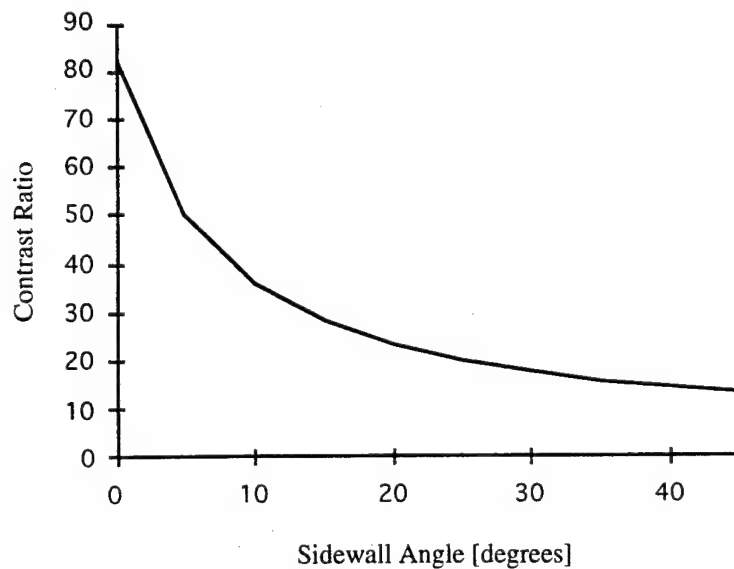


Figure 2.10: Contrast ratio vs. sidewall angle. This figure demonstrates the importance of good anisotropy and masking for the grating beam etch step.

For the first order, in the case of small angles, this reduces to $\theta = \lambda/p$. Thus, if an optical system is constructed that accepts diffracted rays from only a narrow set of angles, $\theta_0 \pm \partial\theta$, then it will image the GLV only in the spectral range

$$\lambda_0 \pm \partial\lambda = p_0(\theta_0 \pm \partial\theta)$$

In order to image the GLV at λ_i which is not in $\lambda_0 \pm \partial\lambda$, we choose another value for the periodicity of the grating, p_i , so that

$$\theta_0 \pm \partial\theta = \frac{\lambda_i \pm \partial\lambda}{p_i}$$

Thus, it is possible to choose three different grating periodicities such that each one diffracts a different wavelength through the same diffraction angle and thus through the same slit in the telecentric stop. This is a general process that could be used for more sophisticated additive color systems than the usual red-green-blue (RGB) of the National Television Standards Committee (hereafter NTSC). The optics of such a system are shown in Figure 2.12, which shows the third optical system used with the GLV [Hopkins 1992]. The basic innovation of this system is to place the collimating lens onto the face of the grating package. This puts the collimating lens into the optical path of the diffracted light. Before a discussion of the design of color devices, a review of human color perception and colorimetry is presented.

2.4.1 CIE Color Coordinates

The responsivities of the three types of cones in the human eye [Hunt 1991] are plotted in Figure 2.11. If these could be measured accurately for a large number of individuals, then they could form the basis of a color coordinate system. Since this study was not possible, an alternative methodology was arrived at which used color matching experiments. An observer was presented with two illuminated boxes, one with an unknown source, and the other with variable amounts of red, green and blue (which are defined in this case at 700 nm, 546.1 nm, and 435.8 nm and termed R, G and B). The observer then changed the amounts of R, G and B until he matched the unknown source. Assuming that the brightness of the unknown source is such that $R+G+B$ is constant (ie, brightness is not a factor), then the color of the unknown source could be described by (R,G) .

This explanation oversimplifies the basis of colorimetry, but gives a flavor of how to interpret CIE color coordinates (x, y): x is the amount of red; y is the amount of green; and when both decrease the color is blue (since aggregate brightness is constant). Because of complications in the system, the range of visible colors is not described by a simple geometry in the x, y plane but by a rounded triangle. The edge of the triangle consists of highly saturated colors, like laser or LED illumination. In the center, with equal mixes of red, blue, and green, are shades of white. Thus, moving from the center to the edge of the triangle increases saturation. Moving clockwise increases wavelength. See Figure 2.13.

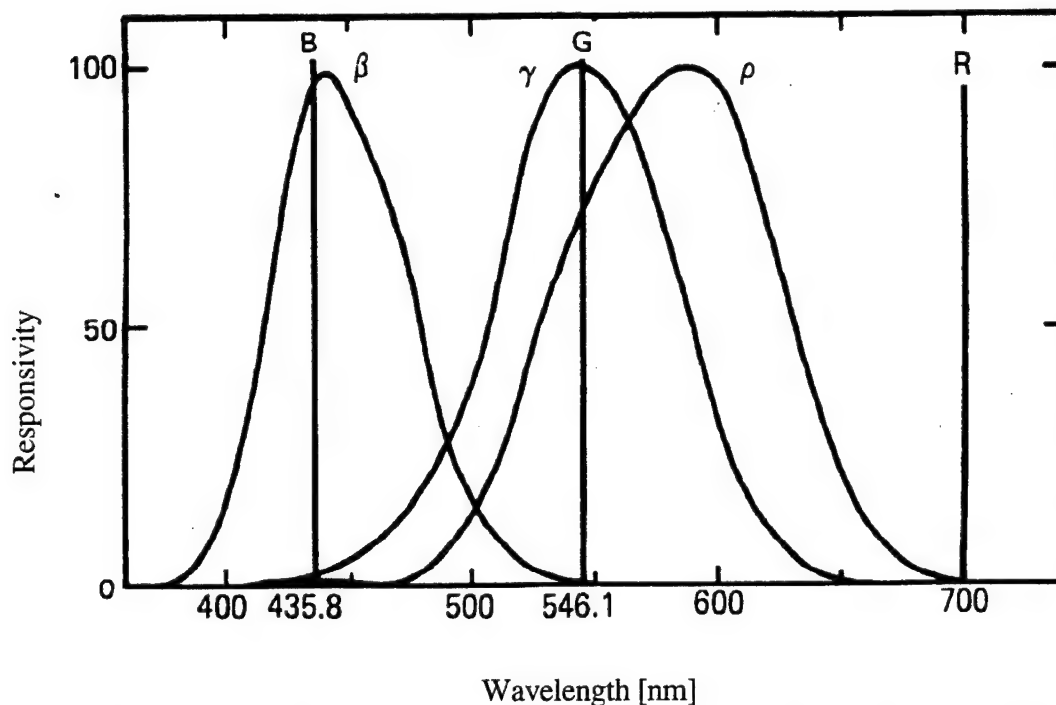


Figure 2.11: Color responsivity of the human eye. β , γ , and ρ are the spectral responsivities of the three types of cones in the human eye. B, G, and R are the spectral lines used to define the 1931 CIE Standard Colorimetric Observer. [Hunt 1991]

If a display is constructed with three color sources, such as a color TV with three phosphors, then each color source may be plotted on the x, y plane. The set of all the perceived colors made by mixing these three sources in varying ratios is called the “gamut” of the colors. Because of the linearity of the human eye and the CIE color coordinate definition, the coordinates of all of the colors in the gamut defined by three

primary sources form the triangle in the x,y plane defined by the coordinate of the primaries.

2.4.2 Color Design

The procedure for designing a color GLV then reduces to the question of how to design the gratings and slits to achieve a desired color gamut. For reasons of compatibility with existing technology, the target gamut is the NTSC phosphor primaries. Since the optical systems we used have a common slit for all three colors to pass through, the key parameters in color design are the choice of center wavelengths, the slit position, and the slit width. Referring again to Figure 2.12, the slit position is given by $f \frac{\lambda_0}{p_0}$. The slit width by $f \frac{\partial \lambda}{p_0}$. Thus, the design consists of choosing values for p_0 , λ_0 , λ_1 , λ_2 , and $\partial \lambda$.

If p_0 is large, then the diffraction angle is small and it may be difficult to spatially separate the diffracted light from the lamp mechanically. Also, the collimation requirements will be higher (*vide infra*). If p_0 is too small, then the lithography becomes more difficult and the the diffraction angles become very large. In this case, scalar diffraction theory breaks down, and the grating depth for a null in the specular reflection no longer coincides with the peak in first order diffraction. An intermediate value of $p_0 = 2.25 \mu m$ was chosen to yield high first order diffraction efficiency at a workable angle.

Wavelength [nm]	Periodicity theory [μm]	Periodicity exp. [μm]	Diffraction Angle [mrad]	x,y theory	x,y measured	x,y NTSC
625 ± 30	2.65	2.75	236 ± 13	0.66, 0.33	0.54, 0.41	0.67, 0.33
530 ± 30	2.25	2.25	—	0.22, 0.71	0.31, 0.62	0.21, 0.71
465 ± 30	1.97	2.00	—	0.14, 0.05	0.17, 0.04	0.14, 0.08

Table 2.1: Basic values of color parameters.

The choices of λ_0 , λ_1 , λ_2 , and $\partial\lambda$ are governed by colorimetry. A white source spectrum $S(\lambda)$ was chosen for generality. It is also a good approximation for a blackbody source at 3500°K, such as a tungsten halogen lamp. After the illumination spectrum was chosen, it was chopped into three possibly overlapping segments, $\lambda_0 \pm \partial\lambda$, $\lambda_1 \pm \partial\lambda$, and $\lambda_2 \pm \partial\lambda$. The color coordinates of each segment were calculated while λ_0 , λ_1 , λ_2 , and $\partial\lambda$ were varied. Since making $\partial\lambda$ as large as possible would result in a minimum of light being wasted at the telecentric stop, $\partial\lambda$ was increased from zero until the color coordinates showed signs of decreasing saturation relative to the NTSC standard phosphors; a value of 30 nm matched the saturation of the NTSC phosphors. λ_0 , λ_1 , and λ_2 were selected by trying to match the wavelengths of green, red, and blue phosphors. The resulting values are summarized in Table 2.1 and plotted in Figure 2.13. A photomicrograph of the pixels themselves is shown in Photograph 2.1.

The color coordinates were measured with a spectra-colorimeter [Photo Research 1992] and are presented in 1931 CIE color coordinates [Hunt 1991]. Figure 2.13 shows the NTSC color gamut along with the theoretical and experimental gamuts. There is a definite loss of saturation of the green and red, although the blue is well-saturated. Figure 2.14 shows the color as a function of diffraction angle. From this plot it is clear that the problem is primarily in the collimation of the incident light: in the absence of good collimation, it is possible to saturate the red and blue by over-tuning, without ever getting a saturated green. For example, if the grating is over-tuned to the blue, then its spectrum will be mostly violet, regardless of the grating pitch. Although there is a loss of brightness (and contrast), it is possible to saturate the color fully. The same is also true of the red, since both red and blue are at the ends of the visible spectrum. The green primary is impossible to over-tune. Thus, the fact that the green coordinate is unsaturated in Figure 2.14 indicates that poor collimation is causing wavelengths outside the 530 ± 30 nm to pass through the slit. To correct this, an angular source size of less than 13 mrad is needed, which corresponds to a linear source dimension of 0.65 mm. A source of approximately 1.0 mm was used.

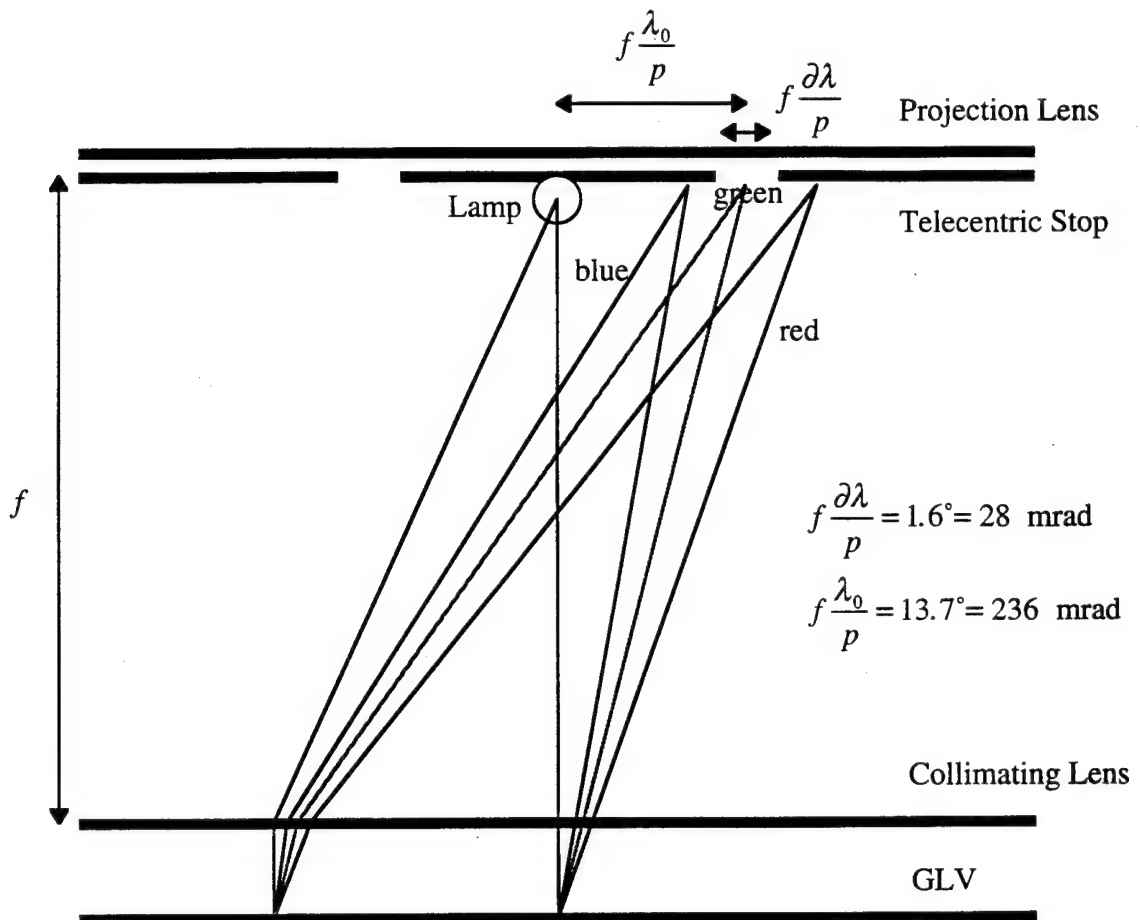
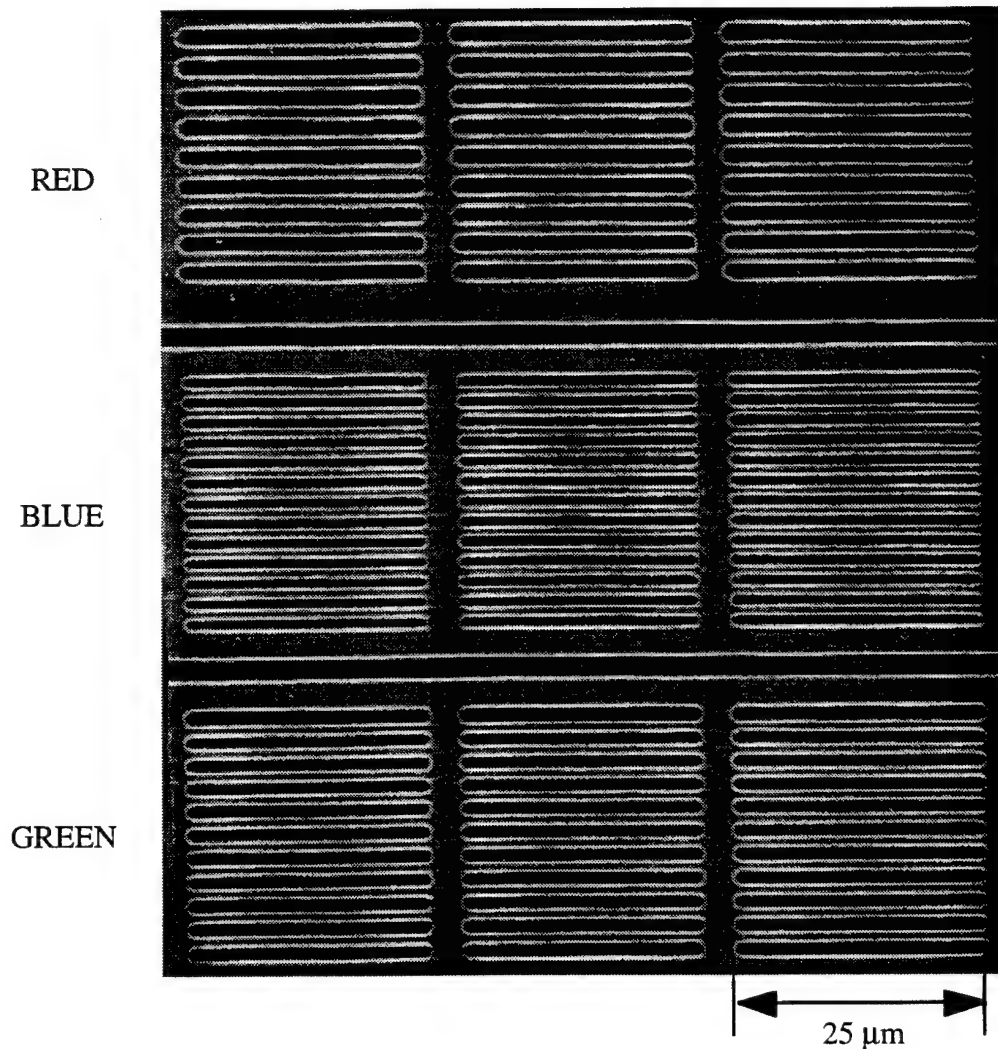


Figure 2.12: Basic optics of Schlieren system (III). This optical system places the lamp collimating lens in the diffracted light path. This innovation produces a very compact, folded optical system. The lamp illumination is collimated at the Collimating Lens. This light strikes the GLV normally, and a diffraction spectrum is produced a focal length away at the Telecentric Stop. Only a portion of the spectrum passes through, depending on the periodicity of the grating. Not shown is an eyepiece or viewer.



Photograph 2.1: SEM of color pixels. The first row corresponds to red, the second blue, and the third green. Each row consists of a series of devices (three are shown) that are electrically connected, which is why each pixel lacks a separate frame.

2.5 Color Contrast Ratio

The contrast ratio in the color case is not a simple function of device geometry. Rather, it is a function of the type of system used to project the color, the number of light valves, the number of mask levels, and how the contrast is defined. We will examine two types of systems under two definitions. The unoptimized case has a single light valve with only one beam/spacer thickness. This will ordinarily be optimized for the green. The second case is for a projector with three light valves, each optimized for a single color, or for a projector with a single light valve that has three different beam/spacer thicknesses.

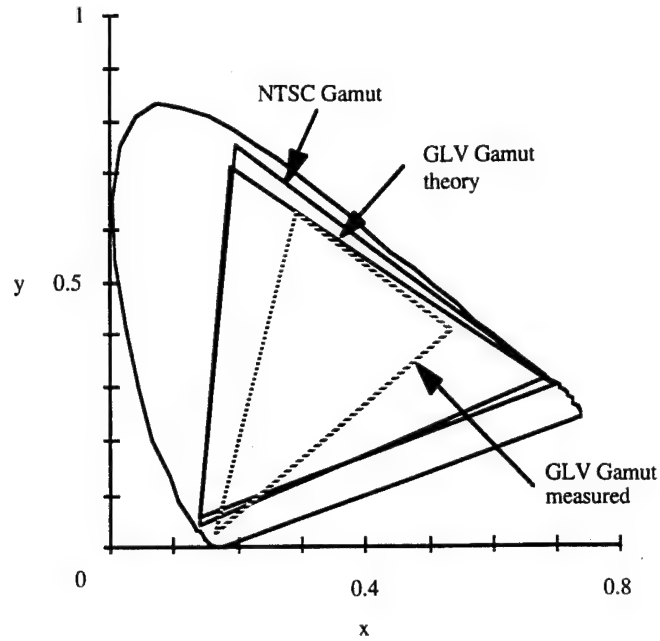


Figure 2.13: Measured color coordinates and theoretical values of the GLV with NTSC phosphor standards and the visible gamut. The outer ring indicates the visible gamut.

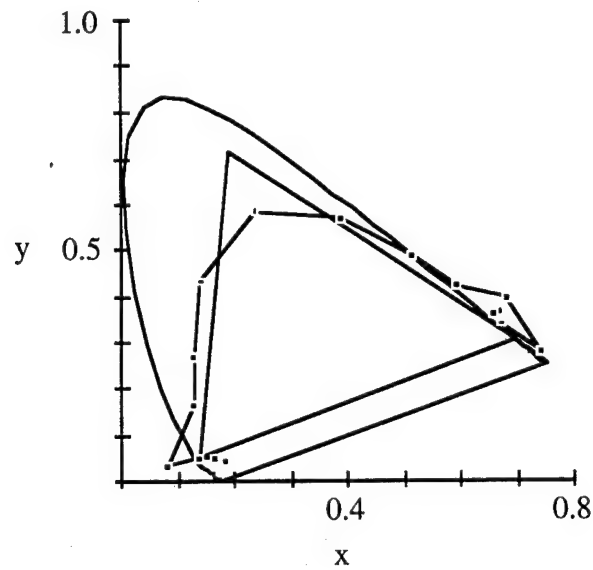


Figure 2.14: Color coordinates of green pixel as a function of diffraction angle. The angle is varied from 160 to 320 mrad. Points outside the edge of the rounded triangle of visible light are noisy.

The unoptimized case is typical of a low cost and weight product, while the optimized case is for higher performance.

The monochrome contrast ratio is the “on” brightness divided by the “off” brightness of a single pixel of a single color. The pixel contrast ratio assumes that each pixel consists of a RGB triad of devices. The pixel contrast ratio is the “on” brightness of a single device divided by the “off” brightness of the whole triad. The values of monochrome and pixel contrast ratios for both unoptimized and optimized systems are given in Tables 2.2 and 2.3. These calculations assume that the devices do not scatter light, have perfect sidewalls and have high beam/spacer thickness uniformity.

Color	Monochrome Contrast Ratio	Pixel Contrast Ratio
red	20	36
green	341	59
blue	22	6

Table 2.2: Contrast ratio for unoptimized system.

Color	Monochrome Contrast Ratio	Pixel Contrast Ratio
red	434	78
green	341	257
blue	375	27

Table 2.3: Contrast ratio for optimized system.

2.6 Pixel Size Limits

The GLV exhibits very high pixel densities. Early devices were constructed with 20 x 25 μm frames. The most recent devices, with shorter beams, are 20 x 15 μm . This gives a monochrome pixel density of 0.33 megapixel/ cm^2 , or a color density of 0.11 megapixel/ cm^2 . The question arises, how much further can the pixel size be reduced?

The basic expression for diffraction from a pixel is [Solgaard 1992]

$$I = I_0 (\text{Diff Order Intensities}) \left(\frac{\sin N\alpha}{\alpha} \right)^2,$$

where $\alpha = \frac{\pi p}{\lambda} \sin \theta$. The width of the central lobe is given by

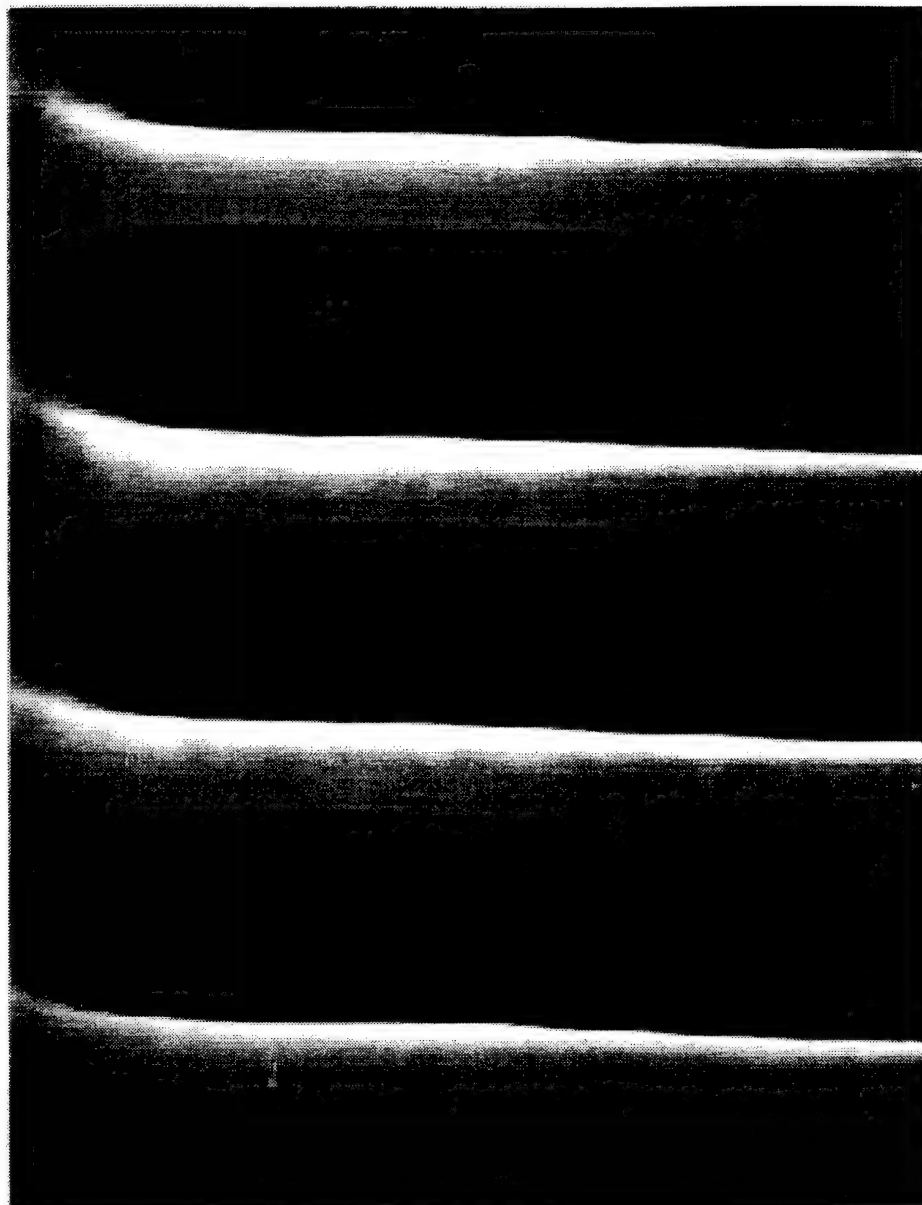
$$\sin \partial \theta = \frac{\lambda}{Np} < \frac{\partial \lambda}{p}$$

so the condition on N, the number of grating lines, for green light, $\lambda = 530 \text{ nm}$ and $\partial \lambda = 60 \text{ nm}$, is

$$N > \frac{\lambda}{\partial \lambda} = 8.8$$

This sets the limit on color pixels as $8.8 \times 2.25 = 19.9 \mu\text{m}$ across. For BW pixels $\partial \lambda = 200 \text{ nm}$ and the limit is three times smaller: $7 \mu\text{m}$.

In the other direction, along the length of the beams, the limit is given by the aperture ratio. As the beams get shorter both the switching voltage and the amount of undeflectable beam at the ends increase. Since approximately $3 \mu\text{m}$ of the beam is wasted ($4 \mu\text{m}$ is more typical, but this includes the $0.5 \mu\text{m}$ of the frame that is undercut), it is impractical to make a pixel shorter than $10 \mu\text{m}$. See Photograph 2.2. The one exception is if singly-supported cantilevers are used instead of doubly-supported beams. In this case pixels might be shortened to $6 \mu\text{m}$ with a 50% aperture ratio.



Photograph 2.2: Sideview of stuck beams. This micrograph shows the distance over which the beams bend to the substrate.

Chapter 3

Mechanics of the GLV

3.1 Basics of hysteresis

The most striking feature of the mechanical operation of the GLV is the hysteresis of the deflection of the beams —and hence diffraction efficiency—as a function of applied voltage. Mechanical models of the deflection can provide scaling laws to help design and control the hysteresis. Two models will be presented, one analytical and one numerical. In both cases the reason for the hysteresis is the same, that the electrostatic attraction between the top and bottom electrodes is a nonlinear function of deflection while the mechanical restoring force caused by the beam stiffness and tension is linear. This is shown in Figure 3.1.

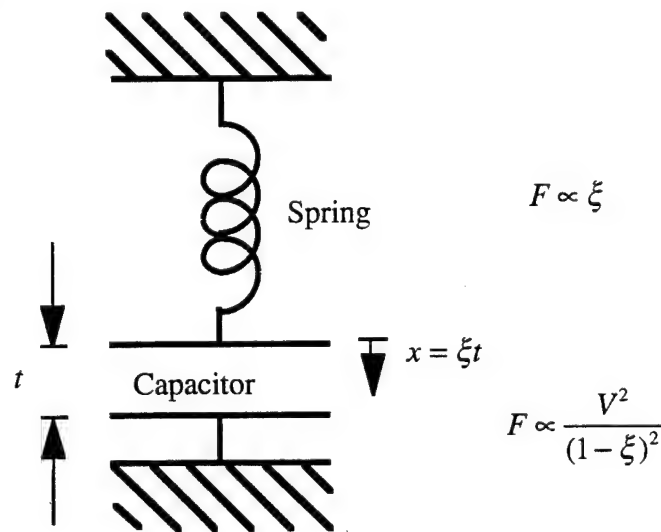


Figure 3.1: Basic model for the GLV beam mechanics. The spring represents the restoring force caused by the beam stiffness and tension. The capacitor represents the electrostatic attraction between the electrodes.

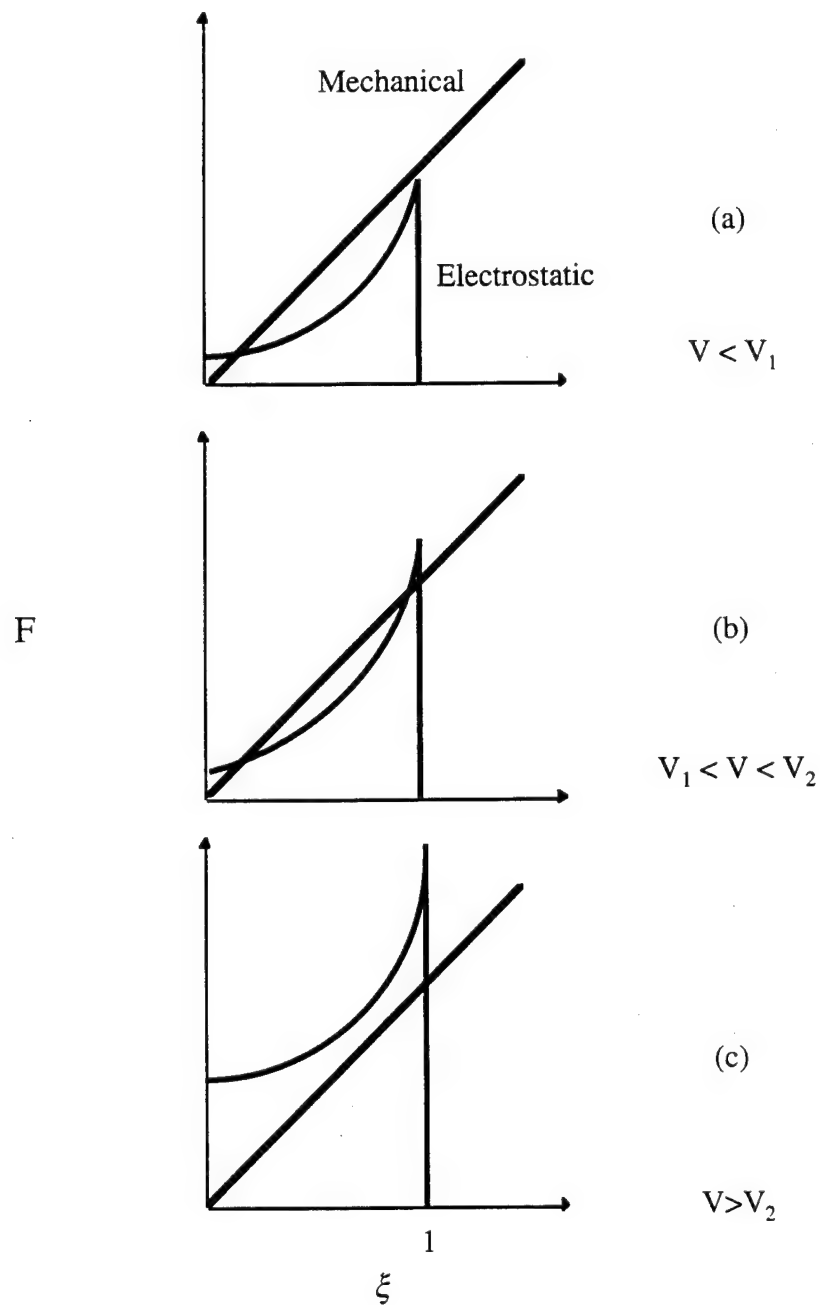


Figure 3.2: Origin of hysteresis. These curves plot electrostatic and mechanical forces as a function of normalized displacement (see Figure 3.1 for equations). When the applied voltage $V < V_1$, the first instability voltage, there is one stable solution in which the forces balance (a). If V is increased past V_1 , then there are two stable solutions, one up and one down (b). For $V > V_2$, the second instability voltage, the beam must be in the down position, pinned to the substrate.

The source of the first equation in Figure 3.1 is a linear approximation of the deflection of beams with force. Unless the beam material violates Hooke's law, this approximation is sound. The second equation is the nonlinear force between the plates of a capacitor. The consequence of this nonlinearity of the electrostatic force is shown more clearly in Figure 3.2. The two curves for spring and electrostatic force are plotted vs. normalized displacement of the center of the beam for three voltage ranges. For small voltages, there is only one "load line" solution, in which the beam is slightly deflected. For intermediate voltages there are two solutions, one lightly deflected and the other in full contact with the substrate. For large voltages, the only stable solution is in full contact with the substrate. Thus, the device shows a hysteresis reminiscent of a magnetic core.

The simplest model for the mechanical operation of the beams of the DGLV neglects the moment of inertia of the beams. In this case the beam is considered as a string under tension, and the electrostatic force that drives the beam is lumped into the center of the beam. While the first approximation will be shown to be rigorous, the second is a major source of error, since it tends to dramatically underestimate the voltage needed to switch the beams. This fact is mitigated by the utility of the string model in examining scaling laws in analytic form, which is not possible with the numerical simulations that are in agreement with measured switching voltages.

3.2 Materials Parameters

The materials parameters and nominal geometry of the beams are given in Table 3.2. In this development we treat the beam and spacer thicknesses as equal. The Young's Modulus of our samples is imperfectly known. Measurements done with samples from the same LPCVD furnace give 200 ± 100 GPa [Hong 1990]. However, other workers have reported inconsistent values for similar growth conditions [Kiesewetter 1992]. The average tension in the beams was determined using a scanning Helium Neon laser deflection system [Flinn 1987] as a function of dichlorosilane to ammonia flows within the furnace [Beck 1990].

Parameter	Symbol	Value
Young's Modulus	E	200 ± 100 GPa
Average Intrinsic Tension	T	100- 800 MPa
Optical Index of Refraction	n	2.0 - 2.39
Relative Permittivity	ε	6.45
Top Electrode Thickness		400 Å
Bot. Electrode Thickness		3000 - 6000 Å
Isolation Thickness		5000 Å
Spacer Thickness	t	1325 Å
Beam Thickness	t	1325 Å
Beam Width	w	1.0 - 1.5 μm
Beam Length	L	6 - 40 μm
Area Moment of Inertia	I	$\frac{wt^3}{12} = 2.4 \times 10^{-4} \mu\text{m}^4$

Table 3.1: Basic physical and geometric factors of the GLV.

Dichlorosilane/Ammonia Flow	Residual Stress	Index of Refraction
1.0	800 MPa	2.04
3.0	420 MPa	2.19
5.2	80 MPa	2.38

Table 3.2: Three different types of nitride in use.

3.3 String Model

The force on a string, for small deflections at a point at the center, is linear. (See Figure 3.3 and Table 3.1 for definitions). x is the deflection of the beam at the center, $\xi = x/t$, and K is a parameter in units of force.

$$F = \frac{4 T t w}{L} x = K \xi$$

For the case that $L = 15 \mu\text{m}$ and $T = 800 \text{ MPa}$ we have $K = 3.75 \mu\text{N}$, which is the scale of the restoring force on a single beam element. The electrostatic force [Solgaard 1992] is a function of the applied voltage, v . The dimensionless parameter V is defined below.

$$F = \frac{1}{2} \frac{\epsilon_0 L w v^2}{(t-x)^2} = \frac{V^2}{(1-\xi)^2}$$

In this case we have neglected the finite contribution to the capacitance from the dielectric in the beam. When the beam is up, this contribution increases the capacitance by $1/\epsilon_r \approx 16\%$. At the inflection point the effect is 10%. The parameters are:

$$K = \frac{4Tt^2w}{L}$$

and

$$V = \sqrt{\frac{\epsilon_0 L w v^2}{t^2}}$$

The condition for the second instability point is that the number of crossing points in Figure 3.2 decreases from three to one. The force and spring constants of the electrostatic attraction and the beam tension must be equal, which is equivalent to saying that the second instability point occurs when the spring line is tangent to the nonlinear electrostatic curve.

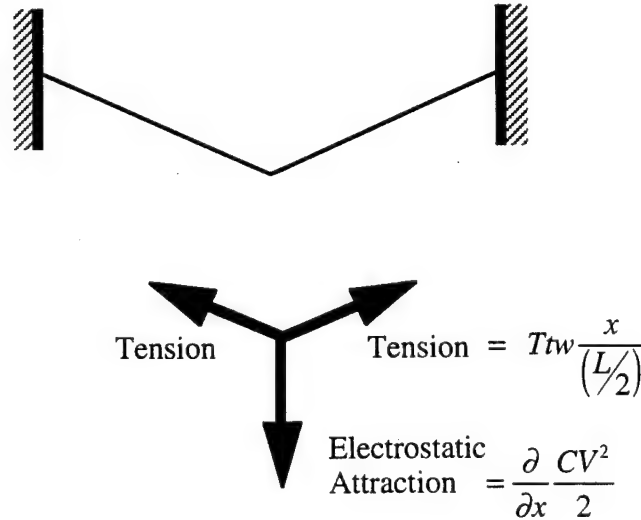


Figure 3.3: Modelling beams as strings. The upward restoring force is caused by tensile stress T in the beams, while the downward electrostatic attraction is the derivative of the stored energy in the beam capacitance, C , with deflection x .

The solution for the second instability point is

$$\xi_2 = \frac{x}{t} = \frac{1}{3}.$$

Thus, the instability point, beyond which the beam collapses with increasing voltage to the substrate, occurs at one-third deflection. As the voltage is retarded, the beam will spring up at the first instability point. This is given by

$$K = \epsilon_r^2 V_1^2.$$

If we now proceed to solve for the second instability voltage, we have

$$V_2 = \sqrt{\frac{32}{27} \frac{T}{\epsilon_0} \frac{t^2}{L}}$$

and

$$V_1 = \sqrt{\frac{27}{4\epsilon_r^2}} V_2 \approx 0.4 V_2$$

Numerically, these expressions underestimate the instability voltages by a factor of 2 compared to experiment. This is because of the assumption that the entire distributed electrostatic attraction is focused at the center of the beam. Nevertheless, the string model accurately predicts the scaling behavior of the switching voltage. Extreme sensitivity to material thickness has been observed, as well as the inverse linear dependence on beam length. Finally, a weak dependence on stress levels has been observed as well. This data will be presented in Section 3.4.1.

There are two major deficiencies with the string model. The first, which is minor, is that the model assumes the beams are long and floppy. An analysis that includes the finite stiffness of the beams gives [Cho 1992]

$$V_2^2 = \frac{8}{27} \frac{t^4 k T}{e_0 L \left(\frac{kL}{4} - \tanh \frac{kL}{4} \right)},$$

where $k = \sqrt{\frac{Tw}{EI}}$. For our geometries, $k = 4 \mu\text{m}^{-1}$, $kL \gg 1$, and this expression reduces to the previous one. Thus, this error seems minor. However, when predicting the profile

of the beams near the spacer, the beam stiffness becomes important. The second shortcoming is that the deflecting force is lumped into the center of the beam, rather than distributed along the length. To overcome both of these problems, a numerical model was constructed to predict switching voltages more accurately.

3.4 Beam Model

The beam model overcomes both failures of the string model and gives accurate results for switching voltages. It is based on solving the 4th order beam equation [Hartog 1961]:

$$y^{(4)} - \frac{T}{EI} y^{(2)} - \frac{W}{EI} = 0$$

for the local deflection $y(l)$, a function of the position l along the beam. $W(y)$ is the one-dimensional electrostatic pressure (N/m) forcing function

$$W(y) = \frac{\epsilon_0 w V^2}{2t^2} \frac{1}{\left(1 - \frac{y}{t(1 + 1/\epsilon_r)}\right)^2}$$

This inhomogeneous, nonlinear equation is best solved by the method of Green's functions with self-consistency. First, the equation is solved assuming that the forcing function is the delta function at position a . For $l < a$ the solution is $\tilde{y}(l; a) = y_1(l)$, and for $l > a$ the solution is $\tilde{y}(l; a) = y_2(l)$. Then, using an assumed beam displacement function ${}^0y(l)$ we calculate a trial forcing function ${}^0W({}^0y(l))$. A new displacement function is generated by convolving Green's function with the trial forcing function:

$${}^{n+1}y(l) = \tilde{y}(l; a) * {}^nW({}^ny(a))$$

The iterations are performed until $\|{}^{n+1}y(l) - {}^ny(l)\|$ is small. The algorithm can be made efficient by sampling the beam position at n grid points. In this case, $\tilde{y}(l; a)$ is an $n \times n$ matrix, and the convolution is a matrix multiplication.

To calculate $y_1(l)$ and $y_2(l)$ the homogeneous equation must be solved:

$$y^{(4)} - \frac{wtT}{EI} y^{(2)} = 0$$

and the boundary conditions are, for a unity magnitude delta functional at position a are:

$$\begin{aligned}
 y_1(0) &= 0 \\
 y_2(L) &= 0 \\
 y_1^{(1)}(0) &= 0 \\
 y_2^{(1)}(L) &= 0 \\
 y_1(a) &= y_2(a) \\
 y_1^{(1)}(a) &= y_2^{(1)}(a) \\
 y_1^{(2)}(a) &= y_2^{(2)}(a)
 \end{aligned}$$

and

$$y_1^{(3)}(a) - y_2^{(3)}(a) + 1 = 0$$

These boundary conditions are derived by integrating the delta function-forced beam equation from $a - \delta$ to $a + \delta$. The homogeneous solutions are simple exponentials

$$\begin{aligned}
 y_1(l) &= a_1 + b_1 x + c_1 e^{l\sqrt{\gamma/EI}} + d_1 e^{-l\sqrt{\gamma/EI}} \\
 y_2(l) &= a_2 + b_2 x + c_2 e^{l\sqrt{\gamma/EI}} + d_2 e^{-l\sqrt{\gamma/EI}}
 \end{aligned}$$

Solution of these eight equations in 8 unknowns used a commercial math package [Wolfram 1991].

While many of the details of the solution are straightforward, one subtlety arose during the analysis: how to model the hard contact between the collapsed beam and the substrate. This is not a trivial problem. In this case we assumed that the substrate was springy, i.e. that it responded with a force proportional to the amount it was compressed. Some tuning of this parameter was needed to help keep the deflection iterations from oscillating. While for the present analysis this proved sufficient, any further modeling must include a viscous damping term to keep the solution from vibrating. It must be noted that oscillations in the solution are physical, in the sense that in vacuum the beams do vibrate with high Q [Solgaard 1992]. The viscous term must then represent the damping of air on the motion of the beam.

3.4.1 Switching Voltage

The first question we addressed with the beam model was the prediction of the second instability voltage (switching voltage). The experimental data are given in Table 3.3. The simulation results are in Figure 3.4.

Stress [MPa]	Beam Length[μm]	Voltage, V_2
800	20	18
800	16	26
400	16	18
100	16	11

Table 3.3: Experimental second instability voltages.

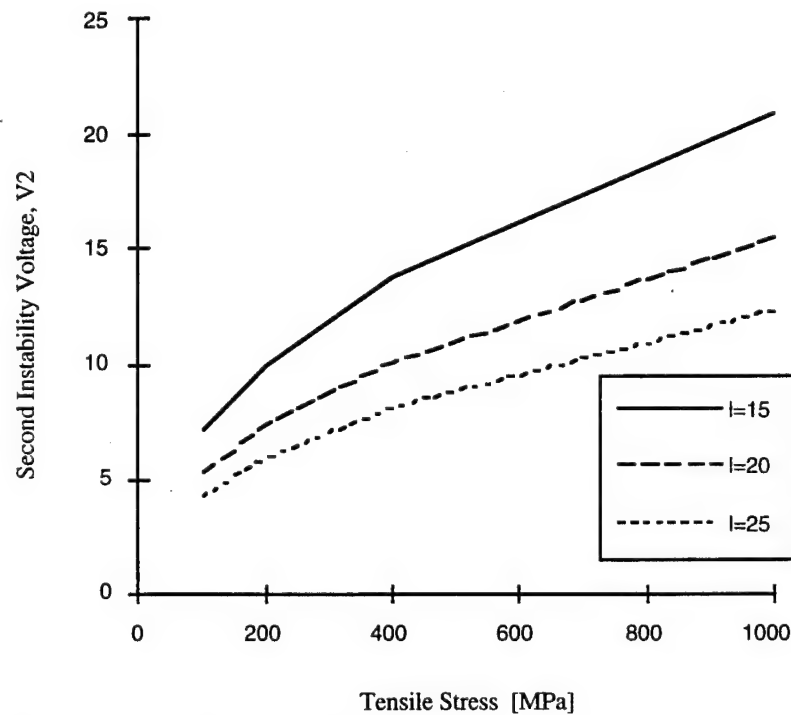


Figure 3.4: Results of beam model. Second instability voltage is plotted as a function of nitride tensile stress for three different length beams, 15 μm , 20 μm , and 25 μm .

The simulated values are approximately 25% lower than the measured values, with no fitting parameters. As can be seen, the results are also consistent with the scaling laws pertaining to length and intrinsic stress. The underestimation of both the string and beam

models may be due to a common error, the use of the semi-infinite parallel plate capacitor model for the beam attraction. Since the gap to width ratio is about 1:10, stray field lines may decrease the capacitance enough to account for part of the 25% error. Two material parameters that are poorly known, Young's modulus and the dielectric constant of nitride, may also contribute. The dominant contribution is probably due to the addition of top electrode aluminum to the beams.

3.4.2 Peak Stress

The yield stress of our LPCVD nitride is not well known, so it is not possible to definitively determine how dangerous stress concentrations in the beams will be. According to the bending seen in SEM micrographs and the beam model, it takes a beam from 2 to 4 microns to deform down to the substrate. This means that the increase of peak stress over the average stress[Den Hartog 1949] is less than 400 MPa.

$$s = -\frac{1}{2}Et \frac{\partial \alpha}{\partial z}$$

where s is peak stress minus the average stress, z is the direction along the length of the beam, and α is the angle between the tangent to the beam at z and the horizontal. The expression can be evaluated in the string model to give an estimate of the peak stress. Thus the maximum stress seen in high-stress devices is 1.2 GPa (400 MPa plus 800 MPa average stress), while the yield stress is nominally 14 GPa [Petersen 1982] (this value was measured for much thicker films and for only one reagent gas ratio). It is likely that stress concentrations due to surface roughness or cracks could produce much large stress concentrations.

3.4.3 Hysteresis

A simulation of deflection of the center of a beam in the beam model as a function of voltage is presented in Figure 3.5. The hysteresis width is represented quite well by $V_1 \approx 0.4V_2$, which was derived for the string model. The openness of the curve may be useful in passive-matrix addressing. Also, as per the string model, the normalized deflection at the second instability point is less than the 0.33 predicted by the string model.

In Figure 3.6 is a measured hysteresis curve for a single pixel on a striated substrate (as described in Section 4.4.5). Optical system II was used to make the measurement, with a

CCD camera in the microscope frame as the detector. There is a significant dark current in the CCD, so no contrast data can be taken from this curve.

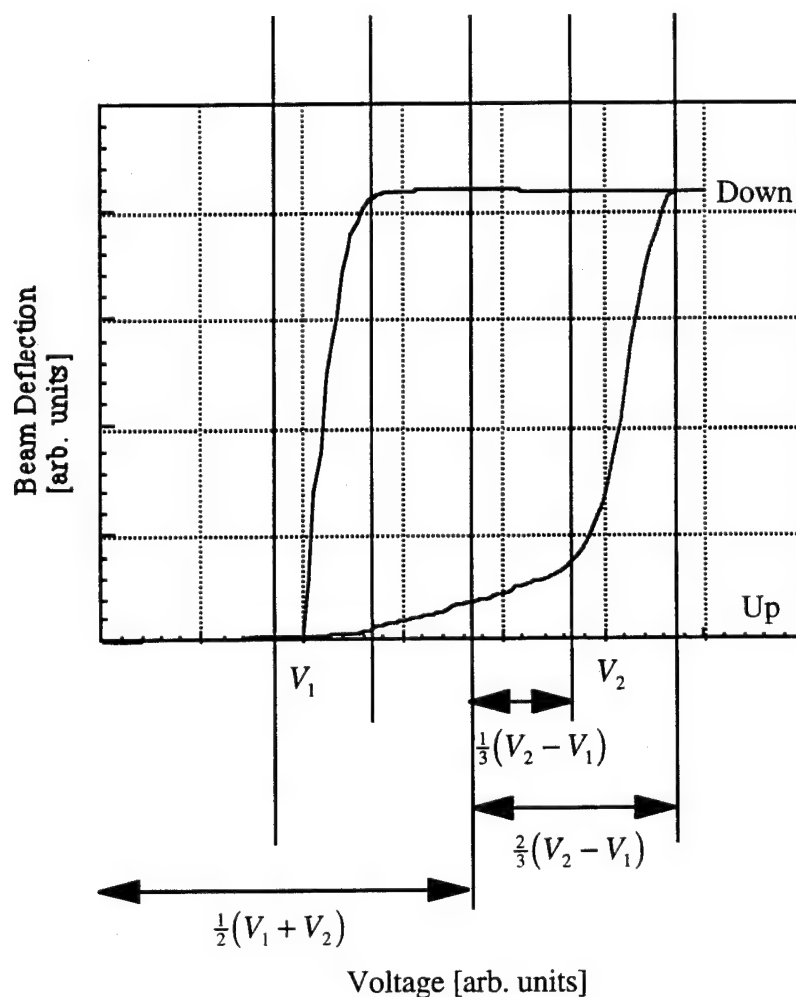


Figure 3.5: Simulated hysteresis curve. Note that $V_1 \approx 0.4V_2$, and that the beam is deflected by less than $1/3$ at V_2 .

3.5 Row-addressing Method

The use of inherent device bistability for a passively driven array of devices is a unique feature of micromechanical displays. Passive matrix row-addressing uses three state drivers. Rows are biased at ground, and the columns are biased at $(V_1 + V_2)/2$. See Figure 3.5. The frame is addressed twice, once to turn on pixels that are off, and the other to turn off pixels that are on. In the first case, the row is selected by applying $-(V_2 - V_1)/3$. Individual columns are turned on by applying $(V_1 + V_2)/2 + (V_2 - V_1)/3$. In this case the total voltage across the desired pixel is greater than V_2 , so the pixel turns

on. The voltages on pixels in other rows and columns are all between V_1 and V_2 , so no pixels switch. Similarly, to turn on pixels off, the rows are grounded except for one, to which $+(V_2 - V_1)/3$ is applied. The columns that are to be unchanged remain at $(V_1 + V_2)/2$, but to the columns to be switched is applied $(V_1 + V_2)/2 - (V_2 - V_1)/3$. The desired pixel then has $(V_1 + V_2)/2 - 2(V_2 - V_1)/3$, which is less than V_1 , so the pixel switches off. Other pixels are left between V_1 and V_2 and do not switch. In this case, at the cost of addressing the frame twice as often, active matrix performance is achieved at passive matrix complexity. Several devices exhibited this behaviour, though they were destroyed in testing.

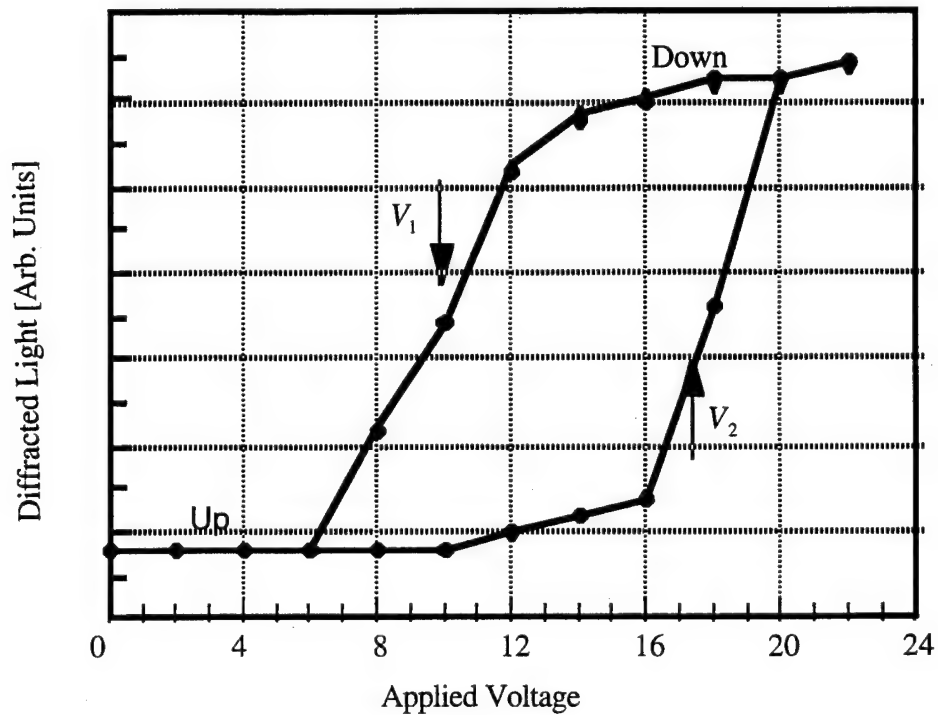


Figure 3.6: Measured hysteresis curve of a single pixel. The finite slope at the instability voltages are due to variation across the pixel of individual beams.

Contrast will be degraded from 80:1 to 40:1 because the beams are partially deflected under a $(V_1 + V_2)/2$ bias. The way to fix this is to make the spacer thicker, to shift the hysteresis curve down. In this way the thicknesses can be adjusted so that $(V_1 + V_2)/2$ produces minimal diffraction.

3.6 Speed

The resonant frequency of these devices is close to 10 MHz [Solgaard 1992]. They are faster than earlier devices because of smaller dimensions and higher residual stresses. The 10-to-90 switching speed is 20.5 ns (see Figure 3.7). This speed of switching makes the GLV the fastest light valve of which the author is aware, roughly 500 times faster than TI's valve and 500,000 times faster than LCDs on the market. This speed is useful because it allows the device to operate in a row by row fashion. This eliminates the need for a full set of data latches for the entire frame—two orders of magnitude savings in transistor count.

Rate	Events per Frame	Frequency
Frame Rate	1	60 Hz
Frame Address	2	120 Hz
5 bits gray scale	32	3.8 KHz
Line Rate (VGA) noninterlaced	480	1.8 MHz

Table 3.4: Time budget for row by row addressing. A 1.8 MHz line rate is used to address a non-interlaced VGA display with 15 bits (i.e., 5 bits per color).

3.7 Temperature Limits

If the GLV is used in a projection system, it is likely that an extremely bright and high power source will be used. About 5% of the incident light will be absorbed by the aluminum top reflector, and this light will heat the device. Since the materials used are fairly stable with respect to temperature up to 400°C, the melting point of aluminum, it is expected that the GLV will be robust with temperature. However, it is important for the driver design that the instability voltages not change too much with temperature.

Using the values in Table 3.4, the average stress in beams composed of 1325 Å of nitride and 400 Å of aluminum decreases by 0.25 MPa/°C. Therefore, at 400°C the average tensile stress in the beams decreases by only 100 MPa, which results in approximately a 25% shift in instability voltages for low residual stress devices. The change is correspondingly smaller for higher stress devices.

Another problem is the fact that the aluminum, which becomes compressed by the smaller thermal expansion coefficient of silicon, may force the beam to deflect up past the plane of the spacer. Because of the dependency of the materials parameters on deposition technique, this possibility should be explored experimentally. Since only 5% of the incident illumination is absorbed, it is extremely unlikely that any lamp could heat a GLV past 150 or 200 °C.

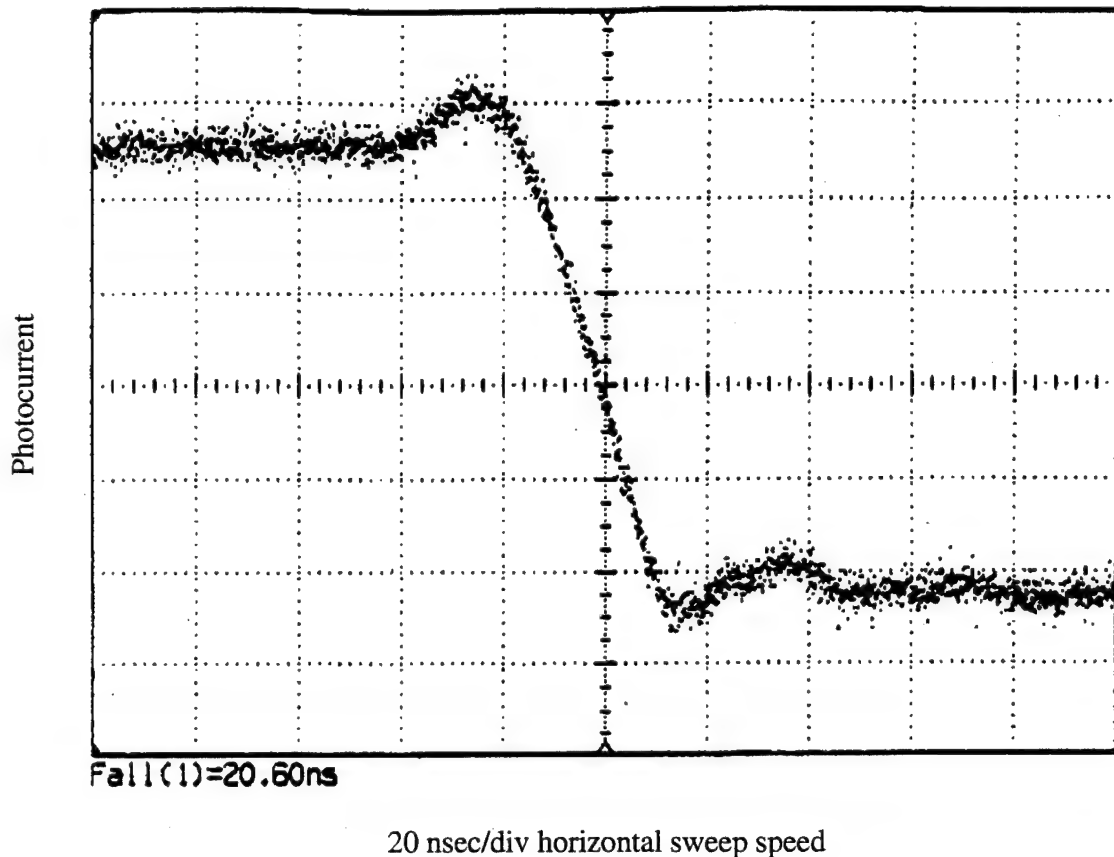


Figure 3.7: Pixel switching in 20.5 ns. The photocurrent from a single 25 x 25 μm pixel is shown as measured on a silicon photodetector on optical system I. The pixel switches from the up to the down position. The rise before the transition is thought to be an artifact of the measurement.

Material	Youngs Modulus [GPa]	Thermal Expansion [$10^{-6}/^{\circ}\text{C}$]
Al	70	25.0
Si	73	2.33
Si ₃ N ₄	200	0.8

Table 3.4: Materials parameters for thermal expansion. [Petersen 1982]

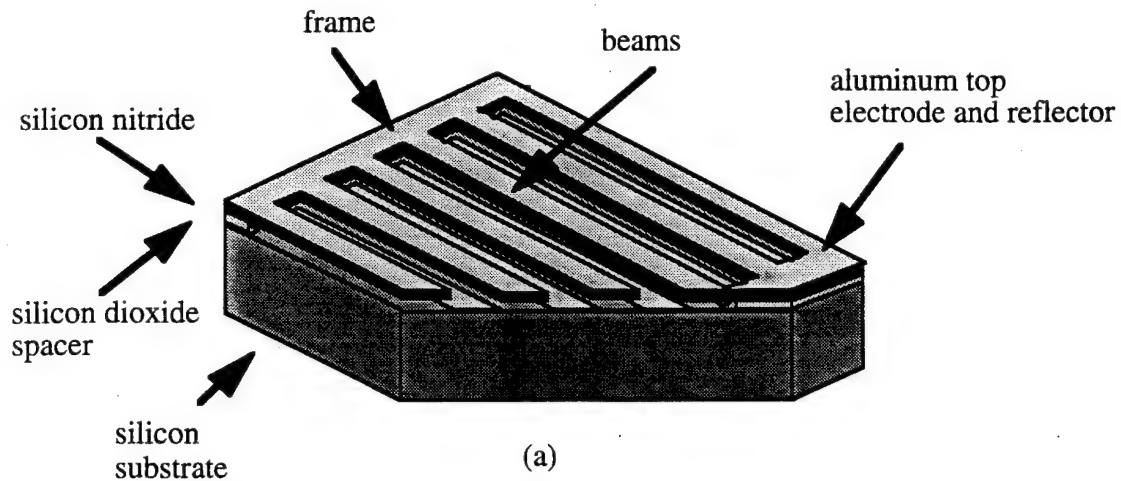
Chapter 4

Fabrication of the GLV

4.1 Basic Process

The GLV can be fabricated in its simplest form with only a single mask. The morphology of a single pixel is shown in Figure 4.1. The pixel is defined by a frame which extends along the front and back edges. Connecting the two pieces of the frame are several beams, which are the moving parts of the device. Beneath the frame is a spacer layer, which supports the frame away from the substrate. An air gap separates the beams from the substrate, which is conducting. On top of the beams, the frame, and the exposed areas of the substrate is a thin layer of metal, which enhances the reflectivity of the structure and serves as the top electrode.

Fabrication of linear arrays of these devices is diagrammed in Figure 4.2. The first step is to deposit on an prime silicon wafer a 1325 Å thick layer of silicon dioxide (hereafter abbreviated "oxide") followed by 1325 Å of silicon nitride ("nitride"). The nitride is patterned to form the frame and beams of the device. Then an isotropic, selective etch is used to undercut the oxide from beneath the beams. In order to free the beams, at least 0.75 μm of undercut is needed. However, this is not enough to completely undercut the oxide from beneath the frame. In this way the frame remains supported by the oxide, and the beams are free but supported at their ends. Since a silicon rich LPCVD nitride is used, the beams are under tension. Finally, 400 Å of aluminum are evaporated onto the top of the structure to form the top electrode and reflector. The wafers are then diced.



beams held up
by tensile stress

(b)



beam pulled down
electrostatically

(c)

Figure 4.1: Single pixel of the one mask GLV process (a). Beams in the undeflected position (b). Beams pulled against the substrate (c). Not to scale.

1: Deposition of sacrificial layer and bridge material



2: Patterning of bridges



3: Etching of sacrificial layer



4: Metallization

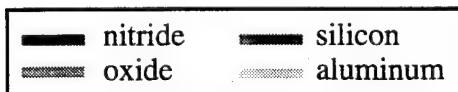


Figure 4.2: Schematic of single mask process.

4.2 Isolation

Device to device isolation is essential for device operation. Although electrical devices typically rely on reverse-biased junctions or mesas, only mesas are suited to micromechanical devices.

The problem with reverse-biased junctions arises from the fact that the 10:1 width-to-thickness ratio makes it difficult to clean contaminants from under the beams. For this reason, it is undesirable to use photoresist on the GLV after the top electrode/reflector layer has been evaporated. Without a patterning, the electrode material will short the isolation junctions. Another problem is that the large operating voltages of the GLV, up to 30 V, can cause avalanche breakdown of the isolation junctions.

In order to design a mesa isolation process that requires no masking steps after the metal deposition, overhanging features are needed. Fortunately, the nitride layer of the GLV overhangs the oxide spacer by over half a micron in all directions, providing maskless device isolation. This overhang is an artifact from the release-etch process, which has to undercut by at least one half of the width of the widest beam. In color devices this means at least $0.75\text{ }\mu\text{m}$ of nitride overhang the oxide.

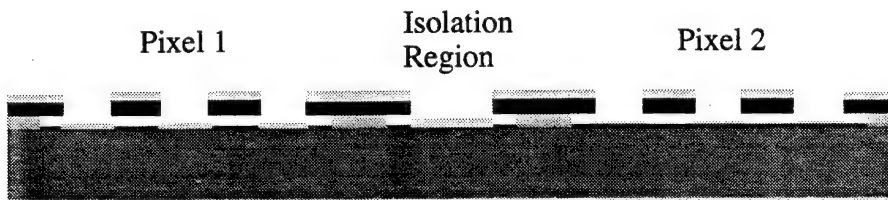
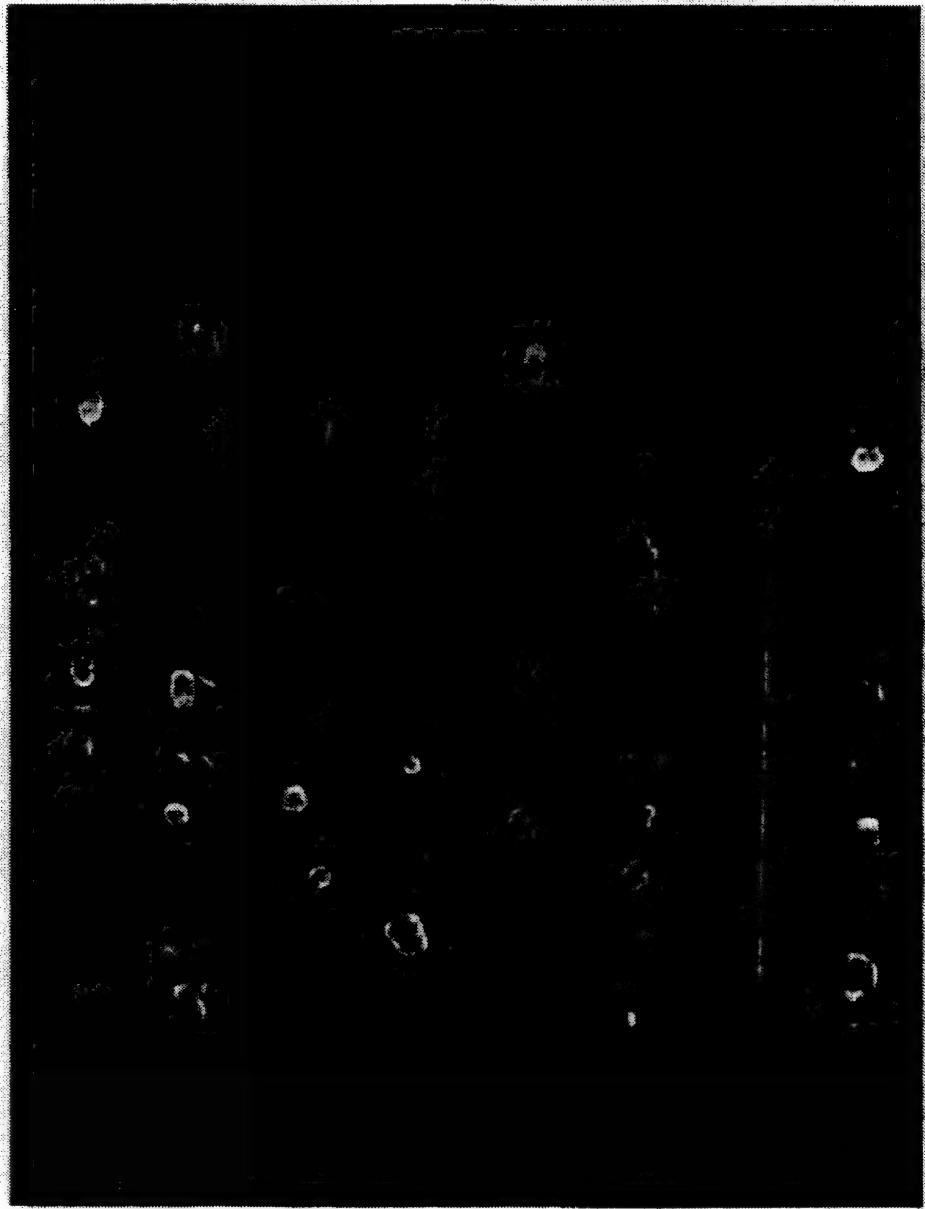
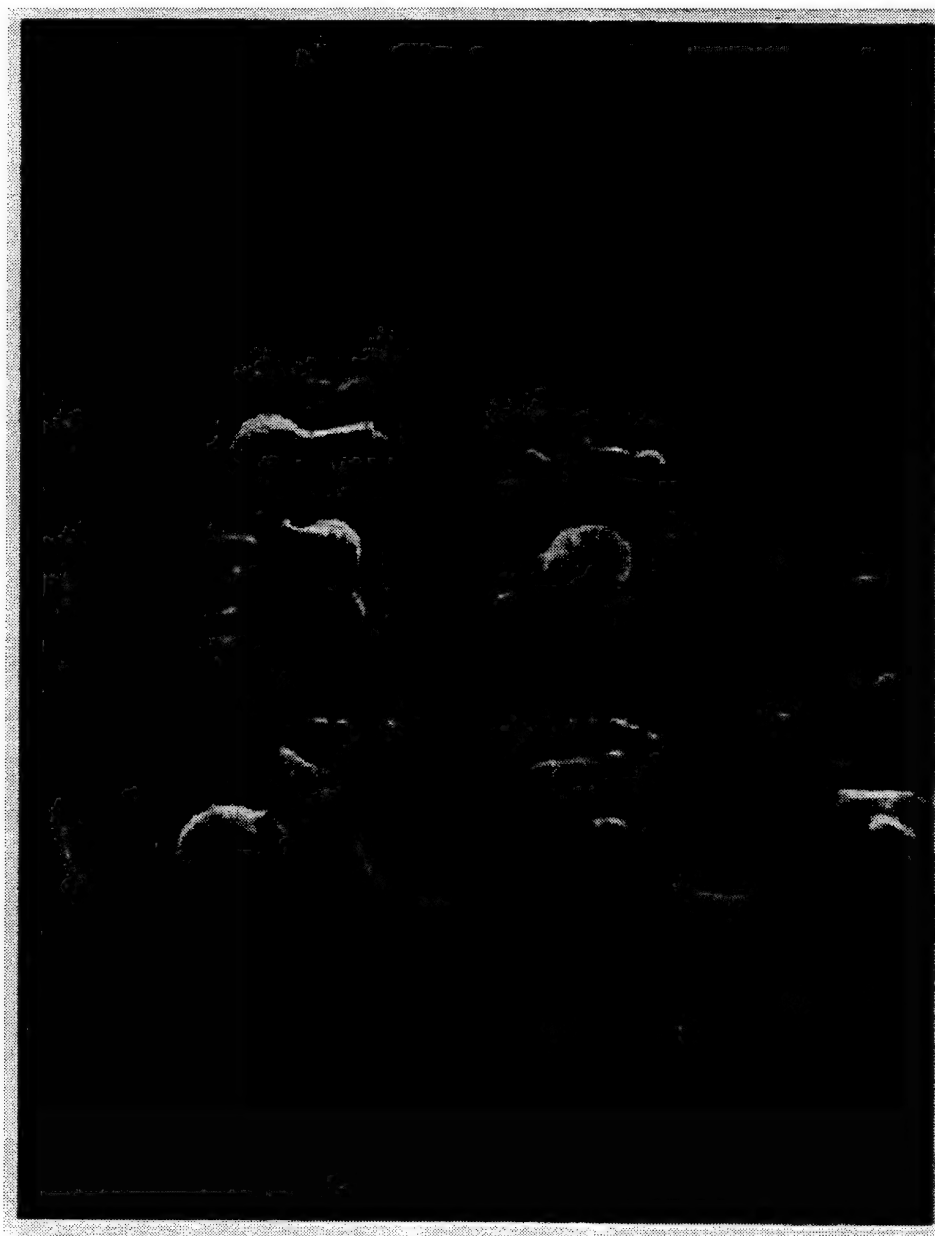


Figure 4.3: Device to device isolation.

In the case of an ideal device with a perfectly evaporated top-electrode, the thickness of the metal could approach that of the oxide spacer, over $1000\text{ }\text{\AA}$. However, if the quality of the sidewalls is poor, then it becomes apparent that thick metal can increase the likelihood of shorting when the beams are brought into contact with the substrate as in Figure 4.4. Peak fields in air and nitride can approach $200\text{ V}/\mu\text{m}$ for an ideal device. If the sidewalls are imperfect, the fields can increase several-fold, to perhaps $1\text{ KV}/\mu\text{m}$. These fields are dangerously close to the dielectric breakdown fields. For this reason thinner aluminum was used, with some loss in conductivity and reflectivity. Photographs 4.1 and 4.2 show devices that may have been destroyed by shorting (see Section 4.7).



Photograph 4.1: Grating destroyed by shorting and fusing. The failure of these beams is attributed to poorly insulating nitride and electrostatic break down. This hypothesis is supported by the fact that single beams have not been observed to fail in this way: this process either affects an entire wafer or is absent. The destruction of gratings is far less common than sticking as a failure mode. Fusing occurs at low voltages, typically less than 20 V.



Photograph 4.2: Closeup of fused beam.

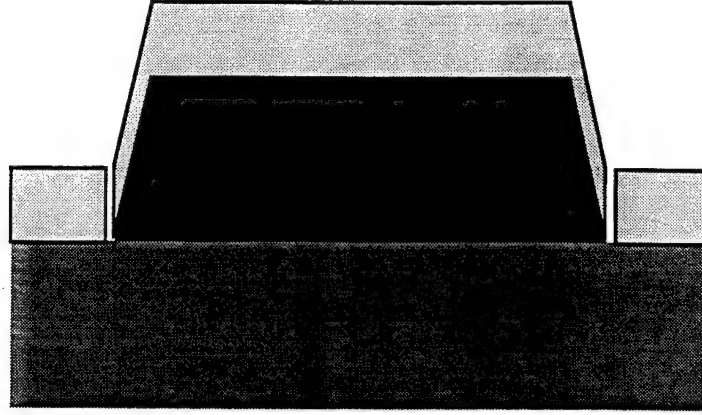


Figure 4.4: Field concentration caused by poor sidewalls.

4.3 Interconnect Conductivity and Reflectivity

To enable simple line-by-line addressing of the GLV in a megapixel display requires an RC charging time for a row (or column) of 100 ns or better. This in turn requires a sheet conductivity of 0.5Ω (per square). This is achievable with a variety of metal interconnects including aluminum, silver, and common group VIII metals. Of these, aluminum and silver are the two with good reflectivity. Silver suffers from corrosion problems compared to aluminum, so aluminum was chosen for the top electrode (and the top surface of the bottom electrode, since the deposition isn't masked or etched). The thickness of aluminum needed for 0.5Ω , which is 750\AA , is too thick given the slope in the nitride sidewalls as discussed above. Therefore, a thinner aluminum layer was used. The sheet conductivity of 400\AA of aluminum is 1Ω . The decrease in conductivity will be problem for large arrays but is not an issue for the smaller arrays tested here.

The reflectivity of a thin layer of aluminum on top of nitride is given as [Ramo 1984]:

$$R = \left\| \frac{Z - Z_0}{Z + Z_0} \right\|^2$$

where

$$Z = Z_{Al} \frac{Z_{SiN} \cos \beta L + j Z_{Al} \sin \beta L}{Z_{Al} \cos \beta L - j Z_{SiN} \sin \beta L}$$

and $Z_{SiN} = 154\Omega$, $Z_{Al} = 5.3 + 53j\Omega$ [Palik 1985], $Z_0 = 377\Omega$, and $\beta = 2\pi / \lambda$. The reflectivity R is 0.33 for $L=200\text{\AA}$ of aluminum, and 0.75 for 400\AA . The same result

holds for silicon, with $Z_{Si} = 108\Omega$ and reflectivities of .38 and .84 for 200 and 400Å, respectively. Although 400 Å is not desirable from either reflectivity or conductivity considerations, it is a fair compromise with minimizing the thickness. With improved sidewall formation, 750Å of aluminum will satisfy reflectivity and conductivity requirements for the top electrode.

Mechanically, the main effect of the aluminum is to add mass and stiffness to the cantilevers. Young's modulus of aluminum is 70 GPa, but the increase in beam stiffness is primarily due to the increase in beam thickness. For normal operation of the devices, the elastic limit of aluminum is exceeded, so Hooke's law is no longer valid. For this reason the aluminum was neglected in the modelling in Chapter 3, with a resulting underestimate of switching voltages.

Other possibilities for the bottom electrode include metal silicides and polysilicon. The bottom electrode will generally be covered with a layer of materials from the top electrode deposition: the only optical requirement of the bottom electrode is smoothness. But silicides and polysilicon suffer from unsatisfactory conductivities. The advantage, however, is that both are stable at much higher temperatures than simple metals [Murarka 1993]. In particular, polysilicon is stable at 785 °C, the temperature for LPCVD nitride deposition. In this work polysilicon is used for the bottom electrode. Ultimately a more conductive bottom electrode will be required.

4.4 Sticking

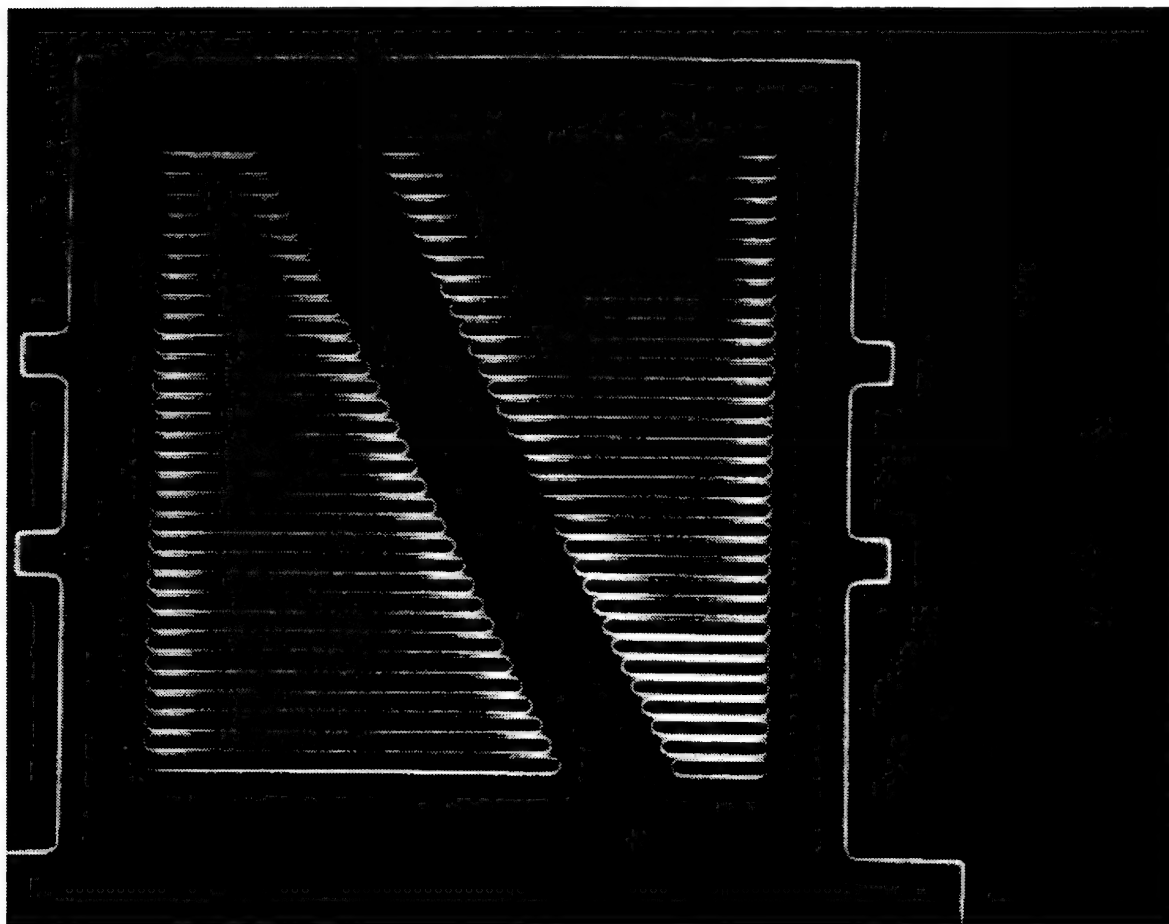
Whenever the beams of the GLV are brought into contact with the substrate (or underlying interconnect) there is a possibility of sticking. Sticking generally occurs either during the drying step after the oxide release etch or when the beams are switched down into substrate contact by a voltage exceeding V_2 . In the absence of a third electrode, which could supply an upward electrostatic attraction to raise stuck beams, sticking must be regarded as a device failure. As a failure mode, it is not catastrophic, since sticking usually is not accompanied by short- or open-circuiting (which then destroys a row or column).

The basic mechanism of sticking depends on when it occurs. During fabrication, as the water that fills the volume beneath the beams evaporates, surface tension of the fluid pulls the beams into contact with the substrate. It was postulated [Alley 1992b] that

solutes in the evaporating fluid that remain behind can covalently bond the beams to the substrate. Since beams that have been stuck in this way take several hours to become unstuck when re-immersed in water, it is assumed that the binding energy is large.

4.4.1 Water

If the beams become stuck during operation, the likely culprit is hydrogen bonding mediated by moisture between hydrogenated and hydroxylated surfaces [Scheeper 1992]. In the GLV the beams are made of nitride, which can hydroxylate, and the substrate of silicon, which can oxidize. The test of the applicability of this theory to the GLV is quite simple: much higher device yields and longer device operation are seen for light valves operated in a flowing dry nitrogen ambient. Also, device failure from sticking during operation is reduced for wafers that are stored in a dry vacuum chamber. In order to quantify these results, beam peeling theory will be reviewed in the next section.



Photograph 4.3: Harp structure.

Sensitivity to water vapour is not unique to GLVs, and when manufactured they can be baked and hermetically sealed in packages.

4.4.2 Beam Peeling Theory

An excellent theory that analyzes the dynamics of beam sticking has recently been published by Mastrangelo [Mastrangelo 1992; Mastrangelo 1993a; Mastrangelo 1993b]. The applicable formula for L_h , the minimum beam length that will be stuck, is given as a function of the average stress in the beam, σ_R , the specific binding energy, γ_s , and the ratio of surface contact area to total area under the beam, δ :

$$L_h^4 = \left(\frac{128Et^5}{5\gamma_s\delta} \right) \left(1 + \frac{4\sigma_R L_h^2}{21Et^2} \right)$$

The equation can be solved numerically; the elastic modulus term that comes from the stiffness of the beam and the residual stress term are both significant—neither beam stiffness nor beam stress dominates. Mastrangelo finds $\gamma_s = 270 \text{ mJ/m}^2$ for hydrophilic (water attracting) and $\gamma_s = 100 \text{ mJ/m}^2$ for hydrophobic (water repelling) surfaces; our data (see Figure 4.6) agrees with the hydrophilic finding. The reason hydrophilic surfaces have a higher binding energy than hydrophobic is that hydrophilic surfaces have hydroxyl groups that can hydrogen bond, while hydrophobic surfaces use the weaker Van der Waal's bond.

The basic means of testing the specific binding energy is through the use of a test structure that has a number of different length beams, from 10 to 40 μm . This “harp” structure is shown in Photograph 4.3. Generally, all the beams longer than a certain length, L_h , will be stuck, while all the shorter beams will be up. This is shown on an atomic force micrograph in Photograph 4.4. To have high yield, a GLV device should be designed with $L < L_h$. As discussed in Section 2.6, it is desirable to make L between 10 and 20 μm . This requires that L_h be at least 20 μm if not 30. Initial values were $9 \pm 2 \mu\text{m}$. The resulting value of L_h for each process variation will be given, and the results are summarized in Section 4.4.8.

4.4.3 Stress

The simplest way to decrease sticking is to increase the residual stress in the film. This can be accomplished by varying the ratio of dichlorosilane to ammonia in the nitride LPCVD reactor [Beck 1990]. Stresses from 100 MPa to 800 MPa are possible without

compromising the stability and breakdown characteristics of the film. The first step in decreasing sticking was to move from using 100 MPa films to 400 and 800 MPa. This resulted in L_h increasing from less than 10 μm to 12 or 13 μm , in agreement with Mastrangelo's equation. The tradeoff for decreased sticking is increased operating voltage.

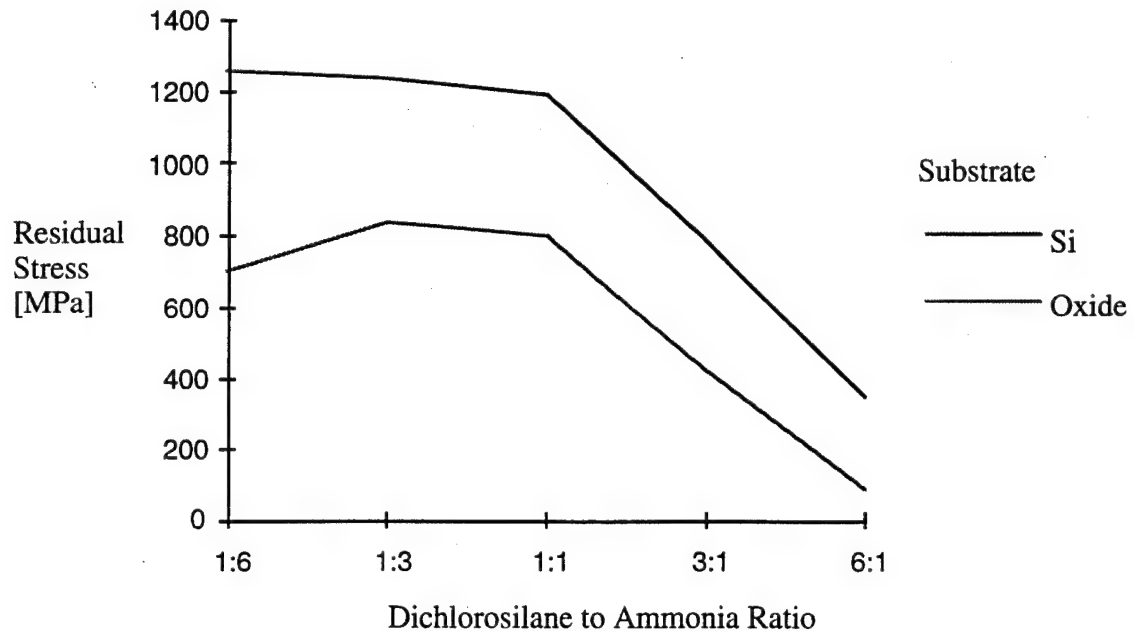


Figure 4.5: Control of residual stress in LPCVD nitride. From [Beck 1990].

4.4.4 Surface Treatments

After increasing the residual stress, the next approach to increasing L_h was to decrease γ_s , the specific binding energy. Mastrangelo reported a decrease of γ_s to 100 mJ/m² when the binding surfaces were changed from hydrophilic to hydrophobic. This is consistent with [Scheeper 1992]. Bare silicon is hydrophobic, but its oxide is hydrophilic. So while a freshly released wafer may have a hydrophobic surface, within hours that surface becomes hydrophilic.

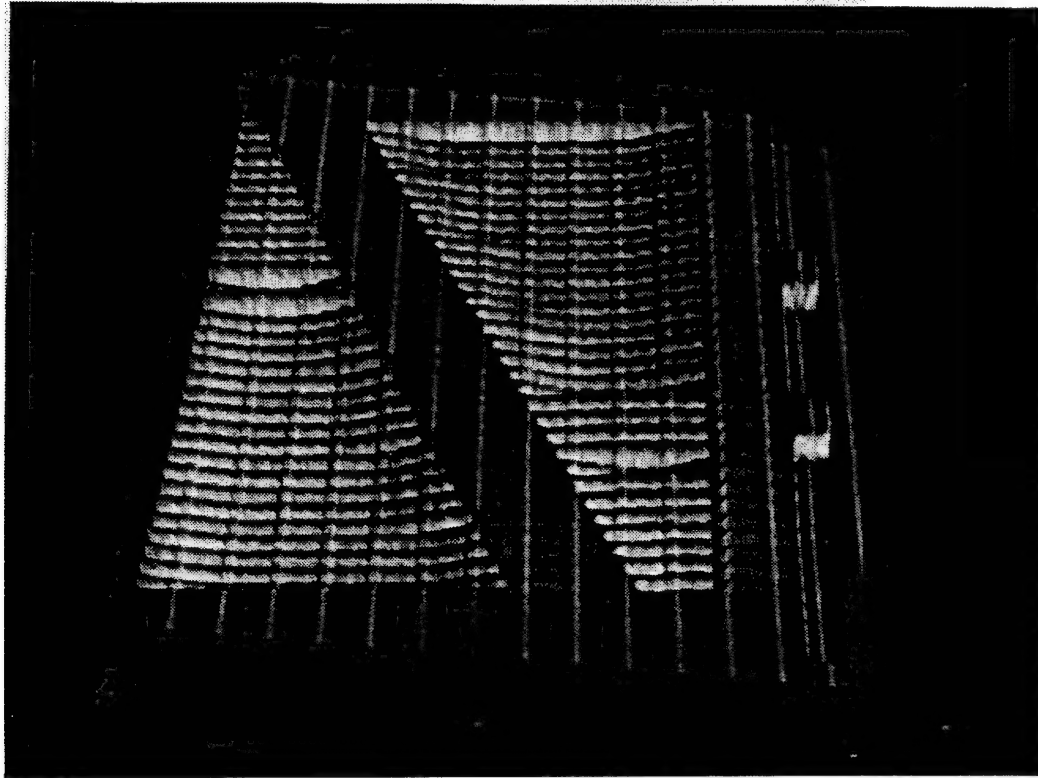
One strategy for solving this problem is to bond a hydrophobic monolayer over the oxidized surface, since preventing the formation of a surface oxide is difficult in a packaged device [Alley 1992a; Alley 1992b]. Alley's octadecyltrichlorosilane method was tried on the GLV with no success. The beam sticking became worse than before; all

beams in the harp structure stuck to the substrate. Since the chemistry of the surface treatment required anhydrous conditions, wafers were transferred from the release-etch bath to dry, organic solvents. If the large aspect ratio of the areas under the beams impeded diffusion of water from these regions, then the silating agent would bond to the water rather than the oxidized surface. This produced a hydrated polymeric material beneath the beams that ruined the devices. It is thought that this process should be able to be developed for the GLV to avoid this problem, but it promises only a two fold improvement in γ_s . Since L_h depends on the product of δ , and γ_s , another approach is to reduce the effective area of contact between the bottom of the beam and the substrate, which is discussed in the next section. Other work has been done to reduce the contact area which is not discussed here [Sandejas 1993].

4.4.5 Striations

If the substrate beneath the beams is corrugated, then δ is reduced by the ratio of the change in surface contact area. For example, if the substrate is etched to produce 100 Å tall lines, 1 μm wide, spaced every 5 μm, then the total contact area is reduced by a factor of five. The lines, hereafter referred to as "striations," are in the direction perpendicular to the beams. This assumes that when the beams are brought into contact with the substrate, they only hit the tops of the lines, not the spaces in between. In order to insure this, the switching voltage for 5 μm long beams with 100 Å gaps was calculated using the beam model and found to be larger than that needed to switch 15 μm beams with .1325 μm gaps. See Photographs 4.4 and 4.5.

This method of reducing δ has three variables, the height of the striations, the width of the striations and the line-to-line spacing. Increasing the height of the striations is desirable because it allows the line-to-line spacing to increase. The height of the striations is limited by it's effect on contrast ratio. Heights of 100 Å do not reduce contrast appreciably (see Figure 4.8 and the fact that the striation only occupies 0.2 or less of the surface). With 100 Å high striations, the line-to-line spacing can be several microns, at least 5 if not 10. The striation width is limited by lithography or processing techniques. Since we used lithographically defined striations with no etch-stop (which would uncouple the striation width and height), we were limited to 1 μm wide striations. This gives a total $\delta = 5$. This geometry increased L_h from 13 to 22 μm, which again agrees with Mastrangelo's equation.



Photograph 4.4: Atomic force microscope image of harp structure. Striations are clearly evident on both substrate and nitride. In this case the reflow smoothing process failed to provide a flat surface for nitride deposition.

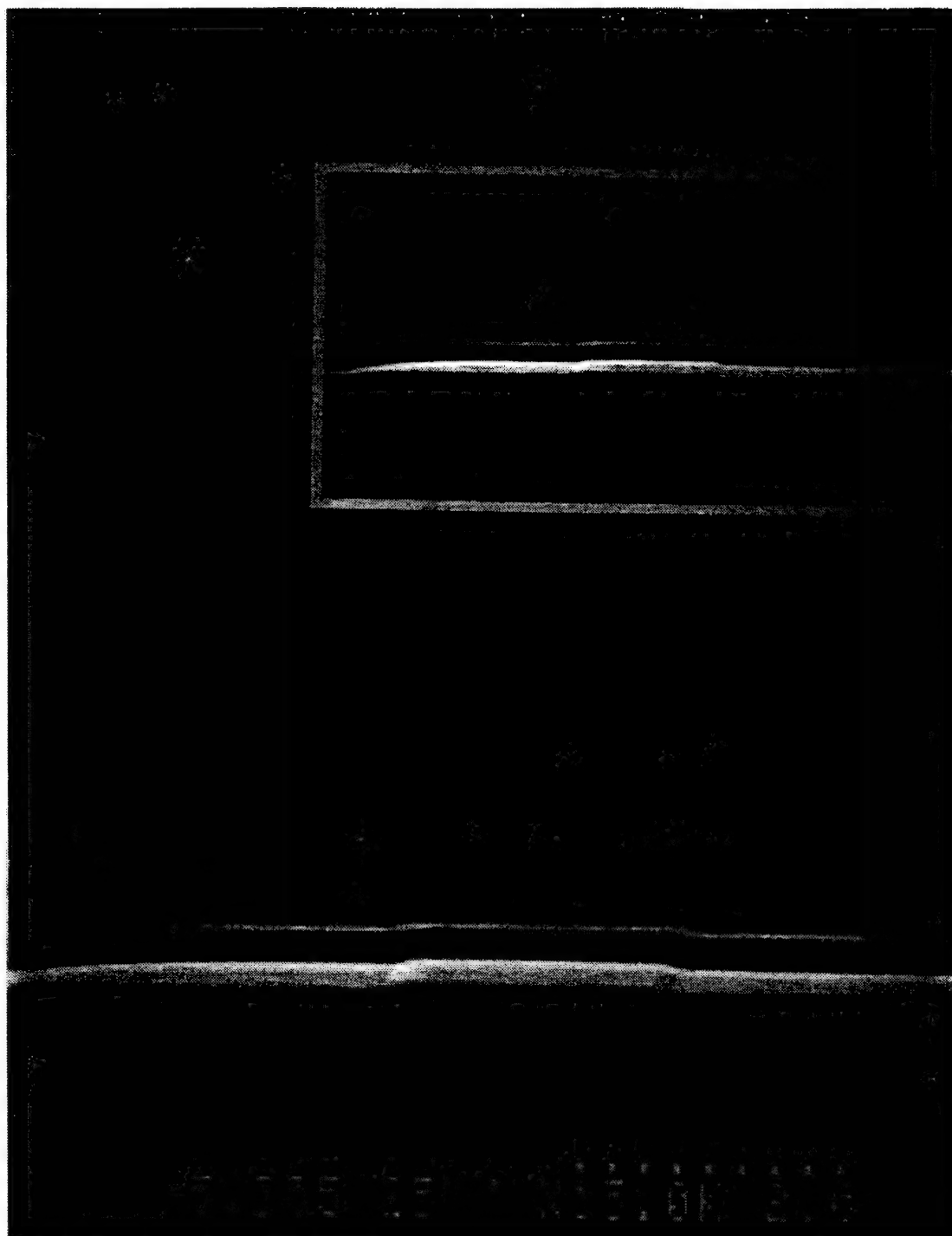
4.4.6 Van der Waals Bonding

Although water undoubtedly plays an important role in the sticking forces, in a dry ambient sticking still remains a problem. In this case the culprit is not a surface chemistry problem but a fundamental limitation, the Van der Waal's attraction between two insulators [Scheeper 1992]. The pressure of the attraction is given by

$$P = \frac{A}{6\pi D^3}$$

where A is the Hamaker constant and D is the separation between the two materials. For $D > 30$ nm the long-range attraction is given by

$$P = \frac{B}{D^4}$$



Photograph 4.5: Striations in one dimensional arrays. Note the slight striation in the nitride beams and the 1 μm undercut of the frame.

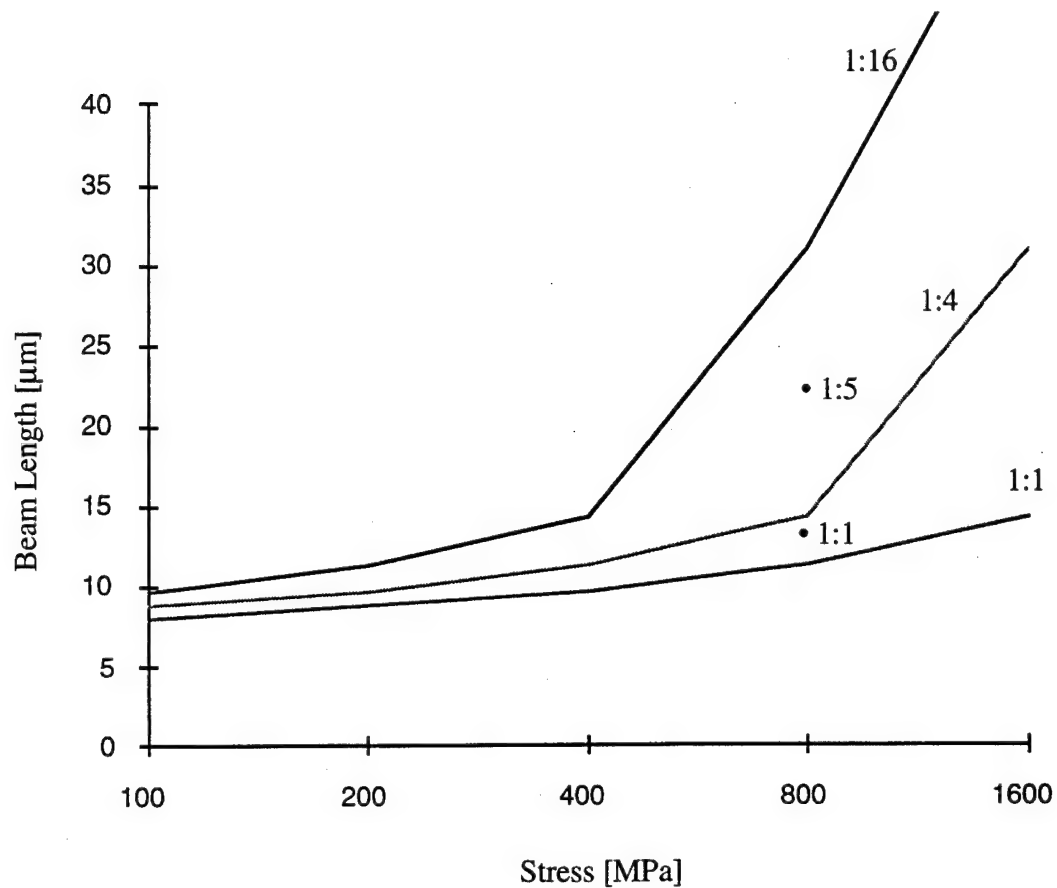


Figure 4.6: Beam peel length as a function of residual stress and striations. The three curves are for $\delta = 1:1$ (i.e., no striations), 1:4, and 1:16. The two data points are experimental for $\delta = 1:1$ and 1:5 with 800 MPa residual stress.

The expressions for Van der Waals bonding and the string model of chapter 3 can be combined to plot L_h as a function of the striation ratio, δ , and residual stress, σ . See Figure 4.6. The results show an encouraging trend. For lithographically defined striations, with a maximum δ of 1:10, there are modest gains possible. But through the use of an etch stop layer, which would allow timed etching to narrow the striations, $\delta = 1:100$ is possible. This should exhibit an extremely long L_h . Although this approach is appealing, using surface roughness is simpler.

When D is approximately 2 nm, which may not be a bad guess for the surface roughness on the bottom side of the nitride beams, then this expression gives a good estimate for the observed value of γ_s for a substrate exposed to moisture. This suggests that increasing

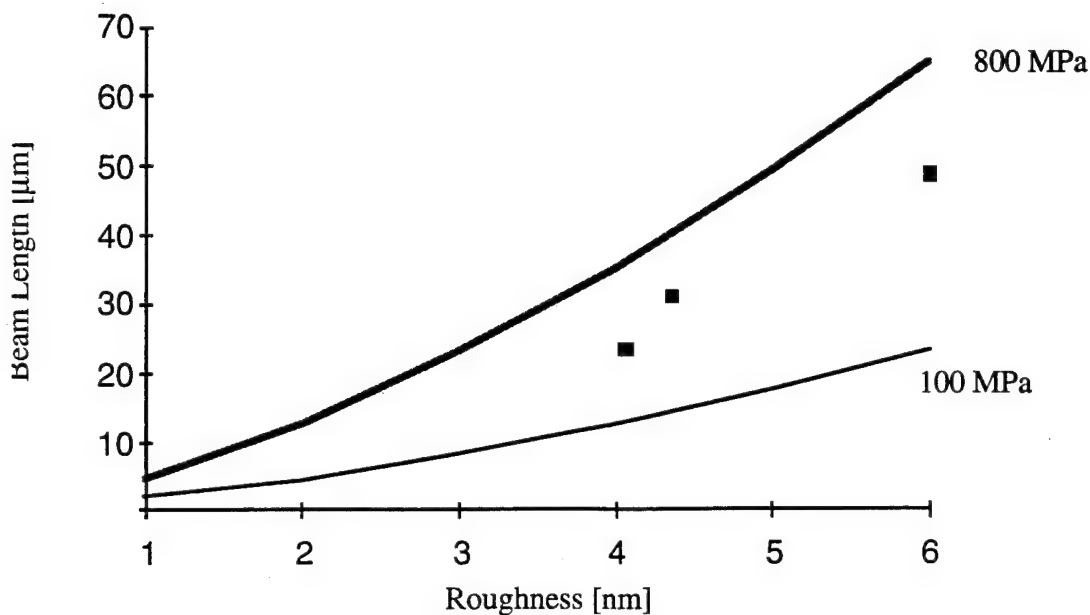


Figure 4.7: Surface roughness and beam sticking. The three dots show data for 800 MPa and RMS surface roughness measured by AFM.

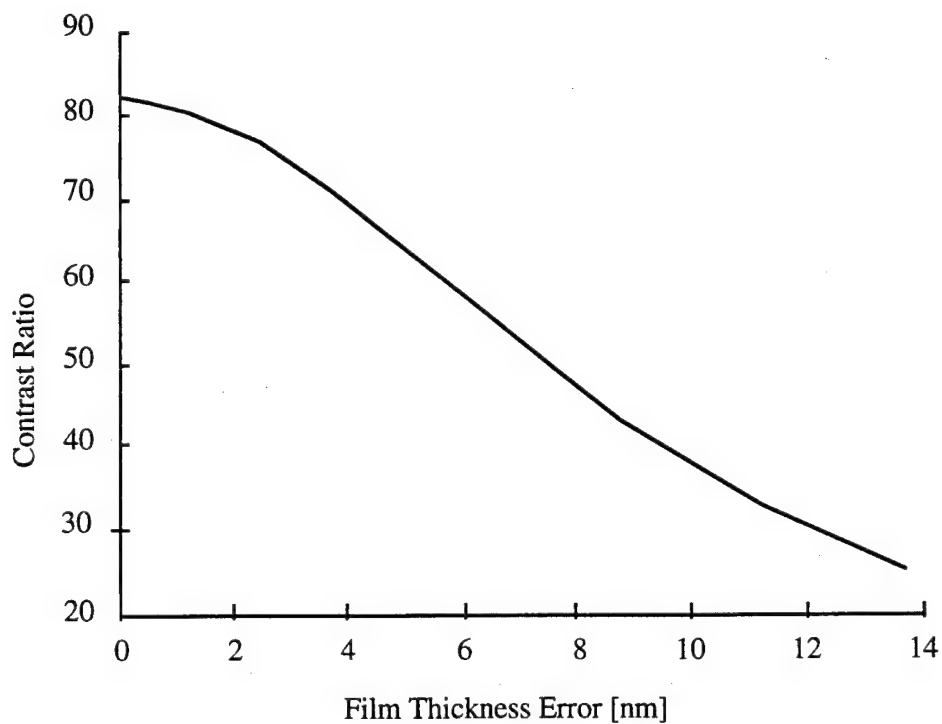
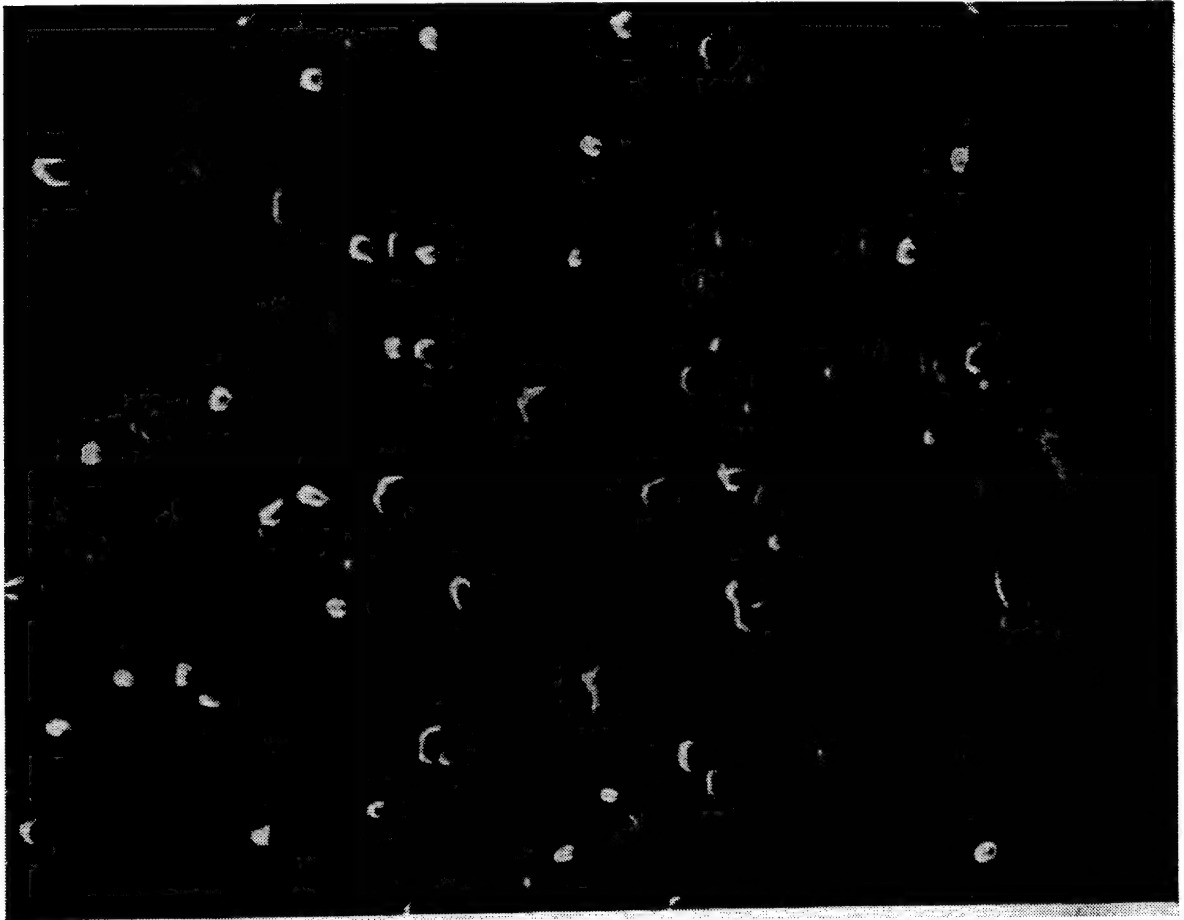


Figure 4.8: Contrast ratio versus film thickness. Although thickness error and roughness are not the same, this figure, repeated from Chapter 2, shows that only a few nanometers of roughness are acceptable before the contrast ratio decreases precipitously.

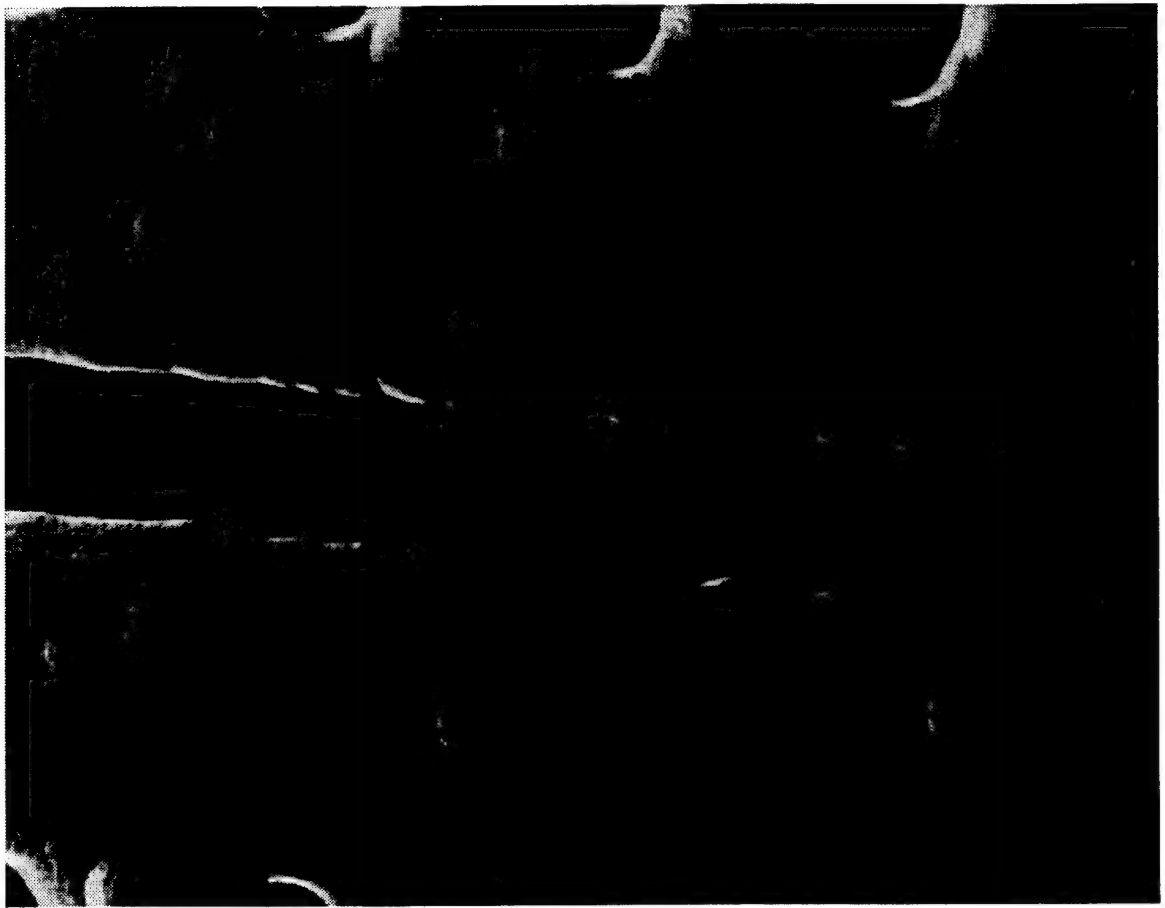


Photograph 4.6a: Rough polysilicon surface.

the roughness of the substrate or the bottom side of the beams will be useful in controlling stiction.

4.4.7 Surface Roughness and Contrast

One semiconductor material that has controllable roughness is LPCVD silicon, which may be amorphous or polycrystalline [Bawolek 1993; Dana 1993; Voutsas 1993]. By controlling growth temperature, film thickness, and substrate surface quality a very large range of surface roughness is possible [Ibok, 1993 #64]. If we make the identity that D , the distance between the beam and the substrate in the down position, is equal to the surface roughness, then using the string model and the Van Der Waals force gives Figure 4.7, in which L_h is plotted as a function of residual stress and surface roughness. Three data points are added for 800 MPa devices with various polysilicon roughnesses (measured by atomic force microscopy). Photographs 4.6a and 4.6b show the rough polysilicon surface and the nitride that is grown over it.



Photograph 4.6b: Nitride deformed by rough polysilicon. The reflow process smooths the oxide surface, but some roughness remains.

It is clear from Figure 4.7 that increased roughness, although not as effective as striations at increasing L_h , is still very effective. The tradeoff is with contrast ratio. Although we do not have a theory for contrast that includes sub-wavelength scale roughness, Figure 4.8 gives some idea of the decrease in contrast ratio in this circumstance.

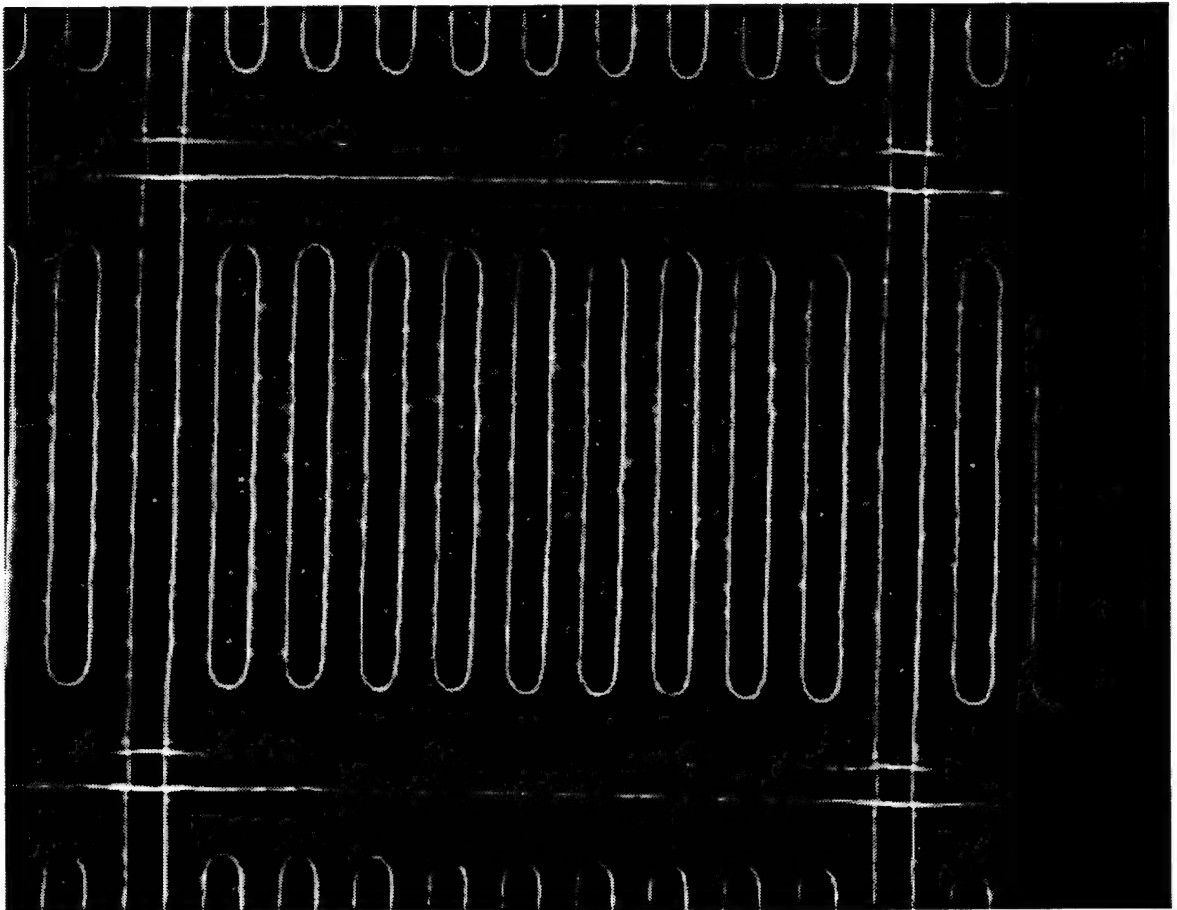
4.4.8 Progress in Reducing Sticking

The progress in solving the sticking problem is summarized in Table 4.1, in which L_h is given for each process variant. Short beams have very high switching voltages. An observed practical limit was that above 40V electromigration of the aluminum resulted in the devices shorting to ground. If the test circuit had significant source impedance, then the beams simply do not move (although they are up). If a low-impedance source is used,

the device explodes, scattering debris from the beams, frame, and bondpads. In order to keep operating voltages to 35 V or less, the minimum usable beam length is 15 μm . To insure >99% yield of usable devices, an L_h of 25 μm is desired:

Process	L_h [μm]
Desired	>25
Initial (low stress)	10
High stress	13
Surface treated	8
Striated	22
p-Si roughened	>40

Table 4.1: Progress in decreasing sticking.



Photograph 4.7: Single pixel in a two-dimensional array. Roughness in the nitride results in less than optimal lithography.

4.5 Two-Dimensional Arrays

The problems with building two-dimensional arrays of pixels are important because solving them is the first step in integrating the processes of light valve construction and driver circuit integration and fabrication. Regardless of whether an active or passive matrix is used, the interconnection of the drivers and the pixels will require an interconnect step, and the development of two-dimensional arrays exhibits significant difficulties.

The primary difficulties with adding an interconnect layer are twofold: the interconnects must remain isolated from one another, the substrate, and the top electrodes; and the interconnect layer must be thermally compatible with subsequent processing. The first of these problems we have solved, the second is a source of continuing concern.

4.5.1 Isolation

The interconnect layer presents special problems because of the fact that the present process does not have a masking step after the top electrode deposition. Because of the large aspect ratio of the beams and the small thickness of the spacer, it is difficult to remove photoresist residue from beneath the released beams following lithography. Therefore, the basic process includes no wet processing after the release etch. Since the top electrode deposition follows the release, there is no patterning of the top electrode metal. In the basic process, isolation between top electrodes depends on the overhang of the nitride over the spacer to prevent shorting. The same mesa isolation strategy is used to isolate the bottom electrodes. The use of mesa isolation requires the use of a very non-planar structure, with the concomitant problems. (See Photographs 4.8 and 4.9).

4.5.2 Thermal budget

The reasons given for choosing aluminum for the top electrode are equally valid for the bottom electrode. The difficulty is that subsequent layers, especially the LPCVD nitride deposition at 785 °C, exceed the thermal budget of the aluminum (<400 °C). For this reason polysilicon interconnects are used instead of aluminum. Although the conductivity of polysilicon will make arrays larger than 200x200 be RC limited rather than device limited, polysilicon has the advantages that its roughness can be controlled by processing and it is stable at the nitride deposition temperature (provided it is capped with oxide).

4.5.3 Basic Recipe

Processing begins with a 5000 Å oxide isolation layer being grown on a bare silicon substrate. This isolation layer can be grown by any available technique. On top of this layer is grown a 3000-6000 Å undoped polysilicon layer. The temperature of this growth may be varied to control surface roughness. The layer is probably amorphous initially, but it crystallizes during subsequent high temperature processing (the reflow step). The polysilicon is pre-dep diffusion doped with phosphorous, cleaned, and patterned into the bottom interconnect layer. 1325 Å of low temperature LPCVD oxide are deposited on top of the nonplanar bottom electrode traces. This oxide is doped with 8% Phosphorous to reduce the reflow temperature. The oxide is steam reflowed at 1000 °C for 20 minutes. 1325 Å of LPCVD nitride are deposited next, then patterned and dry etched. The wafer is then cleaned to remove all traces of photoresist and released. The oxide spacer is removed from under the beams. In addition, oxide is removed from under the edges of the frames and the bottom electrode traces. The overhanging polysilicon and nitride provide the isolation. This process is depicted in Figure 4.9, and complete details are given in Appendix 1.

4.5.4 Nonplanar Processing

The difficulties in the development of this process are best shown in Photographs 4.9 and 4.10, which are two views of the corner regions of the 4x4 array in Photograph 4.8. Photograph 4.9 is in the same orientation as Photograph 4.8, with the top electrode making connections vertically and the polysilicon lines underneath running horizontally. Photograph 4.10 is from the the other orientation. The nonplanar structure used to isolate the bottom electrodes creates the possibility of nitride stringers shorting between adjacent top electrodes. These stringers are evident at the bright horizontal line in Photograph 4.9 and on the right side of Photograph 4.10. Second, step coverage along the edges of the polysilicon makes it possible for the top electrode to be open-circuited if the reflow is not sufficient. This can be seen in the top part of Photographs 4.10, where the nitride/top electrode runs horizontally over the polysilicon, down to the isolation oxide between the polysilicon lines, and then back up the next polysilicon line. Careful tuning of the reflow process was used to solve both problems by smoothing out the edges of the nonplanar structures.

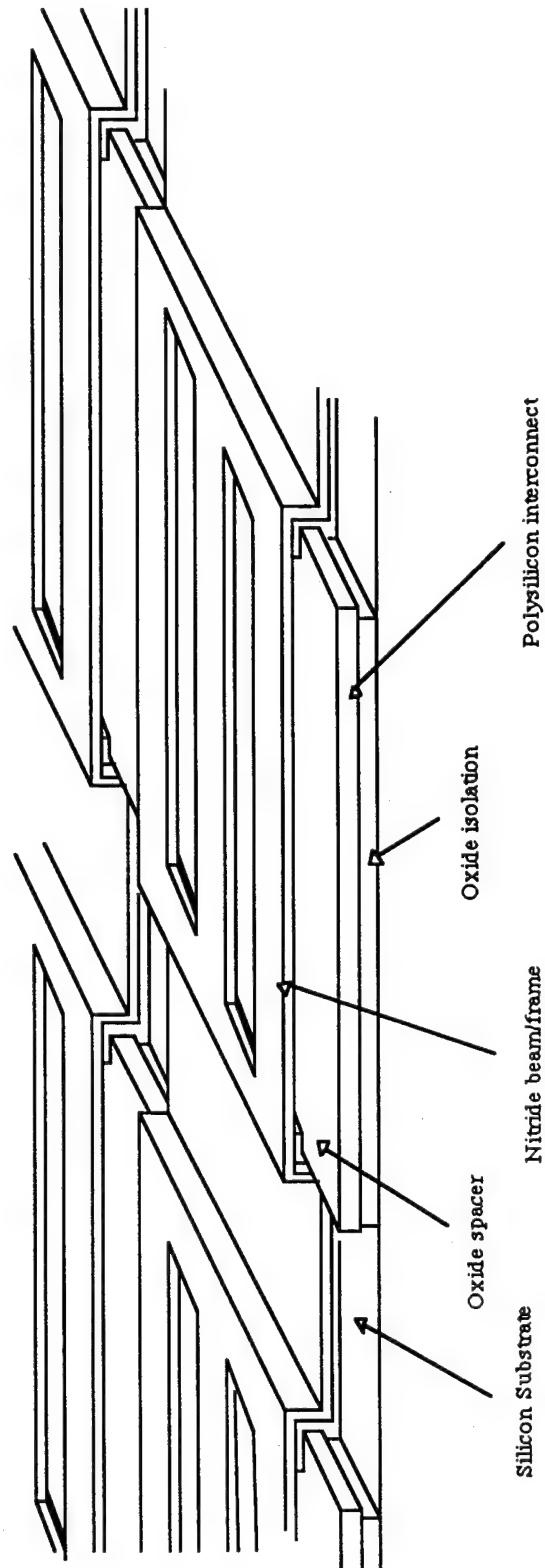
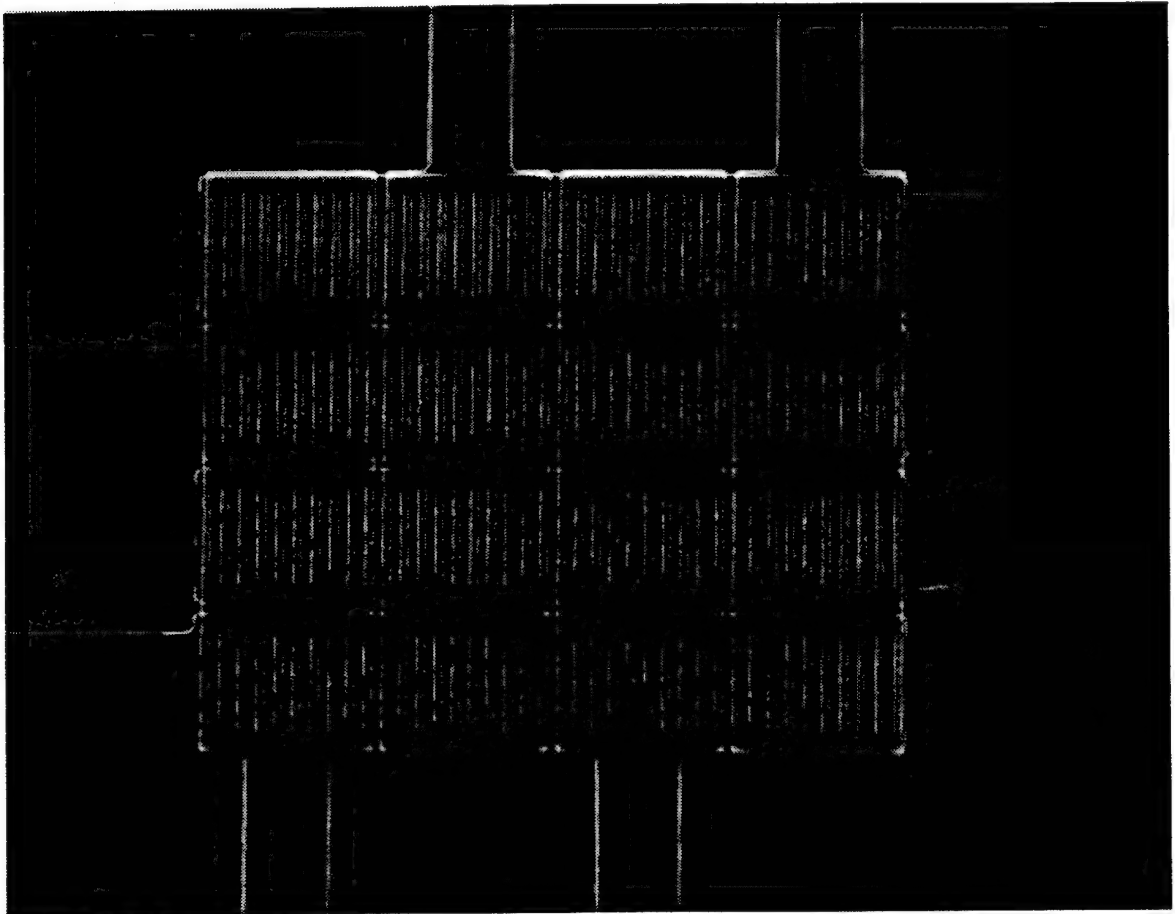


Figure 4.9: Schematic of two dimensional array. This figure shows pixels with only three beams rather than the usual ten for clarity.

4.6 Reliability

Adequate data for reliability does not exist for the GLV. An initial experiment was done that cycled pixels over 300 billion cycles at an accelerated rate (1 MHz for 100 hours), which corresponds to ten years of television use for a color GLV with eight bits of gray scale. The devices were operated with a 25 V square wave in ambient conditions. No pixel damage (in the form of sticking or fusing) was observed. However, recent work [Pryputniewicz 1994] suggests that accelerated lifetime testing is not valid, since it doesn't give the material time to deform plastically or for cracks to grow. A second limitation is that this testing was done on striated devices. It is not known whether the use of surface roughness rather than striations will increase beam cracking or not.



Photograph 4.8: 4x4 pixel array.

4.7 Device Failure

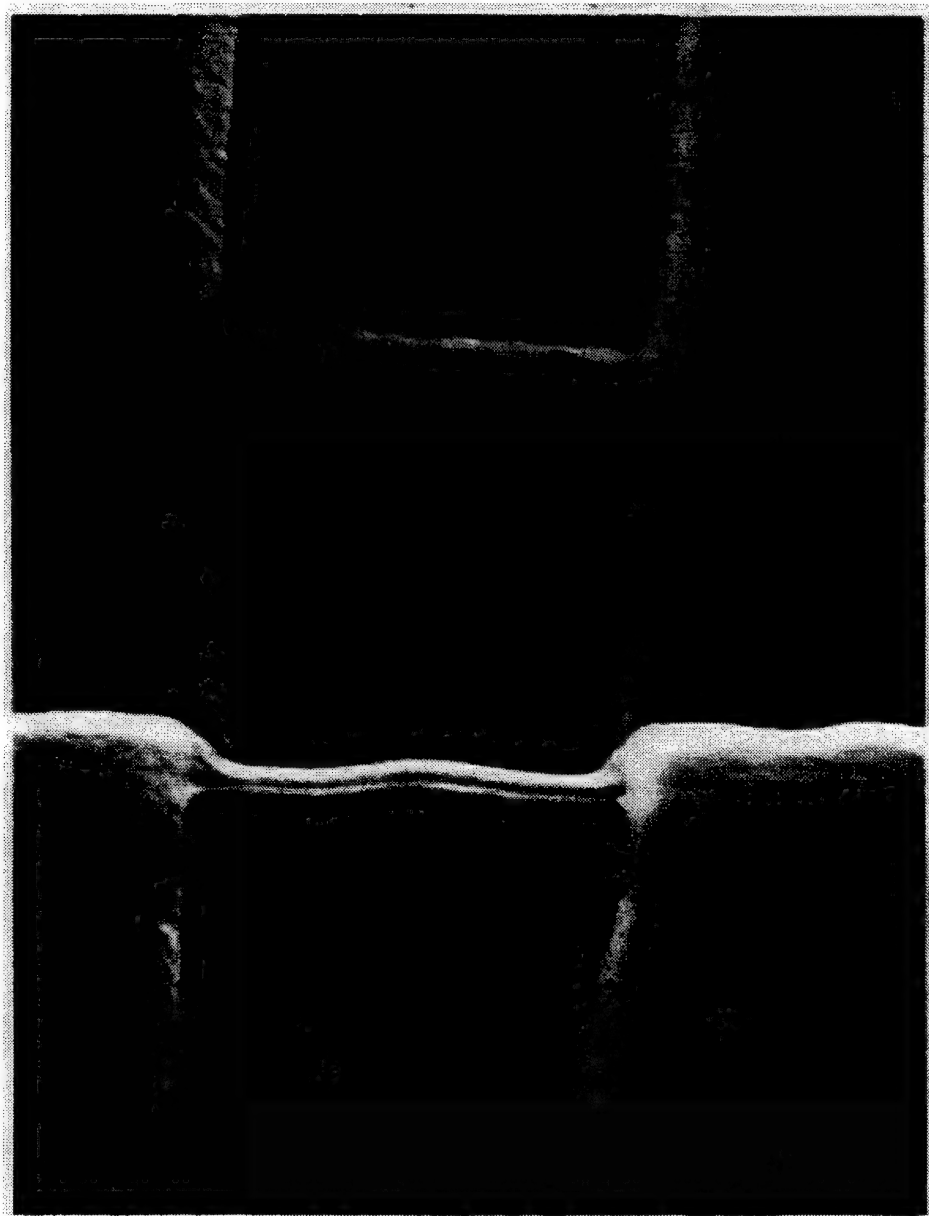
Three types of device failure have been observed. Low voltage fusing is a process that is related to a failure in wafer processing. It first appeared to be correlated to particular LPCVD nitride depositions, although measurement of thickness and refractive index did not reveal anything unusual. A later hypothesis was that the use of thicker ($1\text{ }\mu\text{m}$) aluminum bondpad metalizations caused leaching of silicon from the nitride into the aluminum. This process degrades the nitride and is known as the Kirkendall Effect [Wolf 1990]. The solution to this problem is to use an aluminum sputter target with 4% silicon. Subsequent wafers have confirmed this phenomenologically, although no measurements have been performed to establish causality. Wafers coated with aluminum/silicon did not exhibit fusing.

The second type of device failure is high voltage shorting. When $> 40\text{ V}$ is applied to devices arcing causes large currents to flow and device heating. Usually the device is destroyed catastrophically. It is thought that the large field concentrations described in Section 4.2 are responsible.

Sticking of the beams to the substrate is the third and most common form of device failure. In initial experiments, the beams stuck to the substrate during the drying process following the release-etch. Previous work established that freeze-drying the devices resulted in un-stuck devices [Solgaard 1992]. However, when operated into contact with the substrate these devices would stick. After the development of the high stress nitride process, the freeze-drying technique was abandoned in favor of standard spin-drying. For all subsequent work, if a certain beam did not stick during spin-drying, it generally would not stick during subsequent operation. For this reason the figure of merit for yield, L_h , was recorded for devices that had been recently released. Some degradation of L_h over time was observed in devices that had been left in air for months, so later devices were stored in vacuum and tested in dry nitrogen. The standard deviation for L_h on a wafer was between 2 and 3 μm , so making L_h 10 μm larger than the design length resulted in yields of greater than 90%.

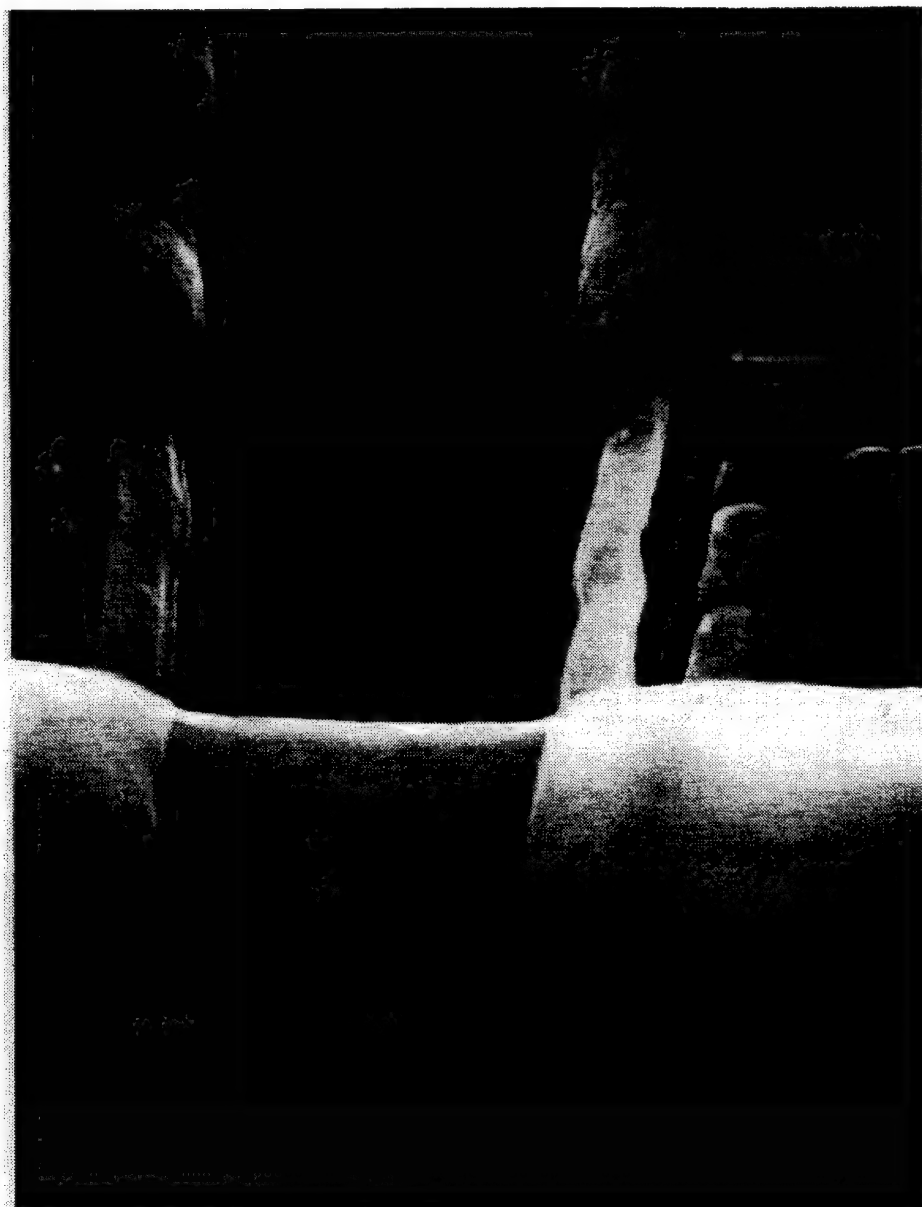
4.8 Future Process Design

The present work lessened the sticking problem and the interconnect problem though the use of the surface roughness and doping of polysilicon. It is very likely that stress concentration when the beams strike a roughened substrate will increase damage rates.



Photograph 4.9: Four corners of a two dimensional array. The nitride runs vertically, and the middle shows the isolation region. A nitride stringer is apparent in the bottom half of the picture.

Also, it is possible to redesign the striations so that they are not visible from the top surface. This modification would prevent the contrast ratio from being degraded. Thus, it is likely that future processes will make use of smooth materials and etched striations.



Photograph 4.10: Four corners point of two-dimensional array, alternate view. Nitride/top electrodes run horizontally and must be continuous over the step formed by the polysilicon lines, which run vertically. In the right half of the picture the nitride, spacer, and polysilicon can be clearly seen. A nitride stringer shorts two adjacent top electrodes together.

Another weakness of the present process is the very high thermal budget, which is 785 °C for the nitride and 1000 °C for the reflow. While clever etching might eliminate the need for reflow, the nitride is a serious problem. One alternative is to use a lower temperature nitride, say PECVD. PECVD nitride is deposited at 200 °C and through the use of a two-frequency system has controllable residual stress. Since such systems can also deposit oxide, PECVD appears to solve the thermal budget problem. Aluminum could be used for the bottom electrode as well as the top. The problem is that the release etch should have a good differential rate between oxide and nitride. For LPCVD it is well over 100:1, which is necessary for etching 10:1 aspect ratios. For PECVD, the best differential etch rate we found was 10:1. If another etch could be found, then the PECVD option becomes an excellent solution.

Chapter 5

Conclusion

5.1 Device Summary

The grating light valve is a relatively new display technology. It is based on reflection phase gratings of electrically controllable depth. When the beams are suspended "up" from the substrate the device has a minimum of diffraction, and normally incident light is reflected. If a potential is applied to bring the beams into contact with the substrate, then the device diffracts 80% of the light into the first order diffraction modes, which are then collected by a Schlieren optical system. The contrast ratio was measured to be 20:1 for black-and-white displays. A contrast of 80:1 should be achievable with improved processing techniques. A color gamut a little smaller than that of television phosphors was measured. Improved lamp collimation should improve the saturation of the colors. Contrast ratios for optimized color devices should exceed 200. Pixels as small as $6 \times 20 \mu\text{m}$ are possible.

The position of the beams is bistable for intermediate voltages. For a qualitative understanding, the beams can be modelled as strings under tension. To get better quantitative results, a full integration of the fourth order beam equation was used. The validity of the model was limited because the contribution of top electrode aluminum to the beam stiffness was neglected. Switching voltages between 5 and 10 V should be obtainable. The lowest measured in this work is 11 V. The combination of bistability and speed—the devices switch in 20.5 ns—might be used for passive matrix addressing in a row-by-row fashion. The device operation should not be significantly affected by temperatures in excess of 200 °C.

Simple fabrication requires only a single mask. To make devices with two-dimensional arrays of contacts two masks are needed. Through the use of the overhang of the frame

material the devices are isolated from each other without an additional masking step. Aluminum is used for the top layer of interconnects and the reflective layer on the beams and spaces. Sticking of the beams to the substrate is caused by hydration of the surface and/or Van der Waals bonding. The two methods of reducing this problem, corrugating the substrate with striations and using a naturally rough substrate material like polysilicon, both are extremely successful at reducing sticking. However, both have deleterious effects on the optical performance of the device if overdone. Two-dimensional arrays were constructed with a highly non-planar process. Despite problems with shorts and opens in the top conductor, this method was used to demonstrate working two-dimensional arrays.

5.2 Future Work

There are four major areas of development needed for these devices, presented in order of increasing importance.

In order to use the bistability of the devices for switching, it is necessary to insure that the hysteresis loop is made as open as possible. This might be achieved by using conducting beams or beams with higher permittivities. Conducting beams would have the effect of decreasing the gap between the top and bottom electrodes when the beams are down. This increase in capacitance would cause a substantial decrease in the first instability voltage.

A second area of research is to determine the effect of surface roughness on contrast ratio. This will help determine whether roughness or striations should be used to reduce sticking. A new process for striations should be designed that is self-aligned and produces quarter micron striations. This might have a minimal effect on contrast while decreasing sticking. Ultimately, a self-aligned striation that would not affect contrast would be ideal.

Third, the devices of this thesis were all produced with LPCVD. This process requires too high temperatures to be compatible with driver circuit fabrication. Either a move to PECVD or to alternate materials must be considered. Possibilities for alternate materials include spin-on glasses, polymers, metals, and other types of oxynitrides. This process redesign is absolutely necessary for reliable operation, since the high temperatures of the current process make it necessary to bond the drivers to the display rather than integrate them monolithically.

Finally, the aging characteristics of micromechanical displays are not at present well understood. Texas Instruments' deformable mirror device uses metal flexures, while the

grating light valve uses silicon nitride. The latter is expected to have much better ageing characteristics than the metal flexures. Although this problem is speculative, it may prove to be a critical deciding factor. In addition, it is not clear what sort of packaging is necessary to insure long life of these devices, i.e. whether full hermeticity is needed.

These four areas of research highlight the limitations of this work and the present state of the grating light valve. With additional work in these areas it is possible that the grating light valve will someday be commercially produced.

Bibliography

- [Alley 1992a] R. Alley, "Recipe for OTS Silating," Personal Communication, Nov. 11, 1992 .
- [Alley 1992b] R. L. Alley, G. J. Cuan, R. T. Howe, and K. Komvopoulos, "The Effect of Release-Etch Processing on Surface Microstructure Stiction." In *IEEE Solid-State Sensor and Actuator Workshop*, Hilton Head, SC, IEEE, pp. 202-207, 1992b.
- [Alt 1973] P. M. Alt and P. Pleshko, "Scanning Limitations of Liquid-Crystal Displays," *IEEE Transactions on Electron Devices*, vol. ED-21, no. 2, pp. 146-155, 1973.
- [Apte 1993] R. B. Apte, F. S. A. Sandejas, W. C. Banyai, and D. M. Bloom, "Deformable Grating Light Valves for High Resolution Displays." In *Society for Information Display Symposium*, Seattle, WA, 1993.
- [Aratani 1993] K. Aratani, P. J. French, P. M. Sarro, R. F. Wolffenbuttel, and S. Middelhoek, "Process and Design Considerations for Surface Micromachined Beams for a Tuneable Interferometer Array in Silicon." In *Solid-State Sensors and Actuators: TRANSDUCERS '93*, Yokohama, pp. 230-235, 1993.
- [Backlund 1992] Y. Backlund, K. Hermansson, and L. Smith, "Bond-Strength Measurements Related to Silicon Surface Hydrophilicity," *Journal*

of the Electrochemical Society, vol. 139, no. 8, pp. 2299-2301, 1992.

- [Bawolek 1993] E. J. Bawolek, J. B. Bohr, E. D. Hirleman, and A. Majumdar, "Light scatter from polysilicon and aluminum surfaces and comparison with surface-roughness statistics by atomic force microscopy," *Applied Optics*, vol. 32, no. 19, pp. 3377-3400, 1993.
- [Beck 1990] P. A. Beck, S. M. Taylor, J. P. McVittie, and S. T. Ahn, "Low Stress Silicon Nitride and Polysilicon Films for Micromachining Applications." In *Proceedings of the Materials Research Symposium*, vol. 182, pp. 207-212, 1990.
- [Bloom 1992] D. M. Bloom, F. S. A. Sandejas, and O. Solgaard, "Method and Apparatus for Modulating a Light Beam," *United States Patent*, Number Serial Number 07/876,078. Issued: Filed April 28, 1992.
- [Born 1980] M. Born and E. Wolf, *Principles of Optics*. Sixth Edition (Corrected) ed., Pergamon Press, 1980.
- [Bowling 1985] R. A. Bowling, "An Analysis of Particle Adhesion on Semiconductor Surfaces," *Journal of the Electrochemical Society: Solid State Science and Technology*, vol. no. September 1985, pp. 2208-2214, 1985.
- [Boysel 1989] R. M. Boyzel, J. M. Florence, and W.-R. Wu, "Deformable Mirror Light Modulators for Image Processing." In *Optical Information Processing Systems and Architectures*, vol. SPIE 1151, pp. 183-194, 1989.
- [Burns 1990] D. W. Burns and H. Guckel, "Thin Films for Micromechanical Sensors," *Journal of Vacuum Science and Technology A*, vol. 8, no. 4, pp. 3606-3613, 1990.

- [Cho 1992] S. T. Cho, K. Najafi, and K. D. Wise, "Internal Stress Compensation and Scaling in Ultrasensitive Silicon Pressure Sensors," *IEEE Transactions on Electron Devices*, vol. 39, no. 4, pp. 836-842, 1992.
- [Dana 1993] S. S. Dana, M. Anderle, G. W. Rubiloff, and A. Acovic, "Chemical vapor deposition of rough-morphology silicon films over a broad temperature range," *Applied Physics Letters*, vol. 63, no. 10, pp. 1387-9, 1993.
- [Den Hartog 1949] J. P. Den Hartog, *Strength of Materials*. New York: Dover Publications, 1949.
- [Flinn 1987] P. A. Flinn, D. S. Gardner, and W. Nix, "Measurement and Interpretation of Stress in Aluminum-Based Metallizaion as a Function of Thermal History," *IEEE Transactions on Electron Devices*, vol. ED-34, no. 3, pp. 689-699, 1987.
- [Gaither 1988] S. A. Gaither, "Two-Dimensional Diffraction from a Surface-Relief Grating," Computer Program, Vers. 26 May 1988, courtesy of W. VeldKamp, MIT Lincoln Laboratory .
- [Gaylord 1982] T. K. Gaylord and M. G. Moharam, "Planar Dielectric Grating Diffraction Theories," *Applied Physics B*, vol. 28, no. pp. 1-14, 1982.
- [Gerhard-Multhaupt 1991] R. Gerhard-Multhaupt, "Light-valve technologies for high-definition television projection systems," *Displays*, vol. 12, no. 3/4, pp. 116-129, 1991.
- [Gerhard-Multhaupt 1990] R. Gerhard-Multhaupt, W. Brinker, H.-J. Ehrke, W.-D. Molzow, H. Roeder, T. Rosin, and R. Tepe, "Viscoelastic Spatial Light Modulators and Schlieren-Optical Systems for HDTV Projection Displays," *SPIE Large-Screen Projection Displays II*, vol. 1255, no. pp. 69-78, 1990.

- [Guckel 1989] H. Guckel, J. J. Sniegowski, and T. R. Christenson, "Fabrication of Micromechanical Devices from Polysilicon Films with Smooth Surfaces," *Sensors and Actuators*, vol. 20, no. 1989, pp. 117-122, 1989.
- [Guckel 1990] H. Guckel, J. J. Sniegowski, T. R. Christenson, and F. Raissi, "The Application of Fine-grained, Tensile Polysilicon to Mechanically Resonant Transducers," *Sensors and Actuators*, vol. A21-A23, no. 1990, pp. 346-351, 1990.
- [Hartog 1961] J. P. D. Hartog, *Strength of Materials*. New York: Dover, 1961.
- [Heath 1978] J. W. Heath and E. V. Jull, "Perfectly Blazed Reflection Gratings with Rectangular Grooves," *Journal of the Optical Society of America*, vol. 68, no. 9, pp. 1211-1217, 1978.
- [Hermansson 1991] K. Hermansson, U. Lindberg, B. Hok, and G. Palmskog, "Wetting Properties of Silicon Surfaces," vol. no. pp. 193-196, 1991.
- [Hong 1990] S. Hong, T. P. Weihs, J. C. Bravman, and W. D. Nix, "Measuring Stiffnesses and Residual Stresses of Silicon Nitride Thin Films," *Journal of Electronic Materials*, vol. 19, no. 9, pp. 903-909, 1990.
- [Hopkins 1992] G. W. Hopkins, "Light Valve Viewer," George W. Hopkins, Consultant, Nov. 1, 1992.
- [Hornbeck 1987] L. J. Hornbeck, "Spatial Light Modulator and Method," *United States Patent*, Number 4,710,732. Issued: Dec. 1, 1987.
- [Hornbeck 1989] L. J. Hornbeck, "Deformable-Mirror Spatial Light Modulators." In *Spatial Light Modulators and Applications III*, San Diego, California, Proceedings of the SPIE, vol. 1150, 1989.

- [Hornbeck 1990] L. J. Hornbeck, "Spatial Light Modulator," *United States Patent*, Number 4,956,619. Issued: Sep. 11, 1990.
- [Hornbeck 1991a] L. J. Hornbeck, "Spatial Light Modulator and Method," *United States Patent*, Number 5,061,049. Issued: Oct. 29, 1991.
- [Hornbeck 1991b] L. J. Hornbeck and W. E. Nelson, "Spatial Light Modulator System," *United States Patent*, Number 5,028,939. Issued: Jul. 2, 1991.
- [Hunt 1991] R. W. G. Hunt, *Measuring Colour*. 2nd ed., New York: E. Horwood, 1991.
- [Ibok 1993] E. Ibok and S. Garg, "A Characterization of the Effect of Deposition Temperature on Polysilicon Properties," *Journal of the Electrochemical Society*, vol. 140, no. 10, pp. 2927-37, 1993.
- [Kiesewetter 1992] L. Kiesewetter, J.-M. Zhang, D. Houdeau, and A. Steckenborn, "Determination of Young's Moduli of Micromechanical Thin Films Using the Resonance Method," *Sensors and Actuators A*, vol. 35, no. 1992, pp. 153-159, 1992.
- [Mastrangelo 1992] C. H. Mastrangelo and C. H. Hsu, "A Simple Experimental Technique for the Measurement of the Work of Adhesion of Microstructures." In *IEEE Solid-State Sensor and Actuator Workshop*, Hilton Head Island, SC, pp. 208-212, 1992.
- [Mastrangelo 1993a] C. H. Mastrangelo and C. H. Hsu, "Mechanical Stability and Adhesion of Microstructures under Capillary Forces—Part I: Basic Theory," *Journal of Microelectromechanical Systems*, vol. 2, no. 1, pp. 33-43, 1993a.
- [Mastrangelo 1993b] C. H. Mastrangelo and C. H. Hsu, "Mechanical Stability and Adhesion of Microstructures Under Capillary Forces—Part II: Experiments," *Journal of Microelectromechanical Systems*, vol. 2, no. 1, pp. 44-62, 1993b.

- [Matson 1989] D. W. Matson and R. D. Smith, "Supercritical Fluid Technologies for Ceramic-Processing Applications," *Journal of the American Ceramic Society*, vol. 72, no. 6, 871-81, 1989.
- [Murarka 1993] S. P. Murarka, *Metallization: Theory and Practice for VLSI and ULSI*. Boston: Butterworth-Heinemann, 1993.
- [Osram 1988] Osram Corporation, "HTI Metal Halide Short Arc Lamps," Sep. 1988. OCN-1007.
- [Osterberg 1994] P. M. Osterberg, R. K. Gupta, and S. D. Senturia, "A Quantitative Model for the Measurement of Residual Stress Using Electrostatic Pull-in of Beams." In *IEEE Solid-State Sensor and Actuator Workshop*, Hilton Head, SC, submitted for presentation, 1994.
- [Palik 1985] E. D. Palik, ed. *Handbook of Optical Constants of Solids*. Academic Press, 1985.
- [Petersen 1982] K. E. Petersen, "Silicon as a Mechanical Material," *Proceedings of the IEEE*, vol. 70, no. 5, pp. 420-457, 1982.
- [Photo Research 1992] Photo Research, "PR-650 SpectraColorimeter," vol. no. 1992.
- [Pryputniewicz 1994] R. J. Pryputniewicz, "Accelerated lifetime testing," Personal Communication, March, 1994 .
- [Ramo 1984] S. Ramo, J. Whinnery, and T. V. Duzer, *Fields and Waves in Communication Electronics, Second Edition*. John Wiley and Sons, 1984.
- [Sampsell 1990] J. B. Sampsell, "Spatial Light Modulator," *United States Patent*, Number 4,954,789. Issued: Sep. 4, 1990.

- [Sampsell 1992] J. B. Sampsell, "An Overview of the Digital Micromirror Device (DMD) and Its Application to Projection Displays." In *Society for Information Display Symposium*, Seattle, WA, vol. XXIV, pp. 1012-1015, 1992.
- [Sandejas 1993] F. S. A. Sandejas, R. B. Apte, W. C. Banyai, and D. M. Bloom, "Surface Microfabrication of Deformable Grating Light Valves for High Resolution Displays." In *Solid-State Sensors and Actuators: TRANSDUCERS '93*, Yokohama, Late News Digest, 1993.
- [Scheeper 1992] P. R. Scheeper, J. A. Voorthuyzen, W. Othuis, and P. Bergveld, "Investigation of Attractive Forces Between PECVD Silicon Nitride Microstructures and an Oxidized Silicon Substrate," *Sensors and Actuators A*, vol. 30, no. 1992, pp. 231-239, 1992.
- [Shimbo 1986] M. Shimbo, K. Furukawa, K. Fukuda, and K. Tanzawa, "Silicon-to-Silicon Direct Bonding Method," *Journal of Applied Physics*, vol. 60, no. 8, pp. 2987-2989, 1986.
- [Solgaard 1992a] O. Solgaard, "Integrated Semiconductor Light Modulators for Fiber-Optic and Display Applications", Ph.D. Dissertation, Stanford University, 1992a.
- [Solgaard 1992b] O. Solgaard, F. S. A. Sandejas, and D. M. Bloom, "A Deformable Grating Optical Modulator," *Optics Letters*, vol. 17, no. 9, p. 688, 1992b.
- [Stengl 1989] R. Stengl, T. Tan, and U. Gosele, "A Model for the Silicon Wafer Bonding Process," *Japanese Journal of Applied Physics*, vol. 28, no. 10, 1735-1741, 1989.
- [Veldkamp 1989] W. B. Veldkamp, G. J. Swanson, S. A. Gaither, C.-L. Chen, and T. R. Osborne, "Binary Optics: A Diffraction Analysis," MIT Lincoln Laboratory, Aug. 23, 1989. ODT-20.

- [Voutsas 1993] A. T. Voutsas and M. K. Hatalis, "Surface treatment effect on the grain size and surface roughness of as-deposited LPCVD polysilicon films," *Journal of the Electrochemical Society*, vol. 140, no. 1, pp. 282-288, 1993.
- [Wiszniewski 1993] W. R. Wiszniewski, R. E. Collins, and B. E. Pailthorpe, "Mechanical Light Modulator Fabricated on a Silicon Chip Using SIMOX Technology." In *Solid-State Sensors and Actuators: TRANSDUCERS '93*, Yokohama, pp. 1027, 1993.
- [Wolfram 1991] S. Wolfram, "Mathematica 2.0," Computer Program, Wolfram Research, Inc. .
- [Yoshida 1993] M. Yoshida, "Visit to Ultrafast Electronics Laboratory by Representatives of Sharp Electronics Corporation," Personal Communication, 1993 .

Appendix 1

Process Recipe

The recipe for two-dimensional arrays of GLVs is given in this appendix. The recipe is specific to the processes and equipment of the Center for Integrated Systems (CIS), Stanford University, during the latter part of 1993.

A1.1 Standard Process Steps

There are two standard cleaning steps that are part of any CIS process.

Organic Clean.

- a. $\text{H}_2\text{SO}_4:\text{H}_2\text{O}_2$, 9:1, 120C, for 00:20:00.
- b. Dump rinse and spin dry (hereafter, DRSD).

Diffusion Clean

- a. Organic Clean.
- b. $\text{H}_2\text{SO}_4:\text{H}_2\text{O}_2$, 3:1, 90C, for 00:10:00.
- c. DR.
- d. $\text{HF}:\text{H}_2\text{O}$, 1:50, for 00:00:15.
- e. DR.
- f. $\text{H}_2\text{O}_2:\text{H}_2\text{O}:\text{HCl}$, 1:5:1, 70C for 00:10:00.
- g. DRSD.

The standard lithography process includes:

- a. Singe, 150C, 00:30:00.

- b. SVGCoat recipe 1 (includes adhesion promoter and pre-bake).
- c. Expose 110mJ/cm², Ultratech stepper.
- d. SVGDev recipe 1 (includes development and post-bake).

A1.2 Current GLV process

1. SCRIBE

Buy L-Prime wafers.
Scribe.
DRSD.

2. WET THERMAL OXIDATION

Diffusion Clean.
Furnace Tylan 1,3, or 4. Program WET1000, process time 02:15:00.

3a. POLYSILICON DEPOSITION (option 1)

Furnace Tylanpoly. Program AMOR4006, process time 01:41:00.
target 0.32 μm .
T=560°C. SiH₄=136 sccm. H₂=110 sccm.

3b. POLYSILICON DEPOSITION (option 2)

Furnace Tylanpoly. Program AMOR550, process time 01:41:00.
target 0.26 μm .
T=550°C. SiH₄=136 sccm. H₂=110 sccm.

4. POLYSILICON DOPING

Furnace Tylan 6. Program POCL3900, process time 00:40:00.
Predep diffusion in POCl₃ ambient. T=900°C.
HF:H₂O, 1:50, for 00:00:30.
DRSD.

5. POLYSILICON LITHOGRAPHY

Standard lithography, field "POLY," reticle TWOLEVELS—clearfield.
Etcher Drytek2, Standard Poly Etch (SF₆:C₂ClF₅), 00:01:15 per wafer.

6. LOW TEMPERATURE OXIDE DEPOSITION

Diffusion Clean.

Furnace Tylanbpg. Program PSG400, T = 400°C, SiH₄=14 sccm, PH₃=86 sccm, process time 00:05:10. target 1225 Å—oxide will densify AND thicken during the reflow step by 100 Å.

7. OXIDE REFLOW

Furnace Tylan 1,3, or 4. Program REFLOW.

T = 950°C. Steam ambient. 00:10:00.

8a. NITRIDE DEPOSITION (option 1)

Furnace Tylannitride. Program SIN5.2, process time 00:37:45.

target 1325 Å.

T = 785°C. NH₃=32 sccm. DCS=165 sccm.

8b. NITRIDE DEPOSITION (option 2)

Furnace Tylannitride. Program SIN3.0, process time 00:33:45.

target 1325 Å.

T = 785°C. NH₃=50 sccm. DCS=150 sccm.

8c. NITRIDE DEPOSITION (option 3)

Furnace Tylannitride. Program SIN1.0, process time 00:28:00.

target 1325 Å.

T = 785°C. NH₃=100 sccm. DCS=100 sccm.

9. NITRIDE LITHOGRAPHY

Standard lithography, field "NITRIDE," reticle TWOLEVELS—clearfield.

Etcher Drytek2, Standard Nitride Etch (SF₆:CF₃Br), 00:04:30 per wafer.

NB: this is too short to clear up stringers; should be 00:08:00.

10. RELEASE ETCH

Organic clean.

Etch BOE 6:1, 00:02:50.

DRDRSD.

Appendix 2

Beam Model

The following Mathematica script was typical of those used in modelling the GLV mechanics. The first step is to assume Green's function for the beam equation is of a particular form. Then this solution with undetermined constants is constrained by the homogeneous beam equation, the boundary conditions for rigid supports, and the integral of the beam equation across an arbitrary impulse forcing function. Numerical values are substituted and Green's function $g[p, q]$ is evaluated as a 50×50 matrix. The function $\text{deform}[p, v, z]$ returns the convolution of Green's function and the nonlinear capacitor forcing function as evaluated for deflections p , with voltage v . z is a viscosity or step-size parameter to damp oscillations of the solution. $\text{iter}[v, k]$ is a routine that calculates the self consistent beam deflection for voltage v , with k as a limit on the number of iterations. The remainder of the appendix shows the details of a calculation of a hysteresis loop.

```

y1= a1 + b1 x + c1 E^(T x) + d1 E^(- T x);
y2= a2 + b2 x + c2 E^(T x) + d2 E^(- T x);

boundaryValues = Solve[ {
  y1==0 /. x->0,
  y2==0 /. x->1,
  D[y1,{x,1}]==0 /. x->0,
  D[y2,{x,1}]==0 /. x->1,
  y1==y2 /. x -> a,
  D[y1,{x,1}]==D[y2,{x,1}] /. x -> a,
  D[y1,{x,2}]==D[y2,{x,2}] /. x -> a,
  D[y1,{x,3}] - D[y2,{x,3}] + W ==0 /. x -> a},
  {a1,b1,c1,d1,a2,b2,c2,d2}];

s1= y1 /. boundaryValues;
s2= y2 /. boundaryValues;

ee = 1.2 10^11;           Young's Modulus [Pa]
ep0 = 8.85 10^-12;        Permittivity of Free Space [F/m]
tt = .13 10^-6;           Beam Thickness [m]
dd = 1 10^-6;             Beam Width [m]
ll = 25 10^-6;            Beam Length [m]
ii = dd tt^3 / 12;        Beam Moment of Inertia
t0 = .13 10^-6;           Spacer Thickness [m]
ten = 400 10^6;           Residual Beam Stress [Pa]
ww = 10^-12 ep0 ll dd / (2 t0^2 ee ii)
      Normalized electrostatic attraction (equal to W)
tt = 10^-6 (ten tt dd/ (ee ii))^5
      Normalized restoring force (equal to T)

p1 = First[Simplify[ s1 /.
  {T -> .070 1.414, W -> 8.2 10^(-6), l -> 50}]];
p2 = First[Simplify[ s2 /.
  {T -> .070 1.414, W -> 8.2 10^(-6), l -> 50}]];
g[p_,q_] := If[p>q, p2 /. {x -> p, a ->q}, p1/.
  {x -> p, a ->q}]           Green's Function at q

bounds[i_] := {i,1,49,1}

deflectionTable = Table[g[x,a],Evaluate
  [bounds[a]], Evaluate[bounds[x]]];
      Numerical evaluation of g

forcingFunction[d_] := If[d<.10,((1 - d/.13)^(-2)),
  58 - 6 10^3 (d-.2)] +
  If[d>.135,5 10^3 (d - .135),0]

limitFunction[c_] := Max[Min[.135,c],0]

```


-Graphics-

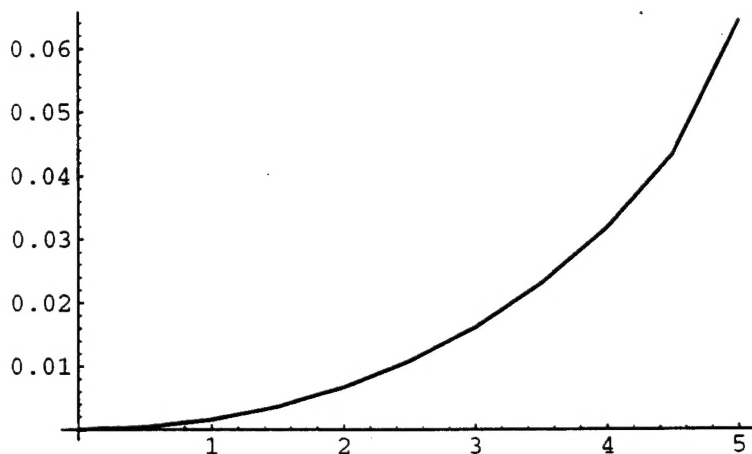
```
deform[p_,v_,z_] := Module [{i},
  forceVector = Map[forcingFunction,p];
  qC = (v^2)/49 deflectionTable . forceVector;
  qC = Map[limitFunction,qC];
  p + z (qC-p)
] This module performs one iteration of the self-
  consistent algorithm
```

```
iter[v_,k_] := Module [{i},
  For[m={},error={};
  oldY=y;e1=1;e2=errorFunc[yFull,y];step=
  Min[10 e2,.9];i=1,
  ((i<=k) && (e1 > 10^-5) && (e2 > 10^-4)), i++,
  newY = deform [y,v,step];
  m = Append[m,newY];
  e1 = errorFunc[y,newY];
  e2 = errorFunc[yFull,newY];
  error = Append[error,{e1,e2,step}];
  step = If[ 200 e1 < step,step/2,step];
  step = If[ 10^2 e2 < step,step/3,step];
  oldY = y;
  y = newY;
];
showY
] This module calculates the deformation at voltage v_
```

y = yZero

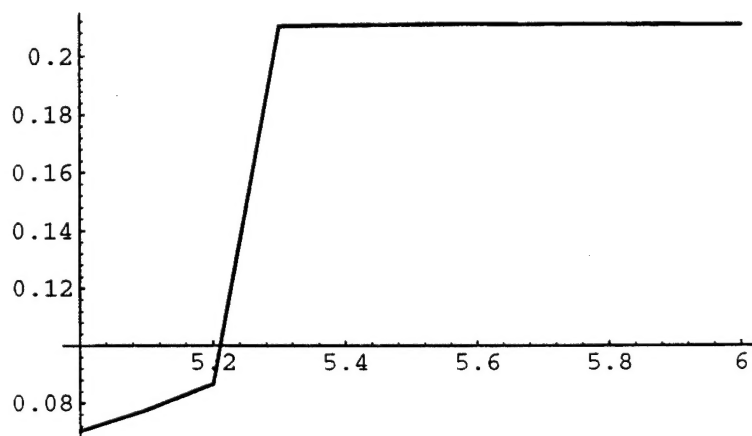
```
{0, 0, 0, 0, 0, 0, 0, 0, 0, 0, 0, 0, 0, 0, 0, 0, 0, 0, 0, 0
  0, 0, 0, 0, 0, 0, 0, 0, 0, 0, 0, 0, 0, 0, 0, 0, 0, 0, 0,
```

viter[0,5,.5,50]



```
{{0, 0}, {0.5, 0.000377021}, {1., 0.00157196}, {1.5, 0.0036
  {2.5, 0.0107871}, {3., 0.0161082}, {3.5, 0.0229396}, {4.,
    {4.5, 0.0431862}, {5., 0.0641659}}}
```

viter[5,6,.1,100]

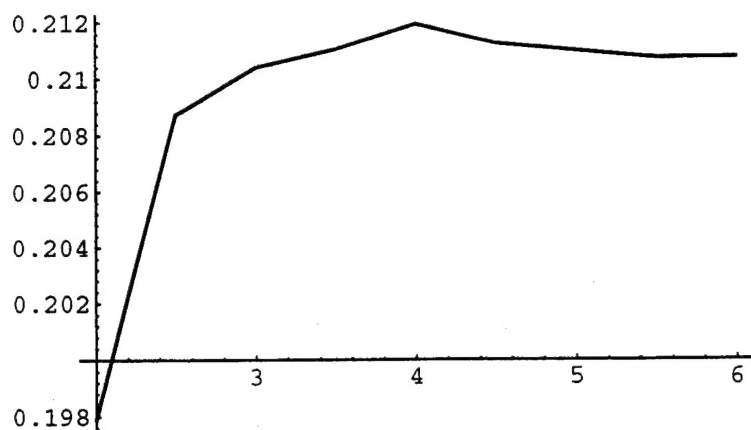


```
{{5, 0.0703352}, {5.1, 0.0775739}, {5.2, 0.0866328}, {5.3,
  {5.5, 0.211044}, {5.6, 0.211131}, {5.7, 0.210948}, {5.8,
    {6., 0.210744}}}
```

Join[%75,%76]

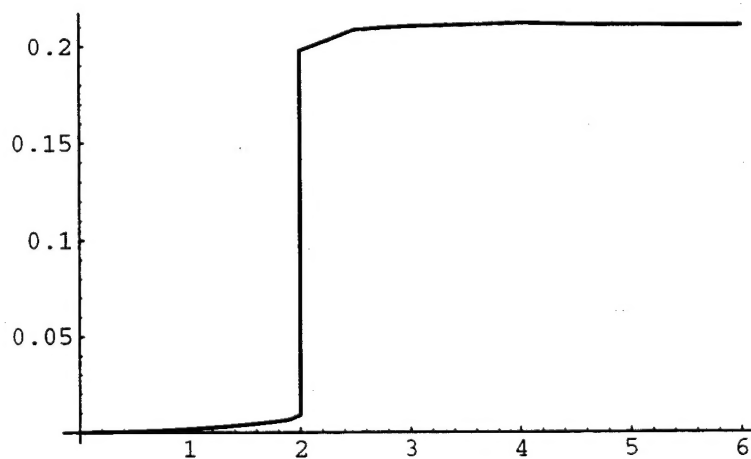
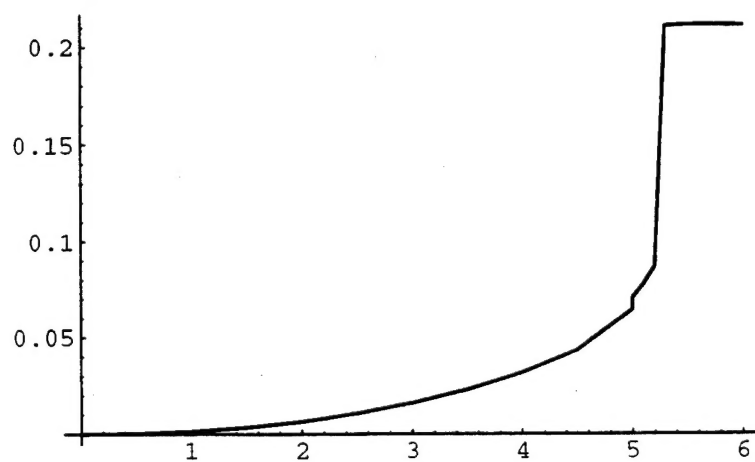
```
{{0, 0}, {0.5, 0.000377021}, {1., 0.00157196}, {1.5, 0.0036
  {2.5, 0.0107871}, {3., 0.0161082}, {3.5, 0.0229396}, {4.,
    {4.5, 0.0431862}, {5., 0.0641659}, {5, 0.0703352}, {5.1,
      {5.3, 0.210394}, {5.4, 0.210773}, {5.5, 0.211044}, {5.6,
        {5.8, 0.210906}, {5.9, 0.210802}, {6., 0.210744}}}
```

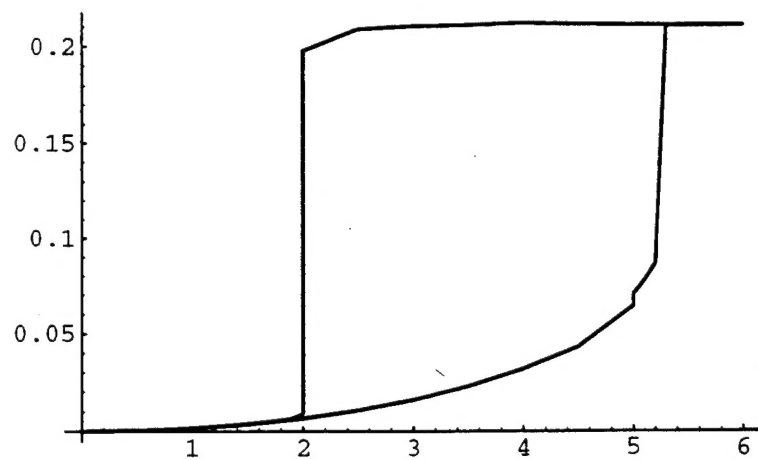
viter[6,2,-.5,30]



```
{ {6, 0.210758}, {5.5, 0.210734}, {5., 0.210985}, {4.5, 0.210734},
  {3.5, 0.211063}, {3., 0.210419}, {2.5, 0.208765}, {2., 0.198}
```

```
Show[ ListPlot[%79,PlotJoined -> True],
ListPlot[%83,PlotJoined -> True]]
```





-Graphics-

t=2000 A, T = 400 MPa, v = voltage * 2, L = 50 μ m